UNIVERSITÀ DEGLI STUDI DI TRIESTE

XX ciclo del Dottorato di Ricerca in Nanotecnologie

A.A. 2005-2007

Design of Nanostructured Catalysts for H_2 Production and CO_2 Hydrogenation

Dottoranda
Loredana De Rogatis

Coordinatore del collegio dei docenti
Chiar.mo prof. Maurizio Fermeglia
Università degli Studi di Trieste

Supervisore/Relatore
Chiar.mo prof. Paolo Fornasiero
Università degli Studi di Trieste

Correlatore
Dr. Erik Vesselli
Università degli Studi di Trieste

Following roads made by others may be easy, but not free.
Making one's own roads, in turn, may be free, but never easy.
Aaro Hellaakoski

to my little brother

CONTENTS

Chapter 3
Rh embedded into Al_2O_3

Chapter 4
Ni_xCu_y/Al_2O_3

Chapter 5
Embedding strategy extension: non precious metals

ABBREVIATIONS

CRR = Combustion and Reforming Reaction

DFT = Density Functional Theory

DMEA = N,N-dimethylethanolamine

DPO = Direct Partial Oxidation

EtOH-SR = Ethanol Steam Reforming

HDA = Hexadecylamine

HEAC16Br = N-hexadecyl-N-(2-hydroxyethyl)-N,N-dimethyl ammonium bromide

EXAFS = Extended X-ray Absorption Fine Structure

HREELS = High Resolution Electron Energy Loss

LEED = Low Electron Energy Diffraction

MCC = Methane Complete Combustion

MDR = Methane Dry Reforming

MeOH-SR = Methanol Steam Reforming

MPO = Methane Partial Oxidation

MSR = Methane Steam Reforming

PVP = Polyvinilpirrolidone

SPC = Solid Phase Crystallization

TEM = Transmission Electron Microscopy

THF = Tetrahydrofuran

TPD = Temperature Programmed Desorption

TPO = Temperature Programmed Oxidation

TPR = Temperature Programmed Reduction

UHV = Ultra High Vacuum

WGS(R) = Water Gas Shift (Reaction)

XAFS = X-ray Absorption Fine Structure

XANES = X-Ray Absorption Near Edge Spectroscopy

XPS = X-ray Photoelectron Spectroscopy

Chapter 1

Introduction

1.1 Energetic and environmental issues

The world's current energy system has been built around the many advantages of fossil fuels. Every aspect of modern life is made from, powered with, or affected by them. Fossil fuels like oil, coal and natural gas are extremely attractive as energy sources because they are highly concentrated, enabling large amounts of energy to be stored in relatively small volumes and they are relatively easy to distribute. However, fossil energy sources are non-renewable being an irreplaceable endowment produced from millennia of biological and geological processes. This means that on the human time-scale they cannot be naturally regenerated and are only available in a finite amount on earth.

The expanding world population and the increasing standards of living and demands for energy in developing countries is putting increasing pressure on diminishing fossil fuel resources and making them even more costly. Predictions based on extrapolation of the energy consumption show that the demand will soon exceed the supply. No matter how long the fossil fuels will last their amount is finite. New oil and gas fields are being still discovered and the methods for retrieving oil from known fields are continuously improving although extraction energy costs would become higher than the actual energy yield due to increased energy costs for research, deep drilling, as well as to lower quality and accessibility of the still available oil storages. Vast reserves, like tar and gas hydrates, await technology to enable their economically and environmentally sound exploitation. Large coal reserves can also be exploited, for example through gasification and Fischer-Tropsch synthesis.

In addition to these aspects, there is clearly a problem of worldwide energy dependence. Since the fossil fuels were created in specific circumstances where the geological conditions were favorable, the largest deposits of oil, gas and coal tend to be concentrated in particular regions of the globe (e.g. two-third of the world's proven oil reserves are located in the Middle East and North Africa) often characterized by political instability in their international relationships [1].

The potentially damaging environmental effect of continuous fossil fuel usage is another factor which has to be considered. Although there is a considerable disagreement as to whether increased fossil fuel consumption is the primary cause of global climate change (e.g. earth's temperature increase and sea level rises), there is a general agreement that a strong correlation exists between localized and regional air pollution and fossil fuel consumption. The exploitation of fossil fuel resources entails significant health hazards in the course of their extraction, for example in coal mining accidents or fires on oil or gas drilling rigs. They can also occur during distribution, for example in oil spillages from tankers that pollute beaches and kill wildlife; or on evaporation process or on combustion, which generate atmospheric pollutants such as sulphur dioxide, carbon monoxide, fine particulate matter, nitrogen oxides, hydrocarbons and very large quantities of carbon dioxide (CO_2) which contributes to the well known greenhouse effect. Concerning the CO_2 emission, several schemes have

been proposed to continue the use of fossil fuels by separating the CO_2 from exhaust gases and sequestrating it into permanent deposits such as depleted gas wells or other stable geological formations [2]. Another promising approach is based on the conversion of CO_2 into more valuable chemical products. Up to now, few industrial processes utilize it as a raw material (see § 1.3). It is worthy of note that an increasing use of CO_2 as feedstock for producing chemicals does not have only an important impact on the mitigation of greenhouse gas emissions, but it can also provide a strategic path for its recycle and reuse opening, at the same time, new opportunities for catalysis and industrial chemistry [3].

The development of new energy strategy that could be economical and environmentally sustainable and be able to meet the demands for a broad range of services (household, commerce, industry and transportation needs) is an imperative challenge. There is not a unique solution which is able to sort out all energy-related problems. Indeed, there must be a global strategy which is based on local solutions: each option shows its own advantages, handicaps and social-economic impact. Nowadays, it is generally accepted that diversification of energy sources is essential [4,5].

One approach that has been proposed and widely discussed recently is the use of hydrogen. It can be considered one of the key energy carriers in terms of energy source, as fuel for transportation and intermediate in the conversion of renewable energy sources. In addition, hydrogen is also of relevance as a clean fuel for fuel cells. However, before a hydrogen-fuelled future can become a reality many complex challenges must be overcome. Before it can be used for instance in fuel cell systems, hydrogen needs to be extracted in a clean and efficient way from the other compounds within which it is normally bonded in nature and this separation requires energy [6-8]. Moreover, there are problems related to the storage technology [9,10] and to the creation of a safe distribution and transport network for this new energy carrier. Furthermore, the potentially harmful effects on environment is recently the object of extensive discussions. The widespread use of hydrogen fuel cells could have hitherto unknown environmental impacts due to unintended emissions of molecular hydrogen, including an increase in the abundance of water vapor in the stratosphere [11].

Although all these aspects make hydrogen far from the application in fuel cells on large scale, there is, however, great interest in increasing hydrogen production for the current and well-established operative processes which consume most of hydrogen to produce fertilizers and to purify oil, more and more dirty, from sulfur (HDS = Hydrogen De-Sulfurization) and nitrogen (HDN = Hydrogen De-Nitrogenization) satisfying the stringent regulations on gasoline.

1.2 Heterogeneous catalysis and nanotechnology

Heterogeneous catalysis is an important part of the technology that supports industrially developed societies. Production of transportation fuels, pollution control, production of low-cost and high-quality raw materials are just some of the areas in which heterogeneous catalysis shows a remarkable impact.

The importance of catalyst's size in catalytic processes does not represent a novelty. Nano-size metal particles have occupied a central place in heterogeneous catalysis for many years, long before recognition of nanotechnology.

It is well known that the efficiency of a catalyst is directly proportional to its surface area. For this reason, many of the heterogeneous catalysts, used in industry today, consist of one or several catalytically active component(s) in the form of very small particles (typically in the size range of 1-100 nm) deposited on the surface of a support (e.g. oxide), a highly porous and thermostable material with a high surface area and suitable mechanical strength. The use of nanoparticles results in a large contact area between the active material of the catalyst and surrounding gas or liquid phase. This ensures that the catalytic material is used efficiently. The extremely small size of the particles maximizes surface area exposed to the reactant, allowing more reactions to occur. Maximizing the surface area is not the only reason for using nanoparticles as heterogeneous catalysts. Indeed, the size of the metal crystallites in the supported metal catalysts has a profound effect on the catalytic activity. A heterogeneous catalytic reaction begins with the adsorption of the reacting gases or liquids on the surface of the catalyst, where intramolecular bonds are broken or weakened. Next, the adsorbed species react on the surface, often in several consecutive steps. finally, the products desorb from the surface into the gas phase, thereby regenerating the active sites on the surface, ready for the next catalytic cycle. With a reduction of particle size the relative proportion of active sites per unit area of the metal particles increases, so that much higher catalytic activity or a highly selective reactions may be expected.

It has to be strongly emphasized the fact that the effect of size reduction is not without consequences also for the physical-chemical properties of the particles. Indeed, if a metal particle, initially having bulk properties, is reduced in size down to a few hundreds or dozens of atoms, the density of states in the valence and conduction bands decreases and the electronic properties change dramatically. The quasi-continuous density of states is replaced by quantized levels with a size-dependent spacing (quantum size effect). In this situation, new properties can be achieved. Therefore, tuning particle sizes provides the possibility to modulate the catalytic activity. This is a great opportunity for heterogeneous catalysis.

In this respect, a typical example is represented by gold. Au was historically considered catalytically inert, but in 1987 Haruta *et al.* [12] showed that nanosized (< 5 nm) Au particles can be very effective catalysts. The fact that Au particles with diameters of about 5 nm or less have unique catalytic properties has opened a new

research area for an explanation of this unexpected effect and for chemical reactions that are catalyzed by Au [13-16]. In some cases, catalysts based on nanosized Au particles allow a significantly lower reaction temperature than those used in existing processes, which is promising for the development of novel energy efficient processes [17-20]. The origin of the high catalytic activity of gold catalysts has been strongly debated and various models were presented. Quantum size effects, charge transfer to and from the support or support-induced strain, oxygen spillover to and from the support, the Au oxidation state, and the role of very low-coordinated Au atoms in nanoparticles were proposed. It is likely that several of the aforementioned effects occur simultaneously.

However, thermal stability of these nanomaterials is limited by their critical sizes; the smaller the crystallite size, the lower thermal stability. The main purpose of using a support is to achieve an optimal dispersion of the catalytically active component(s) and to stabilize it (them) against sintering and hence to increase the catalyst life. Furthermore, in several reactions, the support is not inert and the overall process is actually a combination of two catalytic functions: that of active component(s) and that of the support. In addition, it has to be considered that heterogeneous catalysts often consist of expensive transition metals like Pt, Rh or Pd. In this case, it is evident that reducing the quantity of noble metal employed has then a large economical interest. Powders or finely dispersed particles are therefore preferred to bulk materials. However, this morphological change has deep implications also for the electronic structure of the metals and for their catalytic properties [21].

The need to formulate new catalysts, which exhibit enhanced performance with respect to those currently employed for specific applications represents a difficult undertaking due to the compositional and structural complexity of these systems.

Research in nanotechnology and nanoscience is expected to have a great impact on the development of new catalytic systems [22]. In particular, the innovative idea which is at the base of the nanocatalyst generation is the acquisition of the ability to design, synthesize and control the catalyst on nanometer scale. A major goal in nanocatalysis is to design catalysts that can achieve perfect selectivity and desirable activity controlling the formation of the active site, the environment around the active site, the binding sites and their locations relative to the active site and the path to access these functionalities [23]. To possess this capacity means consequently to have the control of the activity and selectivity of catalyst action.

Designing catalysts that are more efficient, more selective, and more specific to a certain type of reaction can lead to significant savings in manufacturing expenses. A higher activity will be reflected either in high productivity from relatively small reactors and catalyst volumes or in mild operating conditions, particularly temperature. Higher selectivity produces high yields of a desired product while suppressing undesirable

reactions. A reaction of perfect selectivity not only can generate no waste products, thereby reduce energy and process requirements for separation and purification.

For many years, the only way to develop new or improved catalysts was by empirical testing in so-called trial-and-error experiments [24]. This time-consuming and costly procedure is now beginning to be replaced by more rational procedure based on the fundamental nanoscale knowledge of catalysis. This has been made possible due to the extensive developments of sophisticated theoretical and experimental methods which have increased the general understanding of catalysis. In fact nowadays, researchers start to ab-initio simulate nanoscale materials to prediction the structural, morphological, compositional, electronic, and chemical aspects of a catalyst, with the final goal to identifying specific guidelines for improved reactivity, selectivity and stability. In this field, the surface science techniques play also a key role [25]. Indeed, they provide experimental powerful means to explore the very basic properties of catalysts at molecular or atomic level. Furthermore, they drive, in some cases, heterogeneous catalysis research in the establishment of useful relationships between the atomic level physical and chemical properties of the catalyst with the observed catalytic behavior.

1.3 Catalytic reactions for H_2 production

1.3.1 H_2 from fossil fuels and renewable resources

Hydrogen production is the first step towards the transition to the Hydrogen Economy. It can be produced catalytically using any hydrogen-containing compound as a fuel. The sustainable production of growing amounts of hydrogen must be based on clean process.

Today enormous amounts of hydrogen are generated, handled, transported and used as a feedstock in the chemical industry, for instance, in the manufacture of ammonia, methanol, hydrogen peroxide, polymers and solvents. In refineries, it is used in large quantities to purify oil from sulfur, to convert heavy and unsaturated compounds to lighter and more stable compounds. The pharmaceutical industry uses hydrogen to manufacture vitamins and other pharmaceutical products. Furthermore, significant quantities of hydrogen are used to purify gases that contain traces of oxygen, in glass and ceramics manufacture, to hydrogenate unsaturated fatty acids in animal and vegetable oils, producing solid fats for margarine and other food products. Finally, there is a growing demand of hydrogen in the manufacture of semi-conducting layers in integrated circuits and in other miscellaneous applications. All this hydrogen is a chemical substance, not an energy commodity. Currently, almost 96% of the world's hydrogen needs are produced form fossil fuels, with almost half being generated by the steam reforming of natural gas, the most widely adopted and the cheapest process.

Hydrogen production and transportation costs are absorbed in the price of the synthesized chemicals. The cost of this hydrogen remains irrelevant as long as the final products find markets. At present, the use of hydrogen is governed by economic arguments and not by energetic considerations. But if hydrogen is used as an energy carrier, energetic arguments must also be considered. In this context, it is important to emphasize that not only the monetary cost of hydrogen is important and should be as low as possible, but also the energy cost of synthesizing it and bringing it to the end user. The Hydrogen Economy would be meaningful, only if the energy consumed to produce, pack, store and distribute hydrogen was as low as possible compared to the energy content of the delivered fuel gas. This aspect is not always recognized. The Hydrogen Economy differs significantly from the natural gas economy where the energy invested to extract and clean natural gas is small compared to its energy content. It is not so for hydrogen used as energy carrier.

In the next decade, the demand for hydrogen, both for traditional uses and for running fuel cells, is expected to grow [26,27]. Technical solutions, which have to be able to produce hydrogen in sufficient quantities to meet all kind of demand, are really necessary.

Hydrogen can be produced from a variety of feedstocks: from fossil resources such as natural gas and coal, from renewable resources such as biomass and from water. A variety of process technologies can be used, including chemical, biological, electrolytic, photolytic and thermo-chemical. Each technology is in a different stage of development, and offers unique opportunities, benefits and challenges. Local availability of feedstock, maturity of technology, market applications and demand, policy issues and costs will influence the choice and timing of the various options for hydrogen production.

In the near- and mid-term, hydrogen production from hydrocarbons, like methane which represents the main component of natural gas, seems to be the best choice to achieve a gradual transition, given that the present infrastructure can be used and a certain reduction degree of greenhouse gas emissions can be achieved.

In the long term, a hydrogen-based energy system should use renewable sources such as biomass for meeting sustainability goals [10,28]. Renewables are essentially inexhaustible and their employment usually entails much lower emissions of greenhouse gases or other pollutants, and fewer health hazards. In addition to their environmental benefits, renewable sources promise to enhance energy security by reducing the country's reliance on fossil fuels from other nations. Unfortunately, the current costs of renewable energy sources are in many cases higher than those of conventional sources, and this has until recently retarded their deployment.

1.3.2 Methane Partial Oxidation

Methane Partial Oxidation (MPO) has been addressed as a promising alternative route to the conventional Steam Reforming process (MSR) for the production of H_2 in small and medium energy related applications. In MPO (Eq. 1.1) the fuel reacts with a quantity of oxidizer (O_2) which is less than the stoichiometric amount required for the complete combustion.

$$CH_4 + \frac{1}{2}O_2 \rightarrow 2H_2 + CO \qquad (1.1).$$

This technology offers many advantages with respect to MSR. The reforming reaction is less exothermic than MSR and it avoids the need for large amounts of expensive super-heated steam, so it requires lower energy costs. All these aspects would allow to reduce the cost of the whole plant. The disadvantages lie with the fact that fuel and oxygen must be premixed. The proportions are such that the mixture may be flammable or even explosive, particularly if small variations (e.g. as a result of pumping and vaporizing liquid fuels) are possible. Moreover, the process requires oxygen, the separation of which from air at low cost is still technically difficult.

Concerning the reaction pathway, two mechanistic schemes have been proposed: (a) an indirect scheme, labeled as the Combustion and Reforming Reaction (CRR) mechanism and (b) a direct scheme, labeled as Direct Partial Oxidation (DPO) mechanism. According to the CRR scheme, initial combustion of the hydrocarbon (Eq. 1.2) is followed by the reforming reactions of the unconverted methane with H_2O (Eq. 1.3) and CO_2 (Eq. 1.4) produced in the first step. The water gas shift reaction is also involved.

Methane Complete Combustion (MCC):

$$CH_4 + 2O_2 \rightarrow CO_2 + 2H_2O \qquad (1.2).$$

Methane Steam Reforming (MSR):

$$CH_4 + H_2O \rightarrow CO + 3H_2 \qquad (1.3).$$

Methane Dry Reforming (MDR):

$$CH_4 + CO_2 \rightarrow 2CO + 2H_2 \qquad (1.4).$$

The CRR pathway is characterized by temperature gradients along the catalytic bed, since the highly exothermic combustion reaction takes place at its front, while the other reactions occur in the second part of the catalytic bed. This results in several

undesirable consequences such as catalyst deactivation due to sintering or danger of explosion.

On the other hand, in the DPO mechanism CH_4 and O_2 decompose on the surface of the catalyst and surface species recombine to produce CO and H_2 as primary products. CO_2 and H_2O are secondary products, obtained by successive reactions of the primary products with O species in the surface.

Supported noble metal catalysts, including Rh, Ru , Pd and Pt and supported Ni catalysts have been reported to be active. The type of catalyst employed (e.g. metal, support type, etc) and the operative conditions (e.g. gas hourly space velocity, reactant concentration, gas flow rate, etc) may strongly influence the reaction steps of the process.

Despite intensive research efforts, this technology has encountered significant problems in the industrial scaling – up.

1.3.3 Methanol Steam Reforming

Methanol is often considered as a unique and advantageous fuel in many ways, which explains the large amount of interest in it as a hydrogen carrier for fuel cell applications. Methanol can be converted to hydrogen at lower temperatures (150-350 °C) than most other fuels (>500 °C) because it contains no carbon-carbon bonds that must be broken, and unlike methane, it is easily activated at low temperatures. Low-temperature conversion leads to low levels of CO formation, a poison for fuel cell electrodes [29]. However, its main drawback is its high toxicity.

Methanol Steam Reforming (MeOH-SR, Eq. 1.5) is one of the most feasible process for on-board production of hydrogen for fuel cells applications and consequently it has been thoroughly studied.

$$CH_3OH + H_2O \rightarrow 3H_2 + CO_2 \qquad (1.5).$$

The reaction can yield a gas containing up to 75 % hydrogen while maintaining a high selectivity towards carbon dioxide. The main drawback of the steam reforming process is that it is slow and endothermic. The high-energy requirement for the reaction is a major obstacle for the implementation of a reformer based upon this process in an automotive application. There are however several commercial solutions available based upon steam reforming .

Large variety of catalysts has been reported to be active for MeOH-SR. The kinetics and reaction paths depend on the catalytic materials used. The majority of these systems has been Cu-based mainly as an outgrowth of their extensive use in methanol synthesis [30-34].

Concerning the reaction mechanism, two major pathways were suggested in the literature over copper-based catalysts: (i) a decomposition-water-gas shift (WGS) sequence and (ii) methanol dehydrogenation to methyl formate (Eq. 1.6).

In the decomposition-WGS pathway methanol decomposes initially to CO and H_2 and then the CO reacts further with water to form CO_2 and H_2. This reaction scheme was proposed by several authors and was deeply studied over both commercial and novel catalysts.

The methyl formate reaction route was shown to be dependent on the nature of the support. CO does not form and methyl formate and formic acid are the only intermediates . For instance, over γ-alumina the suggested path is as follows :

$$2CH_3OH \rightarrow CH_3OCHO + 2H_2 \qquad (1.6)$$

$$CH_3OCHO + H_2O \rightarrow HCOOH + CH_3OH \qquad (1.7)$$

$$HCOOH \rightarrow CO_2 + H_2 \qquad (1.8).$$

The formation of by-products during the process, such as CO, formic acid and methyl formate is a significant parameter as it poses a threat to the performance of the fuel cells. It is possible to minimize the formation of CO by operating the MeOH-SR in excess of steam and thereby integrating the WGSR into the reformer.

The catalytic properties of copper catalysts for MeOH-SR are significantly different from other transition metals. Several investigations were performed on the behavior of Group 9-10 transition metals [35-37]. The major difference is the CO_2 selectivity. The high CO concentrations obtained on these systems make them highly unsuitable for fuel cells applications.

1.3.4 Ethanol Steam Reforming

Unlike methanol, ethanol is completely renewable and has lower toxicity. It can also be more easily stored and safely handled. Most importantly, it can be produced in large amounts from biomass such as agricultural wastes and forestry residues. This could prove advantageous in tropical countries with a warm climate where there are large plantations of corn and sugarcane. The bioethanol-to-hydrogen system has the significant advantage of reduced CO_2 emissions, since a significant fraction of the produced carbon dioxide is consumed for biomass growth. Notably, the carbon cycle is not a perfectly closed loop, due to the energy requirements for biomass cultivation, transformation and residue treatments. However, there are also important limitations. In fact, cultivation devoted to ethanol production requires large space and consumes significant water resources as in the case of sugar cane. It has been indicated that the

overcropping of the soil can be a problem in some case. For other cultivation, such as maize, a possible competition between food and energy was indicated.

Extensive experimental and theoretical studies on hydrogen production from Ethanol Steam Reforming (EtOH-SR, Eq. 1.9) are reported in the literature.

$$C_2H_5OH + 3H_2O \rightarrow 6H_2 + 2CO_2 \qquad (1.9).$$

The reaction network involved in EtOH-SR is very complex. Many pathways are possible as shown in Figure 1.1.

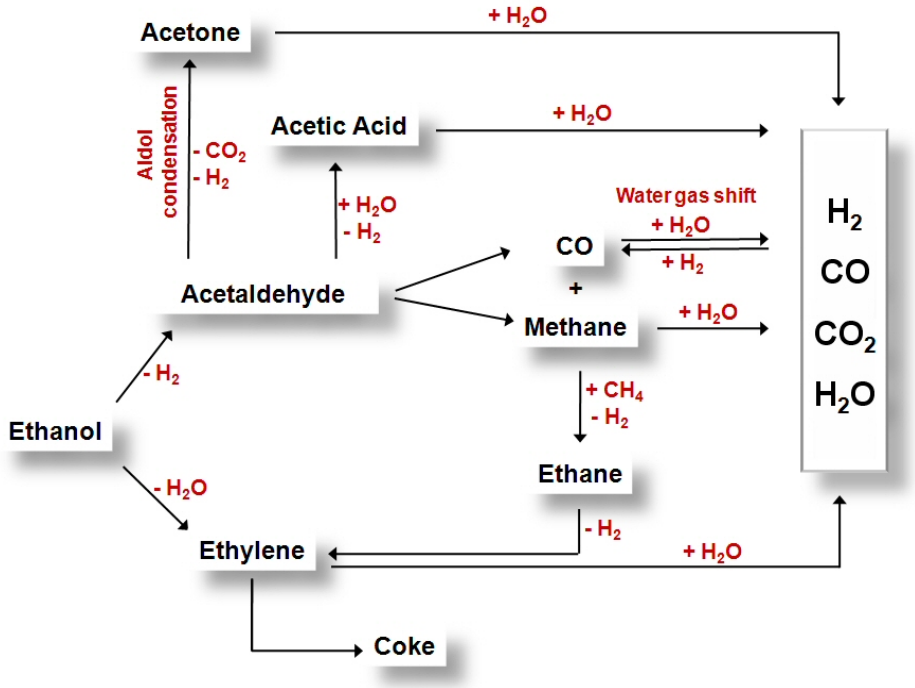

Figure 1.1: reaction pathways for steam reforming of ethanol.

The process includes several steps that require catalytic sites able to dehydrogenate ethanol, to break the C – C bonds of surface intermediates producing CO and CH_4 and to promote the steam reforming of CH_4. Moreover, the water gas shift reaction is also involved, contributing to reduce the CO concentration and increasing the H_2 production. Some of these steps can be favored depending on the catalyst used . However, other secondary reactions can be involved. Dehydration reaction leads to the formation of ethylene, especially when acid supports are used (such as Al_2O_3). Ethylene is easily transformed into carbon that is deposited on the active phase producing the deactivation of the catalyst. Also ethane, formed by methane coupling, acts as very strong promoter for carbon formation. Acetone could be produced from acetaldehyde through a series of reactions involving aldol condensation, oxidation and

decarboxylation. Significant formation of this product is observed when the support may provide structural oxygen for the oxidation step (such as CeO_2 or $Ce_xZr_{1-x}O_2$). The formation of byproducts like methane, ethane, acetaldehyde, acetic acid and acetone is undesirable because they decrease the hydrogen production efficiency and they can reduce the operational time of the catalyst.

It is clear that the catalyst choice plays a crucial role in the reactivity towards the complete conversion of ethanol. Most of the employed catalysts are Al_2O_3-supported metals, noble metals or alloys [38-46]. The catalytic activity and product distribution over these systems depend on the metal (e.g. noble metal or non precious metal), the type of metal precursor, the metal content, the presence of additives, the type of support the method of catalyst preparation and the reaction conditions.

1.4 CO_2 hydrogenation: a chemical route for CO_2 valorization

The utilization of CO_2 has become an important global issue and priority in view of the so-called sustainable society. In fact, it is impossible to decrease and control the CO_2 emissions only by efforts for energy saving and efficient use of energy [47]. As mentioned in § 1.1, the use of CO_2 as feedstock or co-reactant represents a challenging opportunity which can stimulate new approaches in industrial chemistry leading to new and valuable materials as well as to new routes in the synthesis of chemicals.

Up to day, CO_2 is rarely used to its fullest potential due to its high thermodynamic and kinetic stability. The use of a catalyst to promote reaction rates and/or selective pathway of reaction is typically required. Notably, the source and the amount of energy required for carbon dioxide conversion are matter of fundamental importance in order to define the exact potential of each technology and of its application [48].

Catalytic hydrogenation of carbon dioxide has been recognized as one of the promising approaches for its valorization not only because it can generate fuels, but also because some products (e.g. HCOOH, CH_3OH, H_2CO) would be useful hydrogen carriers and could find a large use also in a hydrogen based economy [49].

CO_2 hydrogenation shows advantageous features (e.g. high conversion rate, high selectivity) with respect to other chemical conversion methods. However, the main problem in this type of process is the large quantity of H_2 as the reducing reagent for CO_2.

Methanol synthesis from carbon dioxide and hydrogen has been widely investigated [50]. In addition to its use as a clean fuel in future-oriented energy systems, methanol is regarded as one of the carbon resources or, in other words, is considered one of the key substances in the C_1 chemical industry. It is a key material for producing various organic compounds such as acetic acid, methylamine and formaldehyde. The high value of this building block has a potential to compensate the cost of H_2 used as the reducing

agent. Therefore, many efforts have been recently done to develop catalysts for methanol synthesis from CO_2 and H_2.

1.5 Choice of materials and purpose of the work

To make the reactions described in the previous sections, economically viable and competitive in industrial market, it is necessary to design catalysts with high activity, selectivity and, more important, stability and long lifetime.

The work presented in this thesis concerns the design of noble metal- and non-precious metal-based catalysts. Among noble metals, Rh was chosen as the active phase, since it shows good yields, good selectivity and good resistance towards deactivation due to coke deposition. Furthermore, its high catalytic activity allows the use of low metal loadings, which is a significant economic advantage for the commercialization of such type of catalysts. We demonstrate that the controlled synthesis of Rh nanoparticles embedded in porous oxides results in catalysts which exhibit high hydrogen yield for partial oxidation of methane. Moreover, we show that the process of encapsulation of the Rh nanoparticles during the synthesis, largely prevents metal sintering. A simple and low cost synthetic route to realize this innovative approach is proposed. In order to investigate the possible influence of the thickness of the protective layer on the metal-support interaction, as well as the nature of the Rh species, an XPS study on model embedded Rh systems was also performed. The effects of the thermal/chemical treatments were also explored.

The attempt to extend the embedding strategy to non-precious metals, like Ni and Cu, is described. Ni/Cu-based catalysts are widely used in industrial application mainly due to their low costs and high availability. Ni(x%)Cu(y%)/Al_2O_3 catalysts with different Ni and Cu contents were also synthesized using the conventional impregnation method. All the samples were tested towards the steam reforming of methanol and ethanol, besides the partial oxidation of methane. The role and effect of Ni/Cu ratio on the chemical-physical properties and the catalytic performance were examined. The catalysts were characterized by means of surface area measurements, X-Ray Diffraction (XRD), Temperature Programmed Reduction (TPR), Transmission Electron Microscopy (TEM), Near Edge (XANES) and Extended X-Ray Absorption Fine Structure (EXAFS).

On Ni/Cu based catalysts, CO_2 hydrogenation was also studied. Taking into account the gap between the high pressure and ultra high vacuum environment (UHV), the results were compared to those obtained, on Ni single crystal (Ni(110)), under UHV conditions. The (110) surface of Ni is the most interesting because CO_2 adsorbs only upon this surface under UHV. At variance, CO_2 does not adsorb on any low index surface of copper single crystals. Interestingly, on a Ni/Cu(100) model catalyst, it was observed that the turnover frequency for CO_2 hydrogenation at Ni sites is 60 times

higher than at Cu sites. Moreover CO is essential for promoting Ni segregation to the surface. Even though it was found that Ni can be an excellent promoter for the reaction, clear understanding of the mechanism for carbon dioxide hydrogenation has not been yet achieved. This is the reason why our interest is the characterization of the reaction on Ni(110). In order to clearly understand the reaction mechanism, we aim at identifying the reaction intermediates and channels by means of X-Ray Photoelectron Spectroscopy (XPS), Temperature Programmed Desorption (TPD) experiments and High Resolution Electron Energy Loss Spectroscopy (HREELS).

References

[1] C. J. Campbell and J. H. Laherrere, Scientific American , 60-65. 1998.

[2] C. Song, Catalysis Today 115 (2006) 2.

[3] G. Centi and S. Perathoner, Heterogeneous catalytic reactions with CO_2: Status and perspectives. Studies in Surface Science and Catalysis, Elsevier, 2004.

[4] Energy Systems and Sustainability. Power for a Sustainable Future. (G. Boyle, B. Everett, J. Ramage, Eds.) Oxford University Press, 2003.

[5] R.U. Ayres, H. Turton, T. Casten, Energy 32 (2007) 634.

[6] M. Momirlan, T. Veziroglu, Renewable Sustainable Energy Reviews 3 (1999) 219.

[7] M. Momirlan, T.N. Veziroglu, International Journal of Hydrogen Energy 30 (2005) 795.

[8] R. Kothari, D. Buddhi, R.L. Sawhney, Renewable Sustainable Energy Reviews (2007).

[9] L. Zhou, Renewable Sustainable Energy Reviews 9 (2005) 395.

[10] L. De Rogatis and P. Fornasiero, Chapter 8, Catalysys Design for Reforming of Oxygenates, in Catalysis for Sustainable Energy Production. Wiley-VCH, 2008.

[11] T.K. Tromp, R.L. Shia, M. Allen, J.M. Eiler, Y.L. Yung, Science 300 (2003) 1740.

[12] M. Haruta, T. Kobayashi, H. Sano, N. Yamada, Chemistry Letters 16 (1987) 405.

[13] M. Haruta, The Chemical Record 3 (2003) 75.

[14] M. Haruta, Science and Technology in Catalysis 145 (2003) 31.

[15] M. Haruta, Cattech 6 (2002) 102.

[16] M. Haruta, Gold Bulletin 37 (2004) 27.

[17] D.H. Kim, M.C. Kung, A. Kozlova, S.D. Yuan, H.H. Kung, Catalysis Letters 98 (2004) 11.

[18] S.D. Lin, A.C. Gluhoi, B.E. Nieuwenhuys, Catalysis Today 90 (2004) 3.

[19] C.H. Christensen, B. Jorgensen, J. Rass-Hansen, K. Egeblad, R. Madsen, S.K. Klitgaard, S.M. Hansen, M.R. Hansen, H.C. Andersen, A. Riisager, Angewandte Chemie-International Edition 45 (2006) 4648.

[20] R. Burch, Physical Chemistry Chemical Physics 8 (2006) 5483.

[21] Nanocatalysis, (U. Heiz, U. Landman Eds.) Wiley, 2008.

[22] A.T. Bell, Science 299 (2003) 1688.

[23] R. Schlogl, S.B. Abd Hamid, Angewandte Chemie-International Edition 43 (2004) 1628.

[24] C. H. Bartholomew and R. J. Ferrauto, Fundamentals of Industrial Catalytic Processes. Wiley, 2006.

[25] G. A. Somorjai, Introduction to surface chemistry and catalysis. John Wiley & Sons, Inc., 1994.

[26] J. Mathiak, A. Hienzel, J. Roes, Th. Kalk, H. Kraus, H. Brandt, Journal of Power Sources 131 (2004) 112.

[27] Y. Seo, D.J. Seo, J.H. Jeong, W.L. Yoon, Journal of Power Sources 163 (2006) 119.

[28] Renewable Resourches and Renewable Energy: a Global Challenge. (M. Graziani and P. Fornasiero, Eds.) Taylor & Francis, New York, 2007.

[29] R.M. Navarro, M.A. Penia, J.L.G. Fierro, Chemical Reviews 107 (2007) 3952.

[30] J.L. Ayastuy, M.A. Gutierrez-Ortiz, J.A. Gonzalez-Marcos, A. Aranzabal, J.R. Gonzalez-Velasco, Industrial Engineering Chemistry Research 44 (2005) 41.

[31] P.H. Matter, U.S. Ozkan, Journal of Catalysis 234 (2005) 463.

[32] P.H. Matter, D.J. Braden, U.S. Ozkan, Journal of Catalysis 223 (2004) 340.

[33] I. Ritzkopf, S. Vukojevic, C. Weidenthaler, J.D. Grunwaldt, F. th, Applied Catalysis A-General 302 (2006) 215.

[34] L. Yong-Feng, D. Xin-Fa, L. Wei-Ming, International Journal of Hydrogen Energy 29 (2004) 1617.

[35] N. Iwasa, S. Masuda, N. Ogawa, N. Takezawa, Applied Catalysis A-General 125 (1995) 145.

[36] N. Iwasa, S. Arai, M. Arai, Catalysis Communication 7 (2006) 839.

[37] N. Iwasa, N. Takezawa, Topics in Catalysis 22 (2003) 215.

[38] M.N. Barroso, M.F. Gomez, L.A. Arrua, M.C. Abello, Applied Catalysis A-General 304 (2006) 116.

[39] P. Biswas, D. Kunzru, International Journal of Hydrogen Energy 32 (2007) 969.

[40] A. Carrero, J.A. Calles, A.J. no, Applied Catalysis A-General 327 (2007) 82.

[41] H.V. Fajardo, L.F.D. Probst, Applied Catalysis A-General 306 (2006) 134.

[42] S. Sanchez, R.M. Navarro, J.L.G. Fierro, International Journal of Hydrogen Energy 32 (2007) 1462.

[43] D.R. Sahoo, S. Vajpai, S. Patel, K.K. Pant, Chemical Engineering Journal 125 (2007) 139.

[44] J.A. Torres, J. Llorca, A. Casanovas, M. nguez, J. Salvado, D. Montane, Journal of Power Sources 169 (2007) 158.

[45] A. Erdohelyi, J. Rasko, T. Kecskes, M. Toth, M. Domok, K. Baan, Catalysis Today 116 (2006) 367.

[46] T. Montini, L. De Rogatis, V. Gombac, P. Fornasiero, M. Graziani, Applied Catalysis B-Environmental 71 (2007) 125.

[47] T. Sakakura, J.C. Choi, H. Yasuda, Chemical Reviews 107 (2007) 2365.

[48] Y. Zhang, J. Fei, Y. Yu, X. Zheng, Energy Conversion and Management 47 (2006) 3360.

[49] T. Inui, Catalysis Today 29 (1996) 329.

[50] G. Ertl and E. Knozinger. Handbook of Heterogeneous Catalysis, Vol. 4, p.1856,2004.

Chapter 2

Experimental setup

2.1 Materials

2.1.1 Catalyst synthesis

- **Rh@Al_2O_3**

The preparation of Rh(x wt.%)@Al_2O_3 systems was performed by embedding protected Rh nanoparticles into a nanostructured oxidic matrix.

In the case of the Rh(1 wt.%)@Al_2O_3 sample, the growth of the porous oxide around the Rh nanoparticles was obtained by a two step precipitation process of the corresponding metal hydroxide in the presence of the colloidal suspension of Rh nanoparticles as illustrated in Fig. 2.1.

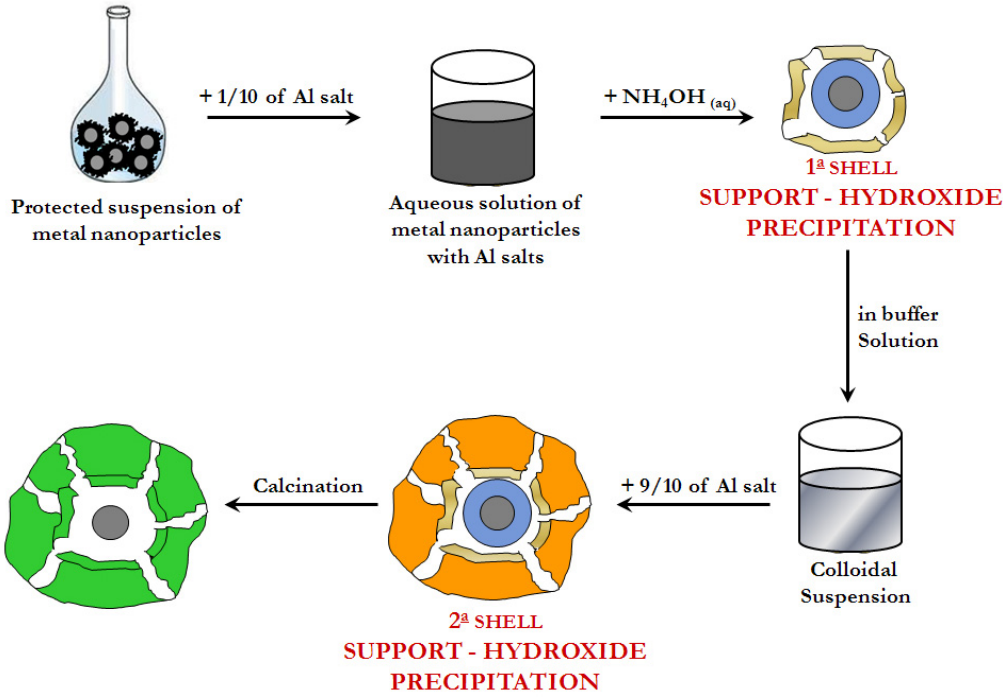

Figure 2.1: schematic representation of the synthesis of Rh@Al_2O_3.

The cationic surfactant N-hexadecyl-N-(2-hydroxyethyl)-N,N-dimethyl ammonium bromide (HEAC16Br), used for the synthesis of the noble metal nanoparticles suspension, was obtained by reaction of 1-bromohexadecane (99%, ACROS) with a 30% excess of N,N - dimethylethanolamine (99%, ACROS) in absolute ethanol (Carlo Erba) under reflux for 1 h [1], and purified by crystallization in absolute ethanol [2] (Yield 70 - 80%, m.p. 200 - 210 °C, ^{1}H-NMR and ^{13}C-NMR spectra as reported in Ref. [3]).

Stabilized Rh nanoparticles were first prepared under Ar at 25 °C, according to reported by Schultz *et al.* [4]. Briefly, an aqueous solution containing $NaBH_4$ (98+%, ACROS) and the cationic surfactant HEAC16Br was quickly added under vigorous stirring to an aqueous solution of $Rh(NO_3)_3 \cdot 2H_2O$ (Johnson Matthey). The suspension

was then stirred for 2 h to decompose the excess of reductant and finally added to 1/10 of the aqueous solution containing $Al(NO_3)_3 \cdot 9H_2O$ (≥ 98.0%, Fluka). The first layer of mixed hydroxide was precipitated dropping the obtained suspension into a 10 % (w/w) NH_4OH solution under vigorous stirring. After aging for 2 h, the precipitate was washed 4 times with NH_4OH/NH_4NO_3 buffer solution (pH = 10) to remove the Br^- ions. The precipitate was then suspended into NH_4OH/NH_4NO_3 buffer solution (pH = 10) and a second protective layer was grown by adding dropwise the remaining 90% of the support precursor solution. The final precipitate was aged overnight at room temperature, filtered, suspended in 2-propanol (electronic grade, Carlo Erba) and refluxed for 5 h in order to stabilize the textural framework of the support [5,6]. After filtration, the solid was dried at 120 °C overnight, crushed and sieved to collect the fraction smaller than 180 μm and calcined in a static oven, first at 500 °C for 5 h and, finally, at 900 °C for 5 h with heating ramps of 3 °C min^{-1}).

The Rh(x wt.%)@Al_2O_3 (with x = 33, 53, 67) model catalysts were obtained with a similar procedure depositing the aluminium hydroxide in a single step.

As references, standard impregnated Rh(1 wt%)/Al_2O_3 and Rh(33 wt.%)/Al_2O_3 catalysts were prepared. The Al_2O_3 support was synthesized using the procedure described above, with the exception that the Rh salt was not present. The obtained hydroxide was dried at 120 °C for 12 h. After calcination at 900 °C for 5 h, the metal was deposited by the conventional *incipient wetness* impregnation using a $Rh(NO_3)_3$ solution. After drying at 120 °C overnight, the material was calcined at 500 °C for 5 h (heating rate 3 °C min^{-1}).

- **Ni/Cu based catalysts**

Ni/Cu metals were supported on a commercial Al_2O_3 (Sasol HP 14-150 calc. 900 °C for 24 h with a specific surface area of 97 $m^2 g^{-1}$) by impregnation method using $Ni(NO_3)_2 \cdot 6H_2O$ (puriss. Fluka) and $Cu(NO_3)_2 \cdot 3H_2O$ (puriss. Fluka) as metal precursors.

Table 2.1: Ni_xCu_y based catalysts.

SAMPLE	ABBREVIATION
Ni(10%)/Al_2O_3	Ni_{10}-Al
Ni(7%)Cu(3%)/Al_2O_3	Ni_7Cu_3-Al
Ni(5%)Cu(5%)/Al_2O_3	Ni_5Cu_5-Al
Ni(3%)Cu(7%)/Al_2O_3	Ni_3Cu_7-Al
Cu(10%)/Al_2O_3	Cu_{10}-Al

Briefly, appropriate amounts of $Ni(NO_3)_2$ or/and $Cu(NO_3)_2$ were dissolved in ethanol. Aluminium oxide or ceria-zirconia mixed oxide was added to the metal/s solution under continuous stirring. The obtained slurry was dried under vacuum until nearly all the alcohol was evaporated and the solid residue was further dried overnight at 120 °C in air, crushed and sieved to collect the fraction smaller than 250 μm. Finally, the material was calcined in a static oven at 600 °C in air for 5 h (heating / cooling rates 3 °C min^{-1}). All the catalysts have a total nominal metal loading of 10 wt.%.

Table 2.1 summarizes Ni(x wt.%)Cu(y wt.%) samples prepared in this work. The final materials obtained are hereafter designated as Ni_xCu_y-Al, according to the support, where x and y represent the nickel and copper loading (wt. %), respectively.

2.1.2 Unsupported Ni/Cu

NiO (99.99 %, Sigma Aldrich), CuO (99.99 %, Sigma Aldrich) and Cu_2O (99.9 %, Alfa Aesar) were used.

2.1.3 Single crystal: Ni(110)

The sample is a disk with a diameter of 9 mm and a thickness of 1.5 mm. The desired surface was obtained as follows: an oriented crystal, a cylinder with a diameter of about 1 cm, was cut along a plane which is normal to the crystallographic direction identified by Miller index [110]. Subsequently, the surface was smoothed with diamond dust. The exact orientation was checked by X-ray powder diffraction technique. Finally, the sample was reduced in H_2 at 600 ° C for 24 h.

Two distinct Ni(110) samples were used for the XPS-TPD and EELS experiments.

In both cases, the surface was cleaned by several cycles of ion bombardment (Ar^+, p~ 1×10^{-6} mbar, E_k = 3 keV) and subsequent progressive annealing up to 1000 °C. Finally, in order to remove carbon contamination, the sample was exposed to O_2 (p~ 6.5×10^{-8} mbar) and heated up to 300 °C. This latter procedure was repeated more times. Surface order and cleanliness were checked by LEED and XPS, respectively.

2.2 Characterization

2.2.1 Classical techniques

The BET surface area, pore volume and average pore diameter of the catalysts were measured by N_2 adsorption at liquid nitrogen temperature using a Micromeritics ASAP 2020. Approximately 100 mg of catalyst, previously degassed overnight at 350 °C, were used for each analysis.

Powder XRD (X-Ray Diffraction) patterns of the samples after calcination and activation / reduction at 750 °C for 2 h were recorded with a computer-controlled Philips X'Pert diffractometer using Cu Kα radiation (λ = 0.154 nm). The data were collected at 0.02 ° in the (2θ) range from 10° to 100°.

Transmission Electron Microscopy (TEM) characterizations were performed at the Chemistry Department of Cagliari University in collaboration with Dr. M.F. Casula. TEM bright field (BF) and dark field (DF) images and selected-area electron diffraction (SAED) patterns were obtained on a JEOL 200CX Transmission Electron Microscope equipped with a tungsten cathode operating at 200 kV. Finely ground samples were dispersed by sonication in n-octane and dropped and dried on a carbon-coated copper grid.

Temperature Programmed Reduction (TPR) experiments were performed on ~30 mg of the calcined materials. The samples were pre-treated at 500 °C for 1 h by pulsing of O_2 in an Ar flow every 75 s, then purged with Ar at 500 °C for 15 min and cooled to RT. The O_2 pulses were stopped when the sample temperature was lower than 150 °C. H_2(5%)/Ar was admitted into the reactor and the flow allowed to stabilise for 30 min before increasing the temperature to 900 °C at 10 °C min^{-1}. After TPR, the samples were outgassed under Ar flow at 900 °C for 15 min and cooled to 427 °C, at which temperature oxidation was carried out with pulses of diluted O_2 for 1 h. The TPR/oxidation procedure was repeated other 2 times. The re-oxidation step of the second cycle was conducted at 600 °C while the third cycle was performed at 900 °C and prolonged for 5 h in order to evaluate the effect of more severe conditions. H_2 consumption was monitored using a Thermal Conductivity Detector (TCD), the response of which was calibrated with CuO.

Near edge (XANES) and extended (EXAFS) X-ray absorption spectra were collected at the XAFS beamline at the Elettra synchrotron facility in Trieste operating at 2.0 GeV and 100–300 mA. All spectra were recorded at room temperature (RT) in transmission mode with a Si(111) double crystal monochromator and using ionization chambers as detectors. The resolving power was $E/\Delta E$ 10^4, and the photon flux at the sample was 10^{10} photons s^{-1}. Angle/energy calibration was checked by simultaneously measuring a Ni and Cu metal foil absorption spectrum between the second and the third ionization chamber. The gas mixtures in the ionization chamber were chosen in order to optimize signal over Ni-Cu edges.

XANES spectra were recorded with an energy sampling step from 0.1 to 1 eV and an integration time of 2 s per point over the range 8000-9500 eV for the Ni K edge and 8600-10200 eV for the Cu K edge. The spectra at the edge jump were fitted by a linear combination of the reference materials for the oxidized and the reduced state of Ni and Cu to estimate the molar fraction of reduced and oxidized metals [7]. EXAFS spectra were recorded with an energy sampling step from 2 to 5 eV, and an integration time of 2 s per point over the range 8000-9500 eV for the Ni K edge and 8600-10200 eV for

the Cu K edge. XANES and EXAFS data analysis were performed with Athena and Artemis programs included in the Ifeffit packages. In order to obtain the coordination numbers and subsequently an estimation of particles size accordingly to Ref. [8], EXAFS first shell analysis was performed on samples at Ni and Cu edges. A spherical shape geometry for metal particles was assumed.

2.2.2 Ultra high vacuum setup

CO_2/H_2 and CO_2/H_{at} experiments were carried out in two different UHV chambers.

XPS and TPD analyses were performed in the laboratory of Surface Structure and Reactivity Group of the Physics Department of the University of Trieste.

A multipurpose apparatus was used with a base pressure of 5 x 10^{-11} mbar and equipped with LEED and spot profile analysis (SPA)-LEED optics, residual gas analyzer for TPD measurements, a conventional Mg *Kα* x-ray source ($h\nu$ = 1253.6 eV, ΔE = 0.9 eV) and a VG MKII hemispheric electron energy analyzer. The sample was mounted on a four degrees of freedom manipulator, resistively heated, and cooled down to -180 °C by liquid nitrogen.

The atomic hydrogen beam was generated by a homemade Bischler and Bertel type thermal cracker (Fig. 2.2) [9,10].

Figure 2.2: atomic hydrogen source

After normalization and background subtraction, the XPS spectra were fitted with Doniach–Sunjic line shapes convoluted with a Gaussian function [11]. Binding energies were calibrated with respect to the position of the Ni $2p_{3/2}$ peak of the clean sample (852.3 eV).

XPS measurements on Rh(x wt.%)@Al_2O_3 powders were also performed. Due to the high metal loading of these samples, the charging effect was limited to few eV, without, consequently, the need to use an electron gun. In this case, the binding energies were calibrated with respect to the position of the C1s (284.8 eV).

HREELS experiments were performed in the laboratory of prof. M. Rocca at the Physics Department of Genova University. A dedicated chamber was used with a base pressure of 1.5 x 10^{-10} mbar and equipped with a commercial LEED optics (OCI), a XPS facility (ESCA Omicron), and a EELS spectrometer (SPECS). Here, the sample was heated by both electron bombardment and irradiation from a tungsten filament, while cooling was performed by liquid nitrogen. HREELS spectra were recorded in specular configurations, with a primary electron energy of 3.0 eV and an incidence angle of 62°. In order to maximize the signal from the low reflectivity, disordered CO_2/H layer, the instrument was operated at resolution around 5 meV. HREELS spectra were normalized with respect to the specular peak.

2.3 Reaction conditions

2.3.1 Standard environment

All catalytic tests were conducted at atmospheric pressure in a conventional fixed bed reactor (U-shaped quartz microreactor with internal diameter of 4 mm). The temperature of the catalyst was measured with a K-type thermocouple. Before testing the catalytic activity, the calcined materials were pre-treated under O_2(5%)/Ar at 500 °C for 1 h (40 mL min^{-1}, 10 °C min^{-1}) and activated by reduction in H_2(5%)/Ar at 750 °C for 2 h (40 mL min^{-1}, 10 °C min^{-1}).

In the case of MPO experiments 100 mg of calcined sample were typically used. Gas flow rates were ~83 mL min^{-1} to ensure Gas Hourly Space Velocity (GHSV) values of ~50000 mL g^{-1} h^{-1}. The CPOM feed was composed of 2.0 vol.% CH_4 and 1.0 vol.% O_2 diluted in Ar. The products and reactants were quantified using a HPR20 Hyden mass spectrometer as detector. The gaseous mixture was introduced in the reactor at RT for 30 min, before ramping the furnace temperature to 900 °C at 5 °C min^{-1}. After 20 min at 900 °C, the furnace was cooled to RT.

CH_4 temperature programmed desorption (TPD) experiments were carried out using 51 mg of the catalyst. Gas flow rates were ~42 mL min^{-1} to ensure Gas Hourly Space Velocity (GHSV) values of ~50000 mL g^{-1} h^{-1}. The feed, composed by CH_4 (2.0 vol.%) diluted in Ar, was introduced in the reactor at RT before ramping the furnace temperature to 900 °C at 10 °C min^{-1}.

In alcohols steam reforming experiments ~120 mg of catalyst were typically used. EtOH/H_2O 1:5 and MeOH/H_2O 1:4 mixtures were injected into an Ar flow with a Hamilton Gastight syringe using a INSTECH Model 2000 syringe pump. All the

transfer lines between syringe, reactor and GC were kept at 120 °C. Gas flow rates were ~31 mL min^{-1} to ensure GHSV values of ~16000 mL g^{-1} h^{-1}. On-line GC analysis was performed using a Hewlett Packard 5890 Series II gas chromatograph. A Molsieve 5A column, with Ar as carrier, was connected to a thermal conductivity detector (TCD) to analyse H_2, O_2, N_2, CH_4 and CO. A Select Permanent Gases/CO_2 PLOT column (parallel PoraPLOT 50 m x 0.53 mm ID and Molsieve 5A 10 m x 0.53 mm ID column) with He as carrier and connected in series to a methanator and to a flame ionization detector (FID) was used to analyze the carbon-containing compounds. C balance was always within ±2%.

The gaseous mixture was first introduced in the reactor at 150 °C, before ramping the furnace temperature to 700 °C at 0.7 °C min^{-1}.

H_2 yield was calculated on the basis of the stoichiometry of the following reactions (Eq. 2.1 for MeOH-SR; Eq. 2.2 for EtOH-SR), which include the water gas shift:

$$CH_3OH + H_2O = CO_2 + 3H_2 \qquad (2.1)$$

$$CH_3CH_2OH + 3H_2O = 2CO_2 + 6H_2 \qquad (2.2)$$

$$\text{H}_2\text{ yield} = \frac{1}{3}\ \frac{\text{mol}(\text{H}_2)\text{produced}}{\text{mol(MeOH)in the feed}}$$

$$\text{H}_2\text{ yield} = \frac{1}{6}\ \frac{\text{mol}(\text{H}_2)\text{produced}}{\text{mol(EtOH)in the feed}},$$

while the yield of all C containing products accordingly to:

$$\text{C product yield} = \frac{\text{moles of C product}}{\text{moles of C in the feed}}.$$

CO_2/H_2 experiments were performed using a CO_2 (10.0 vol.%)/H_2 (60.0 vol.%)/Ar (30.0 vol.%) stream (GHSV = 6000 mL g^{-1} h^{-1}). The gaseous mixture was introduced in the reactor at RT for 30 min, before ramping the furnace temperature to 800 °C at 20 °C min^{-1}. Reaction products were detected with the mass spectrometer and the gaschromatograph. CO_2 temperature programmed desorption (TPD) measurements were also carried out in the same temperature range.

2.3.2 Ultra high vacuum environment

All TPD spectra were performed with a linear temperature ramp of 1.5 °C s^{-1}, while XPS and HREELS spectra were collected as a function of the annealing temperature after exposure of the clean surface to 4 L of CO_2 and to 4 L of CO_2 plus 10 L of H_2/H_{at} at -180 °C and subsequently heated to increasing temperatures. "L" (Langmuir) is the convenient unit used to express the gas exposure, a measure of the amount of gas which a surface has been subjected to (1 L = 10^{-6} Torr s). The coverage of a fixed species on a surface, instead, is expressed in "monolayer" (ML). A monolayer of adsorbate corresponds to an atom/molecule of adsorbate per surface atom.

References

[1] A.B. Scott, H.V. Tartar, Journal of the American Chemical Society 65 (1943) 692.

[2] C.A. Bunton, L.G. Ionescu, Journal of the American Chemical Society 95 (2004) 2912.

[3] A. Roucoux, J. Schulz, H. Patin, Advanced Synthesis and Catalysis 345 (2003) 222.

[4] J. Schulz, A. Roucoux, H. Patin, Chemistry-A European Journal 6 (2000) 618.

[5] S.L. Jones, C. Norman, Journal of the American Chemical Society 71 (1988) C190.

[6] D. Segal, Journal of Materials Chemistry 7 (1997) 1297.

[7] T. Shido, M. Lok, R. Prins, Topics in Catalysis 8 (1999) 223.

[8] S. Calvin, S.X. Luo, C. Caragianis-Broadbridge, J.K. McGuinness, E. Anderson, A. Lehman, K.H. Wee, S.A. Morrison, L.K. Kurihara, Applied Physics Letters 87 (2005) 1.

[9] U. Bischler, E. Bertel, Journal of Vacuum Science and Technology A 11 (1993) 458.

[10] C. Eibl, G. Lackner, A. Winkler, Journal of Vacuum Science and Technology A 16 (1998) 2979.

[11] S. Doniach, M. Sunjic, Journal of Physics C-Solid State Physics 3 (1970) 185.

Chapter 3

Rh embedded into Al_2O_3

3.1 Catalysts design: embedding strategy

The severe working conditions often encountered in H_2 production processes (e.g. high temperature, high space velocity) combined with the necessity of long catalyst lifetime, requires the development of an appropriate synthesis procedure able to guarantee high catalyst thermal stability. Supported metal catalysts are usually prepared through impregnation of a porous support with a solution of the metal (or metal oxide) precursor followed by proper chemical and thermal treatments. Although the most attractive feature of this route is its simplicity, in the practical execution, both in laboratory and industrial scale, it does not prevent catalyst's easy deactivation due, for instance, to the active phase sintering. In the case of non-precious metal-based catalysts, high metal loadings can be used to overcome deactivation induced by sintering. Commercial Ni-based systems, for instance, can contain up to 30 wt% of metal. It is clear that the same approach cannot be employed for noble metals. A possible option in this case is the design of a catalyst with a very high metal dispersion, which must be stable under reaction conditions through a strong interaction between the active phase and the support. This would allow metal loadings to be lowered to values acceptable for commercial applications. Indeed, up to now, the high market cost of noble metals, together with their low natural abundance, limits their industrial scaling-up.

Recently, great attention has been dedicated to the development of novel synthesis methods for the preparation of nanostructured catalysts with higher activity and thermal stability than those available. The Solid Phase Crystallization (SPC) technique is one of the proposed approaches. The SPC strategy is based on the preparation of a crystalline oxide precursor (generally perovskite or hydrotalcite compounds) by sol-gel or co-precipitation methods in the presence of ions of the active metal. After calcination, the material contains species of the active metal, homogeneously dispersed inside the bulk. Subsequent reduction at high temperature leads to the migration of most of the metal atoms to the surface, forming small metallic particles which are homogeneously dispersed. It has been indicated that the metal–support interaction is stronger than that obtainable by the usual impregnation or deposition methods. Using SPC, active and thermally stable catalysts have been produced for reforming reactions involving methane [1-12] and methanol [13].

The microemulsion is another synthesis route which shows interesting advantages related to the possibility of controlling properties such as particle size, morphology and size distribution. Nanosized particles with a narrow size distribution can often be achieved with consequent benefits for catalytic reactions. Although this synthetic strategy is quite successful in producing active and stable catalysts, it usually requires large quantities of expensive reagents which have to be then removed during post synthesis treatments.

An innovative and elegant approach, recently adopted for instance by Corma and co-workers [14] and by Burch *et al.* [15], is based on the incorporation of the metal nanoparticles into an open shell of support (oxide) in order to limit the sintering of the particles at high temperature as depicted in Figure 3.1.

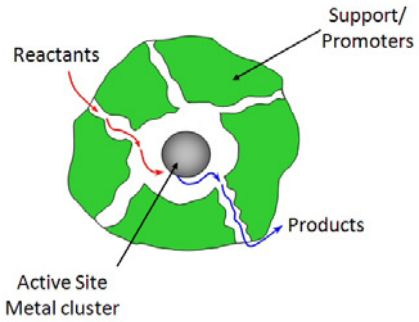

Figure 3.1: model of embedded catalyst

In the ideal situation, the porous nature of the inorganic matrix prevents the total occlusion of the particles favoring accessibility of the catalytic sites to the reactants. Adopting a modified sol-gel procedure, Corma et al. prepared Au nanoparticles embedded in silica [14]. In particular, the synthesis involves the formation of a three-component metal-organic structure composed of Au nanoparticles that are capped with alkanethiols and partially functionalized groups, and polymerized with tetraethyl orthosilicate. Alkanethiols reduce the tendency of Au particles to aggregate [16]. Moreover the particles reveal a narrow size distribution centered at approximately 2 nm. The reduced dimensions of Au particles together with the strong interaction with the support is an important factor to convert the inert gold into highly active catalyst [17-20]. The material obtained in this way shows high activity in the oxidation of CO and in the WGSR [14].

Using the same catalyst design, a simple and low cost strategy was designed for the synthesis of efficient and stable embedded Rh based catalysts for catalytic partial oxidation of methane and steam reforming of ethanol [21-24]. The proposed method has a strong flexibility offering the possibility to modulate the nature of the support and its texture and the inclusion of extra components (e.g. ceria-based mixed oxides as promoters) in the catalyst formulation.

Rh(1 wt.%)@Al_2O_3 was obtained through a co-precipitation procedure composed by two synthetic parts. In the first part a stable suspension of protected metal nanoparticles is obtained according to the method reported in the literature by Schulz and coworkers [25-27]. The metal particles were prepared in the presence of a highly water-soluble ionic surfactant (N-hexadecyl-N-(2-hydroxyethyl)-N,N-dimethyl ammonium bromide (HEAC16Br)) which is able, due to its nature, to modulate the size of particles and to prevent their aggregation. In general, a surfactant is an organic compound that is amphipathic, meaning it contains both hydrophobic groups (their

tails) and hydrophilic groups (their heads). Due to its molecular structure it is able to assemble in solution into micelles (Fig. 3.2).

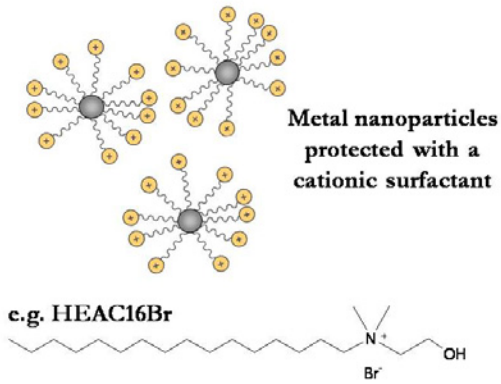

Figure 3.2: micelles model

In water, the tails of the surfactant form a core that is like an oil droplet, while its heads form an outer shell which maintains favorable contact with water. The charged heads of ionic surfactant prevent micelle aggregation. Notably, in the absence of the stabilizer, aqueous particle dispersion is inherently unstable because of the formation of aggregates. The strong tendency to form aggregates is caused by attractive van der Waals forces, which basically always act at short separation distances between particles in water. Modifying parameters like pH, temperature and surfactant concentration, it is possible to tune the metal particle size [23].

The surfactant plays a key role also in controlling the encapsulation of pre-formed metal particles, which represents the second part of the synthesis. During this phase, the growth of the porous oxide layers around metal nanoparticles also takes place. A crucial aspect during this synthetic part is the addition of the Al salt to the Rh nanoparticle suspension. Indeed, particular attention must be dedicated to the stability of micelles which protect the metal particles. Depending on the nature of the stabilizing forces, aggregation may be triggered by an increase in the ionic strength or changes in the solution pH. At a high concentration of salt ions, the particle charge can be screened, and the repulsive electrostatic force can be overcome by the attractive van der Waals force. In a previous investigation [21,24], we highlighted that the addition of Al salt, during the production of the $Rh(1\%)@Al_2O_3$ catalyst, leads to a drastic decrease of the pH and a strong increase of the ionic strength of the solution. As the ionic strength is increased, the electrostatic repulsive forces are progressively reduced allowing micelles collisions. Consequently, the stability of the micelles can decrease under these conditions, leading to a partial coalescence of the metal nanoparticles. The short inter-particle distances determine the aggregation behavior as suggested by HRTEM characterization [21]. In the present work, in order to avoid these unwanted effects, the porous oxide was realized in a two step process. In particular, metal nanoparticles were

covered with a first thin hydroxide layer on which, then, a second and more thicker protective layer was grown. Although HRTEM characterizations of this system are still in progress, catalytic tests (see § 3.2) suggest that a better incorporation and preservation of particle sizes mainly due to the milder conditions of pH and ionic strength during the synthetic procedure was achieved. This sample will be designated in the next sections as Rh(1%)@Al_2O_3-2-shell to distinguish it from Rh(1%)@Al_2O_3-1-shell obtained by a single step hydroxide precipitation and from Rh(1%)/Al_2O_3 prepared by conventional impregnation procedure.

3.2 Embedded catalyst characterization

The textural properties of Rh(1%)@Al_2O_3-2-shell are similar to those of Rh(1%)@Al_2O_3-1-shell as shown in Table 3.1.

The sample presents Type IV isotherms with hysteresis loops, typical of mesoporous materials [28]. The t-plot analysis indicates that the microporous volume is always negligible, while BJH analysis reveals that the material has a bimodal pore distribution, with maxima centred near 18 nm (main) and 6 nm. The embedded catalyst shows a high surface area (156 $m^2 g^{-1}$) consistently with Rh(1%)@Al_2O_3-1-shell.

Table 3.1: results of N_2 physisorption at -196 °C on the embedded catalysts after calcination at 900 °C for 5 h.

SAMPLE	S_{BET} [a] ($m^2 g^{-1}$)	d_M [b] (nm)	Cumulative Pore Volume ($mL g^{-1}$)
Rh(1%)@Al_2O_3 1 shell	157	6/18	0.79
Rh(1%)@Al_2O_3 2 shell	156	6/18	0.78

[a] BET surface area
[b] Pore diameter: maximums of the bimodal pore distribution

The analysis of the XRD pattern (data not shown) of Rh(1%)@Al_2O_3-2-shell after calcination indicates a composition of approximately 50% γ-Al_2O_3 and 50% θ-Al_2O_3. The mean crystallite size, determined following the Scherrer equation, is ~ 6 nm for γ-Al_2O_3 and ~ 7 nm for θ-Al_2O_3. Phases related to the presence of Rh species were not identified.

Figure 3.3 reports the Temperature Programmed Reduction (TPR) profiles of Rh(1%)/Al_2O_3 (a), Rh(1%)@Al_2O_3-1-shell (b) and Rh(1%)@Al_2O_3-2-shell (c). The presence of significant consumption of H_2 during the TPR experiments confirms that the Rh nanoparticles are converted into RhO_x species during the calcination treatment

at 900 °C. Consequently, in order to obtain active metallic Rh nanoparticles, an appropriate activation procedure is necessary.

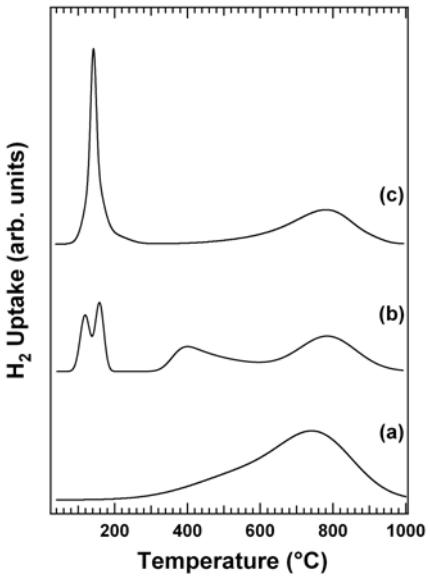

Figure 3.3: temperature programmed reduction profiles of the samples after calcination and standard cleaning in O_2 (5%)/Ar at 500 °C for 1 h: (a) impregnated Rh(1%)/Al_2O_3, (b) embedded Rh(1%)@Al_2O_3-1-shell, (c) Rh(1%)@Al_2O_3-2-shell.

The different types of RhO_x formed from the oxidation of metallic clusters dispersed on the surface of Al_2O_3 were extensively studied by Hwang *et al.* using the TPR technique [29]. It was shown that, increasing the oxidation temperature, the reduction peaks move to higher temperatures. The different reduction temperature of RhO_x species was related to a different interaction with the support: the stronger the interaction, the higher the reduction temperature. It was indicated that the nature of the RhO_x can range from O atoms adsorbed on the surface of metallic Rh (that reduces at sub-ambient temperature) to $Rh(AlO_2)_y$ species (that reduce at very high temperature) obtained from the diffusion of RhO_x into the atomic layers of Al_2O_3 during high temperature oxidation. It is worth noting that Wang *et al.* [30] reported that Rh nanoparticles supported on γ-Al_2O_3 are oxidized at temperatures higher than 430 °C to form different species depending on their diameter, RhO_2 for Rh nanoparticles bigger than 1.5 nm or Rh_2O_3 for the smallest nanoparticles.

A clear attribution of each reduction peak to well-defined species is difficult due to the several factors which are involved. However, the comparison of the samples allows interesting qualitative considerations.

The Rh(1%)@Al_2O_3-1-shell sample presents a structured TPR profile, characterized by different reduction peaks centered at 120, 160, 400 and 790 °C. The

reduction peaks at 120 and 160 °C can be associated to RhO_x species exposed on the surface of Al_2O_3. The different reduction temperature could be ascribed to a different interaction with the support [29] and/or with a different dimension of the RhO_x crystallites [31]. A reduction peak around 400 °C is not reported by Hwang et al. [29] but is present in the TPR profiles of an hydrotalcitic precursor containing Rh prepared by Basile *et al.* [4]. In this sample Rh^{3+} ions were homogeneously dispersed into the hydrotalcitic matrix. According to these data, it seems reasonable to ascribe the reduction peak at 400 °C in the TPR of Rh(1%)@Al_2O_3-1-shell catalyst to RhO_x species occluded into the Al_2O_3 matrix. Finally, the reduction peak around 790 °C is indicative of the presence of stable Rh species, such as the $Rh(AlO_2)_y$ species reported by Hwang et al. [29].

On the other hand, the Rh(1%)@Al_2O_3-2-shell sample shows two major reduction peaks centered at 140 and 780 °C. The presence of a single, symmetric reduction peak at 140 °C is indicative of a high homogeneity of the RhO_x species exposed on the surface of the Al_2O_3 matrix. Notably, the growth of the oxidic matrix in 2 steps was developed to avoid the coalescence of the nanoparticles during the addition of the Al salt and to improve their homogeneity in the final materials. No reduction peaks are observed around 400 °C, indicating the absence of RhO_x species deeply occluded into the Al_2O_3 matrix. The reduction peak centered at 780 °C suggested the formation of some $Rh(AlO_2)_y$ species [29].

Additionally, the TPR experiments highlight that the redox behavior of the embedded catalysts is significantly different to that of the impregnated sample. The TPR profile of the Rh(1%)/Al_2O_3 material is characterized by a single extended reduction process centered around 750 °C, indicating a strong interaction between the Rh species and the support. These data suggest the effectiveness of the embedding strategy in preventing high mobility of active phase into the support.

3.2 Catalytic properties improvement

Figure 3.4 presents the results of MPO in a run-up experiment on the embedded Rh(1%)@Al_2O_3-2-shell. Almost identical reaction profiles are observed for Rh(1%)@Al_2O_3-1-shell and Rh(1%)/Al_2O_3 [21,24].

CH_4 and O_2 conversion starts around 260 °C. O_2 is completely converted around 370 °C while CH_4 conversion reaches 25%. Up to this temperature, the only detectable products are CO_2 and H_2O. CO and H_2 are observed only when O_2 is fully converted. Above 370 °C, CH_4 conversion increases continuously and above 700 °C full methane conversion is observed.. While CH_4 conversion increases, CO and H_2 yields grow and the H_2O yield decreases. Meanwhile, CO_2 yield remains almost constant (around 25%) up to 460 °C and starts to diminish above this temperature. Consequently, the CO and

H_2 selectivity increases above 460 °C while the CO_2 one decreases. The observed products distribution is consistent with a reaction pathway involving the combustion – reforming reactions, as previously reported for other Rh catalysts supported on Al_2O_3-based oxides [8,9,32,33].

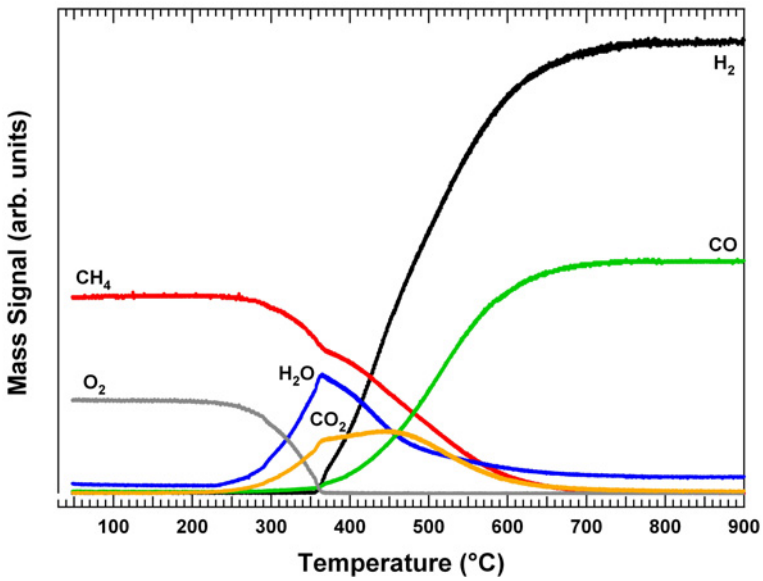

Figure 3.4: catalytic activity of the embedded Rh(1%)@Al_2O_3-2-shell catalyst under MPO conditions (CH_4 (2.0%) + O_2 (1.0%) in Ar, GHSV = 700000 mL g^{-1} h^{-1})

Despite their similar reactivity during the first run-up experiments, the impregnated and embedded Rh catalysts present significant differences in their stability under MPO conditions, either under consecutive run-up experiments or during isothermal reaction at high temperature for a long time.

Both embedded systems show a constant reactivity profile during at least 6 consecutive run-up experiments. On the contrary, the impregnated Rh(1%)/Al_2O_3 catalyst is characterized by a progressive worsening of its catalytic performance, with a significant decrease of the CH_4 conversion above 550 °C (data not shown) [21].

The stability of the catalytic activity under isothermal conditions was tested at 750 °C after 6 run-up experiments. As reported in Figure 3.5, the deactivation begins immediately for Rh(1%)/Al_2O_3 system, while the catalytic activity of Rh(1%)@Al_2O_3-1-shell sample remains constant for at least 60 h. After this period of time, the CH_4 conversion starts to decrease slowly. In the case of the Rh(1%)@Al_2O_3-2-shell catalyst, the conversion of CH_4 at 750 °C is complete and constant for at least 150 h, more then twice longer with respect to the performance of the Rh(1%)@Al_2O_3-1-shell catalyst. This result suggests that the synthesis modification (2-shell vs. 1-shell) induced a significant improvement in the catalyst stability under reaction conditions.

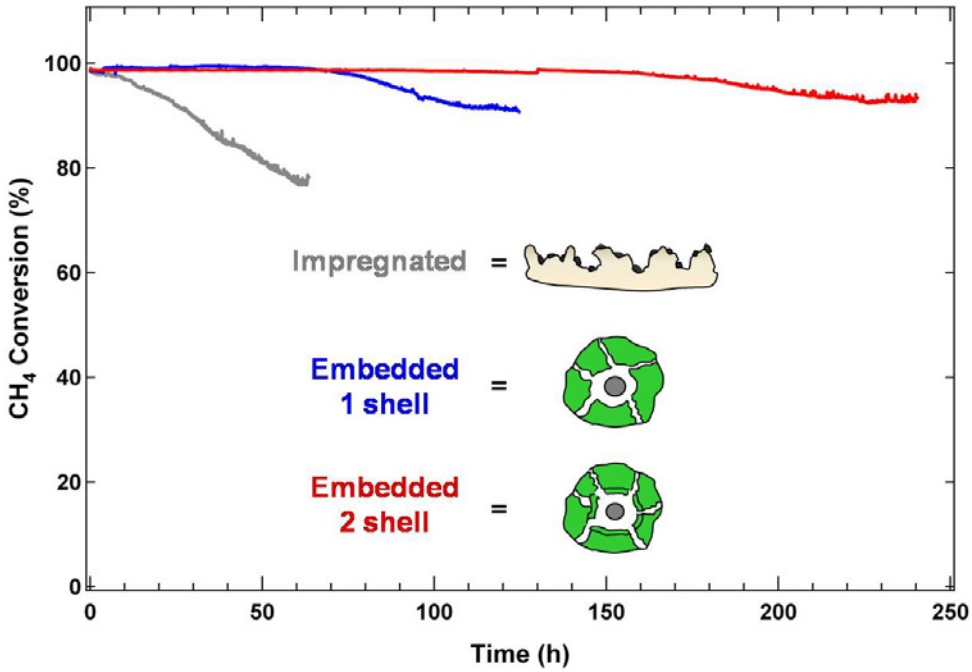

Figure 3.5: stability of the catalytic activity of the embedded Rh(1%)@Al_2O_3-1-shell, Rh(1%)@Al_2O_3-2-shell and the impregnated Rh(1%)/Al_2O_3 catalysts under MPO conditions at 750 °C (CH_4 (2.0%) + O_2 (1.0%) in Ar, GHSV = 700000 mL g^{-1} h^{-1}).

The higher thermal stability of the embedded systems with respect to the traditional catalyst obtained by incipient wetness impregnation, can be correlated to the protection offered by the surrounding layer of porous oxide which prevents extensive sintering of the active metal phase. However, some coke deposition is also observed leading to a partial deactivation of the catalytic activity. This partial deactivation is essentially reversible: an in situ treatment with O_2 at high temperature (850 °C) is able to restore the properties of the catalyst almost completely [21]. On the contrary, the deactivation observed on the impregnated Rh(1%)/Al_2O_3 sample is mainly irreversible. In this case, the major factor inducing the catalyst decay is the sinterization of the metal phase and/or the incorporation of Rh into the Al_2O_3 lattice during high temperature treatments.

Concerning the catalytic behavior under isothermal conditions of Rh(1%)@Al_2O_3-2-shell system with respect to Rh(1%)@Al_2O_3-1-shell, the improvement in the catalyst life time could be correlated with several factors.

On Rh(1%)@Al_2O_3-1-shell sample, the observed deactivation was proved to be mainly due to coke deposition [21]. It was reported that methane partial oxidation entails a network of structure sensitive reaction steps including C-H and C-O bonds breaking [34]. Some of these steps play a key role in carbon accumulation on the

catalyst surface. The rate of C-forming and C-reforming reactions, as well as the balance between these two processes, are a function of both the metal particle size and the reaction temperature [34]. Particles with different shape or size expose different surface planes to the reactant and each of them shows a peculiar catalytic activity due to different active sites involved. In the present work, the effect could be due to a lower rate of coke deposition on 2-shell system with respect to 1-shell.

Although with less extent, over Rh(1%)@Al_2O_3-1-shell catalyst, the deactivation is also caused by the sintering of the support and the active phase [21]. As indicated by the HRTEM characterization for the Rh(1%)@Al_2O_3-1-shell system, it is possible to distinguish various types of Rh nanoparticles: (a) particles on the external surface on the alumina support; (b) partially embedded particles and (c) deeply embedded particles [21]. The distribution of these species, which have different mobility and, consequently, different thermal stability against sintering, could be not the same as in the Rh(1%)@Al_2O_3-2-shell sample. In the latter case, it seems reasonable to expect a better incorporation of the metal particles into oxidic matrix and a better preservation of particle size (e.g. more uniform distribution (see TPR, § 3.2) during the subsequent chemical and thermal treatments. In addition, the undesirable incorporation of Rh into the Al_2O_3 lattice, during long-term high temperature treatments, could also be further reduced.

3.4 Study of model embedded systems

An XPS study on model embedded Rh systems has been carried out in order to obtain a better understanding of the interaction between Rh and the alumina support as previously explained in § 1.5. One of the main tasks was the characterization of the electronic density of the rhodium atoms in the particles embedded into alumina with respect to those on the surface of the support.

We designed three system to simulate different degrees of coverage, i.e. Rh nanoparticles surrounded by a thin or even incomplete porous alumina layer or by a thicker protecting oxide capping (Table 3.1). The theoretical number of the alumina layers around each particle was estimated as follows. We assumed a spherical shape for the metal particles and we considered an average diameter of 2 nm, which is slightly higher with respect to that of the protected nanoparticles in solution [21,24] and similar to that observed in the reduced Rh(1 wt.%)@Al_2O_3-1-shell [21]. Based on these assumptions, we calculated the exposed metal surface area of the Rh(1 wt.%)@Al_2O_3 sample. Considering for simplicity the surface (0001) of α-Al_2O_3, the area of one alumina unit cell and the number of unit cells needed to cover the metal surface area, we estimated. From the amount of alumina needed to obtain a theoretical monolayer,

we selected a sample chemical composition leading ideally to about 1, 2.5 and 5 monolayer of alumina capping (Tab 3.1).

Table 3.1: embedded model systems and theoretical monolayer of alumina around the metal nanoparticles.

Metal loading* **wt.%**	**n. layer**
1	236
33	5
53	2.5
67	1

* with respect to the amounts of alumina in the final system

The high metal loadings allowed good XPS measurements without significant charging effects.

Fig. 3.6 displays XPS spectra of the Rh ($3d_{3/2}$, $3d_{5/2}$) region of Rh(33%)@Al_2O_3 (A), Rh(53%)@Al_2O_3 (B) and Rh(67%)@Al_2O_3 (C) model catalysts. The components contributing to the peaks are also depicted, as obtained by the deconvolution procedure.

After calcination in air at 900 °C for 5 h (upper panel), all of Rh is oxidized to Rh^{3+} (e.g. Rh_2O_3) as indicated by the binding energy value of the Rh $3d_{5/2}$ peak at 308.2 eV [35-38]. The presence of the bulk oxide phase is quite reasonable, since the model catalysts were calcined in air at relatively high temperature. This result is also supported by XRD data. Fig. 3.7 reports, as an example, the XRD pattern for the Rh(53%)@Al_2O_3 sample (left panel), which shows the characteristic diffraction peaks of the Rh_2O_3 phase. No other species related to Rh (e.g. RhO_2) were detected by XRD. Noteworthy, due to the very high metal content, the XRD peaks of the support cannot be clearly distinguished.

In the case of Rh(33%)@Al_2O_3 and Rh(53%)@Al_2O_3, a minor component at 310.0 eV is also found in the XPS spectra, associated to the presence of Rh^{4+} (e.g. RhO_2) species [39]. This contribution was not observed in the XRD patters, mainly due to the detection limit of the technique.

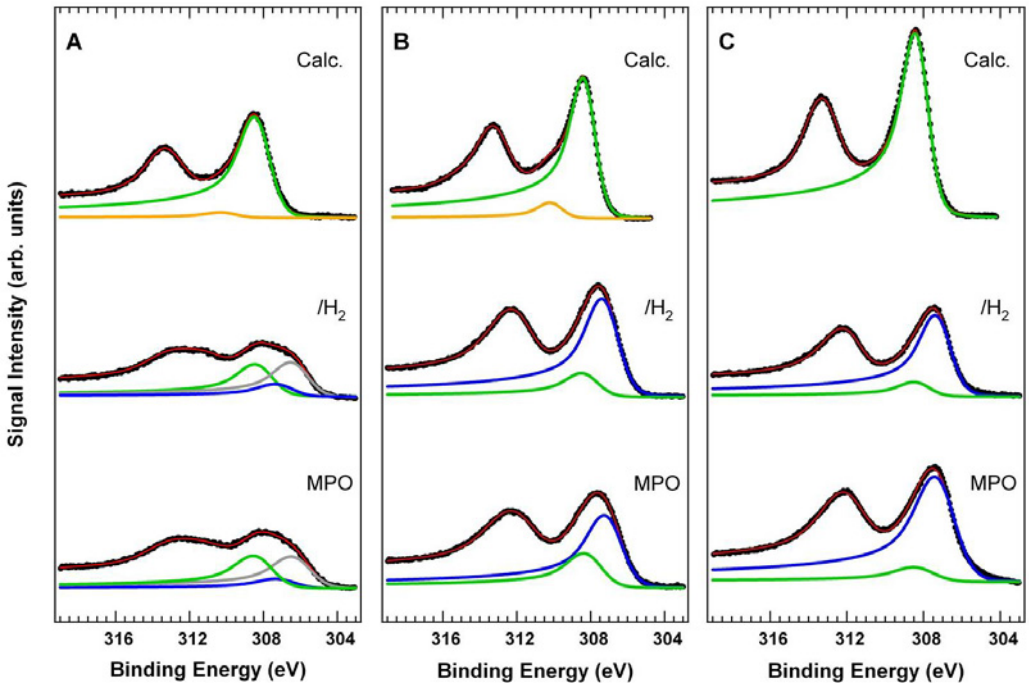

Fig. 3.6: XPS spectra of the Rh 3*d* core-level of (A) Rh(33%)@Al_2O_3, (B) Rh(53%)@Al_2O_3 and (C) Rh(67%)@Al_2O_3 after calcination in air at 900 °C x 5 h (top), activation in H_2 at 750 °C x 2 h (center) and aging under MPO conditions (bottom).

The H_2 treatment at 750 °C for 2 h (middle panel in Fig. 3.6) leads to rhodium reduction in the case of Rh(53%)@Al_2O_3 and Rh(67%)@Al_2O_3, as indicated by the appearance of the XPS peak at 307.1 eV, corresponding to metallic Rh [40-42]. The XRD data also confirm this finding (Fig. 3.7, right panel). On the other hand, the behavior of Rh(33%)@Al_2O_3 is different. Indeed, a new component is observed at 306.3 eV, in addition to the 307.1 eV peak, whose attribution is not straightforward. Notably, in all cases, the feature at 308.2 eV does not disappear after reduction. Taking into account the fact that the samples are exposed to air before XPS measurement, it is reasonable to expect a partial Rh^0 reoxidation. However, the relative Rh^{3+}/Rh^0 ratio is different in all the samples. In particular, it increases as the rhodium loading is decreased, suggesting that metal particles in the Rh(33%)@Al_2O_3 system are more easily oxidized. This behavior is indicative of the different interaction strength between the Rh particles and the support.

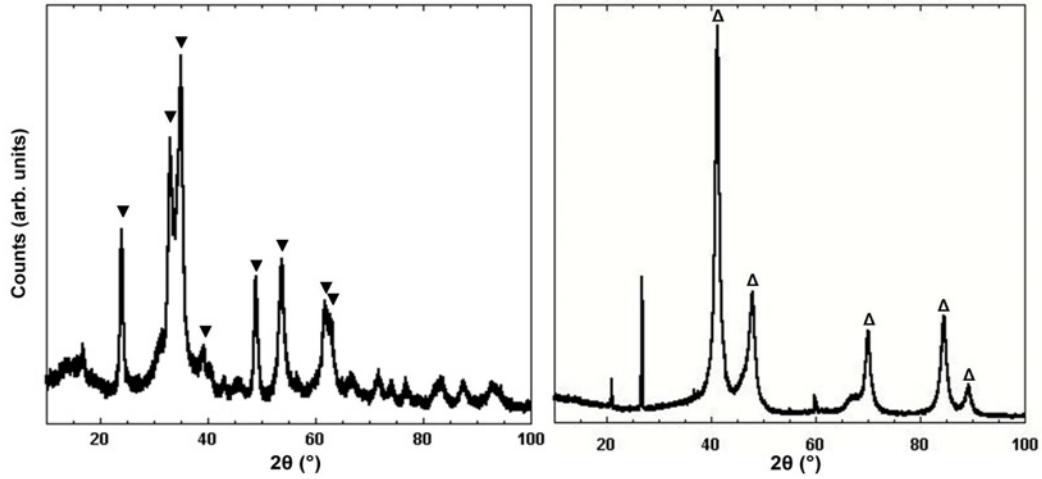

Fig. 3.7: XRD powder diffraction profiles of Rh(67%)@Al_2O_3 after calcination in air at 900 °C x 5 h (left panel) and Rh(53%)@Al_2O_3 after reduction in H_2 at 750 °C x 2 h. (▼) Rh_2O_3, (Δ) Rh.

The three model catalysts show different TPR profiles as depicted in Fig. 3.8. The Rh(33%)@Al_2O_3 catalyst presents a reduction peak centered at 185 °C with a shoulder around 135 °C. Two features, at 140 and 240 °C, are observed in the case of Rh(53%)@Al_2O_3, while a single component at 215 °C is found for Rh(67%)@Al_2O_3. Notably, no H_2 consumption is detected above 450 °C for all samples.

As discussed in the case of Rh(1%)@Al_2O_3 (§ 3.1), a clear attribution of each reduction peak is difficult. The redox properties can vary significantly with the metal loadings, due to the different extent of the interaction between the RhO_x species and the Al_2O_3 support. For instance, in Rh/Al_2O_3 samples with low loadings, the high dispersion rhodium clusters yields an intimate interaction with the alumina support, resulting in higher temperature reduction peaks. However, the metal loading also influences the particle size which may in turn affect their reduction properties . Two major explanations for the size effect have been proposed: geometric effect and electronic effect [43,44]. The geometric effect arises from the fact that the particle size influences the distribution of different oxygen adsorption sites involved in reduction process. The electronic effect is caused by the different electronic properties of small metal particles, where the band structure is not yet fully developed in comparison with bulk metal. The interplay of the above mentioned factors should be taken into account in the interpretation of the redox behavior. Although the individual contributions cannot be studied separately, we have started the investigation of the effect of the Rh-Al_2O_3 interface by statistical analysis of the TEM images. It is reasonable to expect that the metal dispersion decreases when the Rh loading increases. This can be attributed to the fact that at lower Rh content, the smaller rhodium crystallites exhibit a minor tendency to agglomerate while, at higher loading, partial sintering due to the presence of significant rhodium density occurs. Taking into account these considerations, in the

Rh(67%)@Al_2O_3 sample, the particle size should be higher with respect to both Rh(53%)@Al_2O_3 and Rh(33%)@Al_2O_3.

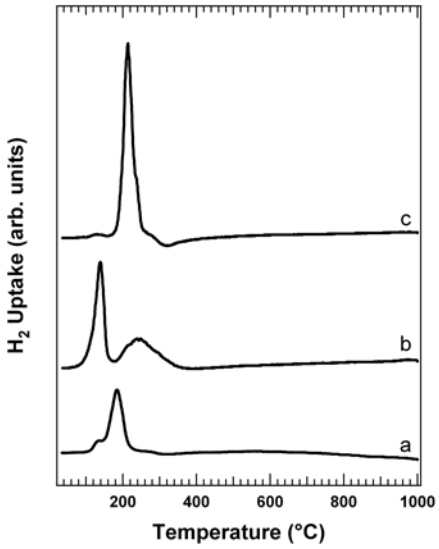

Fig. 3.8: TPR spectra of calcined (a) Rh(33%)@Al_2O_3, (b) Rh(53%)@Al_2O_3 and (c) Rh(67%)@Al_2O_3.

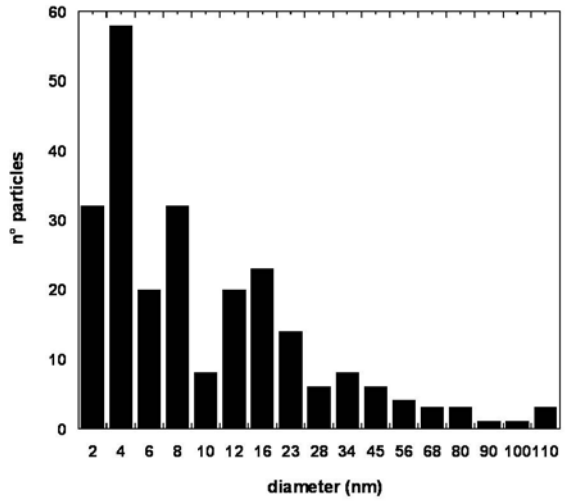

Fig. 3.9: particle size distribution of Rh(53%)@Al_2O_3 sample after reduction in H_2 at 750 °C x 2 h.

In addition to this, it can also evaluate the effect of different ionic strengths after aluminium nitrate addition to the solution containing the protected Rh nanoparticles during the synthesis: the higher the ionic strengths, the lower the stability of the protecting micelles in solution, as mentioned in § 3.2. Therefore, a more significant

destabilization effect, leading to Rh agglomeration, should be expected in the case of low metal loading. Our preliminary TEM analysis indicates that the metal loading has a remarkable effect on particle size. Ranging from a metal loading of 33 wt. % to 67 wt% a relatively narrow size distribution centered at about 10 nm and a broader size distribution shifted at larger nanoparticle diameters (40-50 nm are observed, respectively. Notably, in the case of Rh(53%)@Al_2O_3 sample, where we already obtained a size distribution by statistical analysis, a bimodal distribution (Fig. 3.9) was observed, in agreement with the two peaks observed in the TPR spectra.

The HRTEM analyses of the other reduced sample is still in progress.

The effect of aging under MPO conditions (run-up experiment with subsequent isotherm at 900 °C for 2 h) is negligible on all samples. Indeed, no significant modifications in the oxidation state of rhodium were observed (Fig. 3.6, lower panel).

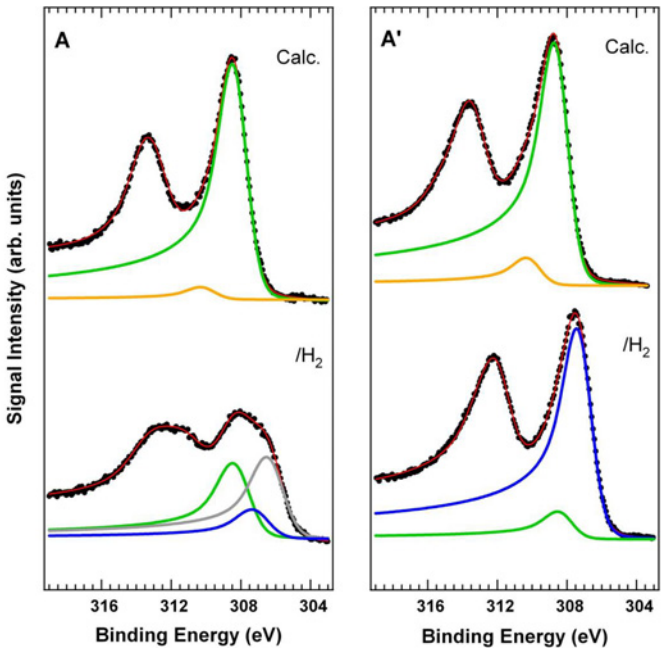

Fig. 3.10: comparison between the Rh 3*d* XPS spectra of (A) Rh(33%)@Al_2O_3 and (A') Rh(33%)/Al_2O_3, after calcination in air at 900 °C x 5 h (upper panel) and activation in H_2 at 750 °C x 2 h (lower panel).

The comparison between the Rh(33%)@Al_2O_3 catalyst and the analogous system prepared by impregnation method (Rh(33%)/Al_2O_3) is important for the interpretation of the XPS data. In fact, the XPS spectra of this latter sample does not show the low binding energy Rh feature at 306.3 eV as illustrated in Fig. 3.10. In Fig. 3.11 the TPR profiles of the two samples are compared. It is evident that the reduction of impregnated material starts immediately (below 100 °C). At 200 °C, all RhO_x species were reduced while, for the corresponding embedded system, the reduction process

was not complete yet. These results suggest the great influence of the synthesis method on the nature of the active species in the final material with respect to the particle size. Furthermore, the increase in the Rh loading could lead to a reduction of the effectiveness of the embedding strategy, due to the low amounts of alumina, which probably is not able to surround completely the metal particles. This could explain the absence of the 306.3 eV peak in the Rh(53%)@Al_2O_3 catalyst and Rh(67%)@Al_2O_3 systems.

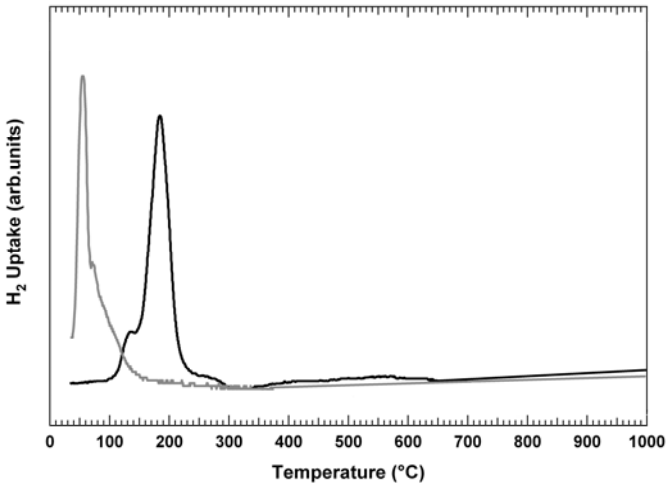

Fig. 3.11: comparison between the TPR profile of the Rh(33%)@Al_2O_3 (black line) and Rh(33%)/Al_2O_3 (grey line) samples after calcination in air at 900 °C x 5 h.

In order to clarify the origin of the peak at 306.3 eV in the XPS spectra and to stabilize a possible relation with the particular local environment in the embedded system and/or with the size distribution of the metal particles, the HRTEM characterization will yield useful information.

Finally, it is interesting to note that a value around 306.0 eV for the binding energy of Rh $3d_{5/2}$ was observed and associated to Rh^0 by Ojeda *et al.* [45] on a series of Rh(2 wt.%)/γ-Al_2O_3 catalysts, prepared by the microemulsion method, after reduction at 500 °C. In this work, the authors correlated the electronic metal-support interaction to the metal particle size.

References

[1] H. Morioka, Y. Shimizu, M. Sukenobu, K. Ito, E. Tanabe, T. Shishido, K. Takehira, Applied Catalysis A-General 215 (2001) 11.

[2] F. Basile, G. Fornasari, F. Trifiro, A. Vaccari, Catalysis Today 77 (2002) 215.

[3] F. Basile, L. Basini, G. Fornasari, M. Gazzano, F. Trifiro, A. Vaccari, Chemical Communumincation (1996) 2435.

[4] F. Basile, G. Fornasari, M. Gazzano, A. Kiennemann, A. Vaccari, Journal of Catal. 217 (2003) 245.

[5] K. Takehira, T. Shishido, P. Wang, T. Kosaka, K. Takaki, Physical Chemistry Chemical Physics 5 (2003) 3801.

[6] K. Takehira, T. Shishido, P. Wang, T. Kosaka, K. Takaki, Journal of Catalysis 221 (2004) 43.

[7] K. Takehira, T. Shishido, M. Kondo, Journal of Catalysis 207 (2002) 307.

[8] F. Basile, G. Fornasari, F. Trifiro, A. Vaccari, Catalysis Today 64 (2001) 21.

[9] F. Basile, G. Fornasari, V. Rosetti, E. Trifiro, A. Vaccari, Catalysis Today 91-92 (2004) 293.

[10] T. Shishido, P. Wang, T. Kosaka, K. Takehira, Chemistry Letters (2002) 752.

[11] P. Arpentinier, F. Basile, P. Del Gallo, G. Fornasari, D. Gary, V. Rosetti, A. Vaccari, Catalysis Today 99 (2005) 99.

[12] P. Arpentinier, F. Basile, P. Del Gallo, G. Fomasari, D. Gary, V. Rosetti, A. Vaccari, Catalysis Today 117 (2006) 462.

[13] T. Shishido, Y. Yamamoto, H. Morioka, K. Takaki, K. Takehira, Applied Catalysis A-General 263 (2004) 249.

[14] G. Budroni, A. Corma, Angewandte Chemie-International Edition 45 (2006) 3328.

[15] C.M.Y. Yeung, F. Meunier, R. Burch, D. Thompsett, S.C. Tsang, Journal of Physical Chemistry B 110 (2006) 8540.

[16] J.E. Martin, J.P. Wilcoxon, J. Odinek, P. Provencio, Journal of Physical Chemistry B 104 (2000) 9475.

[17] H. Sakurai, A. Ueda, T. Kobayashi, M. Haruta, Chemical Communication (1997) 271.

[18] M. Haruta, Catalysis Today 36 (1997) 153.

[19] N. Hickey, P. Arneodo Larochette, C. Gentilini, L. Sordelli, L. Olivi, S. Polizzi, T. Montini, P. Fornasiero, L. Pasquato, M. Graziani, Chemistry of Matererials 19 (2007) 650.

[20] M. Haruta, S. Tsubota, T. Kobayashi, H. Kageyama, M.J. Genet, B. Delmon, Journal of Catalysis 144 (1993) 175.

[21] T. Montini, A.M. Condò, N. Hickey, F.C. Lovey, L. De Rogatis, P. Fornasiero, M. Graziani, Applied Catalysis B-Environmental 73 (2007) 84.

[22] T. Montini, L. De Rogatis, V. Gombac, P. Fornasiero, M. Graziani, Applied Catalysis B-Environmental 71 (2007) 125.

[23] L. De Rogatis, T. Montini, M.F. Casula, P. Fornasiero, Journal of Alloys and Compounds 45 (2008) 516.

[24] P. Fornasiero, T. Montini, and L. De Rogatis, Chapter 2, Catalyst design for hydrogen production: embedded rhodium nanoparticles, in Diffusion and Reactivity of Solids. Book. NOVA Publisher, 2007.

[25] A. Roucoux, J. Schulz, H. Patin, Advanced Synthesis and Catalysis 345 (2003) 222.

[26] J. Schulz, A. Roucoux, H. Patin, Chemistry-A European Journal 6 (2000) 618.

[27] A. Roucoux, J. Schulz, H. Patin, Chemical Reviews 102 (2002) 3757.

[28] K.S.W. Sing, D.H. Everett, R.A.W. Haul, L. Moscou, R.A. Pierotti, J. Rouquérol, T. Siemieniewska, Pure and Applied Chemistry 57 (1985) 603.

[29] C.P. Hwang, C.T. Yeh, Q.M. Zhu, Catalysis Today 51 (1999) 93.

[30] C.B. Wang, C.T. Yeh, Journal of Molecular Catalysis A-Chemical 120 (1997) 179.

[31] J.C. Vis, H.F.J. van't Blik, T. Huizinga, J. van Grondelle, R. Prins, Journal of Catalysis 95 (1985) 333.

[32] W.Z. Weng, C.R. Luo, J.J. Huang, Y.Y. Liao, H.L. Wan, Topics in Catalysis 22 (2003) 87.

[33] D.Z. Wang, Z.L. Li, C.R. Luo, W.Z. Weng, H.L. Wan, Chemical Engineering Science 58 (2003) 887.

[34] A. Beretta, T. Bruno, G. Groppi, I. Tavazzi, P. Forzatti, Applied Catalysis B-Environmental 70 (2007) 515.

[35] S. Suhonen, M. Valden, M. Hietikko, R. Laitinen, A. Savimaki, M. Harkonen, Applied Catalysis A-General 218 (2001) 151.

[36] Z. Weng-Sieh, R. Gronsky, A.T. Bell, Journal of Catalysis 170 (1997) 62.

[37] S. Suhonen, R. Polvinen, M. Valden, K. Kallinen, M. Harkonen, Applied Surface Science 200 (2002) 48.

[38] M. Zimowska, J.B. Wagner, J. Dziedzic, J. Camra, B. Borzecka-Prokop, M. Najbar, Chemical Physics Letters 417 (2007) 137.

[39] Z. Weng-Sieh, R. Gronsky, A.T. Bell, J. Catal. 170 (1997) 62.

[40] M. Zimowska, J.B. Wagner, J. Dziedzic, J. Camra, B. Borzecka-Prokop, M. Najbar, Chemical Physics Letters 417 (2007) 137.

[41] D. Briggs and M. P. Seah, Practical Surface Analysis. Wiley, Chichester, 1990.

[42] T.L. Barr, Journal of Physical Chemistry 82 (1978) 1801.

[43] J.R. Anderson, Advances in Catalysis 23 (1973) 1.

[44] J.H. Sinfelt, Journal of Catalysis 24 (1974) 283.

[45] M. Ojeda, S. Rojas, M. Boutonnet, F.J. Perez-Alonso, F.J. Garcia-Garcia, J.L.G. Fierro, Applied Catalysis A-General 274 (2004) 33.

Chapter 4

Ni_xCu_y/Al_2O_3

4.1 Non precious metals vs. noble metals

Experimental and theoretical studies indicates that noble metals like Rh, Pd, Pt and Ru are very active in C-H and C-C bond cleavage processes [1-3], which are involved, in general, in the reforming reactions. These metals show good yields, good selectivity and good resistance towards deactivation due to coke deposition [4]. However, they are rare and very expensive. For this reason, up to now, Ni-based systems still represent the catalysts which are universal and widely used from the practical point of view, in many reactions both at laboratory and industry scales. Unfortunately, the main problem with Ni is that the rate of C-C bond formation is high, leading to the rapid growth of carbon deposits which poison the catalysts. Carbon formation can often lead to reactor plugging. To overcome this problem, and make carbon formation thermodynamically unfavorable, for example in steam reforming process, industrial plants add excess quantities of steam to the feedstock. Notably, a high steam concentration is not desirable, since additional energy is required to heat and vaporize water with, consequently, higher economic costs for the plant.

Several attempts have been made to identify carbon-tolerant catalysts. Catalysts stability can be improved by choosing a proper support and/or adding promoters to the active component. For example, it was observed that the introduction of copper to Ni-catalysts suppresses carbon formation, as well as the sintering of the active phase, in the methane steam reforming and in the hydrocarbon decomposition reactions [5-10].

Although the number of studies about Ni-Cu alloy catalysts behavior is increasing, the mechanism of nickel promotion with copper as well as the relation between catalytic activity and composition have not been fully understood.

In the present work, as explained in § 1.5, we focus on the catalytic activity and stability, as well as the influence of copper content, of Ni_xCu_y alloy catalysts for methane partial oxidation and steam reforming of methanol and ethanol.

4.2 Catalysts Characterization

Table 4.1 summarises the main textural properties of the calcined materials. All samples present Type IV isotherms with hysteresis loops, typical of mesoporous materials [11]. The t-plot analysis indicates that the microporous volume is always negligible, while the BJH analysis reveals that the materials have a pore distribution centred approximately at 56 nm. All the supported metal catalysts have a specific surface area of ~80 $m^2 g^{-1}$. The lower surface area and pore volume of the impregnated samples with respect to bare Al_2O_3 is consistent with the relatively high metal loading (10 wt.%). Ni/Cu particles might block pores of Al_2O_3 during metals deposition.

Table 4.1: results of N_2 physisorption at -196 °C after calcination in air at 600 °C for 5 h.

SAMPLE	S_{BET} [a] (m^2/g)	d_M [b] (nm)	Cumulative Pore Volume (mL/g)
Al_2O_3	97	47	0.93
Ni_{10}-Al	84	53	0.73
Ni_7Cu_3-Al	78	58	0.77
Ni_5Cu_5-Al	82	55	0.71
Ni_3Cu_7-Al	78	58	0.78
Cu_{10}-Al	80	56	0.77

[a] BET surface area
[b] Pore diameter: maximum of the pore distribution

XRD patterns of the samples after calcination and after activation in H_2 are presented in Fig. 4.1. Overlapping of the XRD peaks of the transitional aluminas complicates phase attribution, as does the low crystallinity of the support. However, the presence of γ-Al_2O_3 and θ-Al_2O_3 is evident, consistently with the medium calcination temperature [12]. Notably, α-Al_2O_3 is absent, in accordance with the relative high surface area of the samples [12].

The XRD patterns of the calcined Ni_{10}-Al and Cu_{10}-Al samples(Fig. 4.1 A, a and b), show the characteristic peaks of NiO (JCPDS 14-0481) and CuO (JCPDS 80-1268), respectively, in addition to those of the support. Average crystallite diameters of 8 nm for NiO and 26 nm for CuO were calculated by means of the Scherrer's equation applied to the main reflections of the two oxides. Other phases related to Ni and Cu were not identified.

In the XRD pattern of the calcined Ni_3Cu_7-Al sample (Fig. 4.1 A, c), it is possible to recognize a monoclinic phase and a cubic one (minor extent). The position of the diffraction peaks related to these phases indicates that they do not correspond to pure NiO (cubic structure) and CuO (monocline structure). Since the ionic radius of Ni^{2+} is bigger than that of Cu^{2+}, a partial substitution between the two cations is possible. The cubic phase will be rich in Ni^{2+}, while the monocline phase will be rich in Cu^{2+}, according to the different ability of the two ions to enter in the two crystallographic structures. The crystallites have an average diameters of 14 nm for the cubic phase and 28 nm for the monoclinic one. On the other hand, in the case of the Ni_5Cu_5-Al (Fig. 4.1 A, d) and Ni_7Cu_3-Al (Fig. 4.1 A, e) samples, the XRD patterns indicate the formation of a solid solution of $Ni_xCu_{1-x}O$ with cubic structure (as for NiO). In fact, the addition of

Cu leads to a shift towards higher angles of all the NiO diffraction peaks. An average crystallite diameter of 7 nm was obtained for both samples.

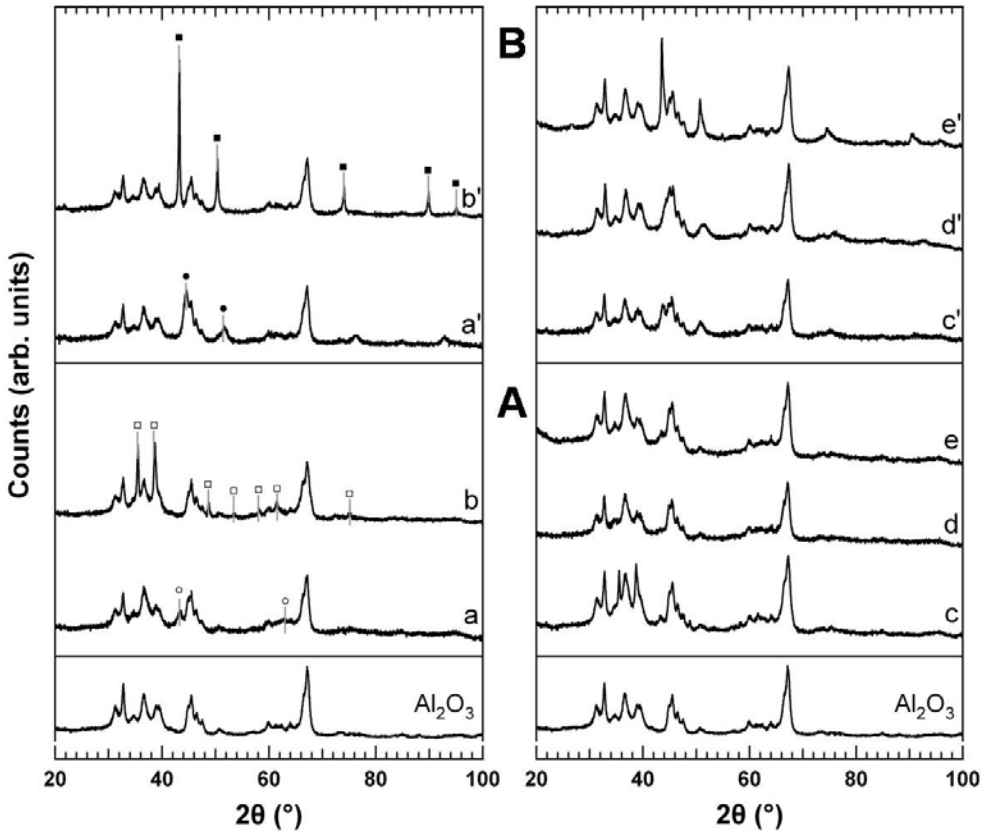

Figure 4.1: XRD powder diffraction profiles of Ni_{10}-Al (a, a'), Cu_{10}-Al (b, b'), Ni_3Cu_7-Al (c, c'), Ni_5Cu_5-Al (d, d') and Ni_7Cu_3-Al (e, e'), after calcination at 600 °C for 5 h (A) and reduction at 750 °C for 2 h (B). The XRD profile of the starting Al_2O_3 is reported for comparison. (○) NiO, (□) CuO, (●) Ni, (■)Cu.

After activation in H_2 at 750 °C, in the XRD patterns of all samples (Fig. 4.1 B) it is possible to identify only the peaks related to the metallic phases. No other Ni or Cu species were detected, although the presence of other phases (such as oxides or aluminates) with a high dispersion or below the detection limit can not be excluded.

XRD patterns of the reduced Ni_{10}-Al and Cu_{10}-Al (Fig. 4.1 B, a' and b') exhibit features due to the presence of the metallic phase with cubic structure (JCPDS 04-0850 and JCPDS 04-0836 respectively). The reflection width indicates an average crystallite diameter of 10 nm for Ni and 44 nm for Cu.

In the case of the bimetallic samples, a progressive shift of the metallic phase peaks is observed (Fig. 4.2 A). In fact, the XRD pattern shows diffraction peaks in an intermediate position between that attributable to metallic Ni and to Cu (Fig. 4.2 A), suggesting the formation of a Ni-Cu alloy. The alloy formation on Al_2O_3 after reduction

in H_2 at 750 °C was previously reported by Lee *et al.* [13]. The composition (e.g. Cu-rich or Ni-rich alloy) and the number of alloys, which can be generated, depend on the Ni:Cu ratio.

Average crystallite diameters of 9-10 nm for Ni_7Cu_3-Al and Ni_5Cu_5-Al, and of 31 nm for Ni_3Cu_7-Al were obtained.

Fig. 4.2 B presents the comparison between the measured cell parameter *a* of the metallic phases (obtained from the position of the (220) reflection), the tabulated values for Ni and Cu, and the theoretical value calculated using the Vegard's law.

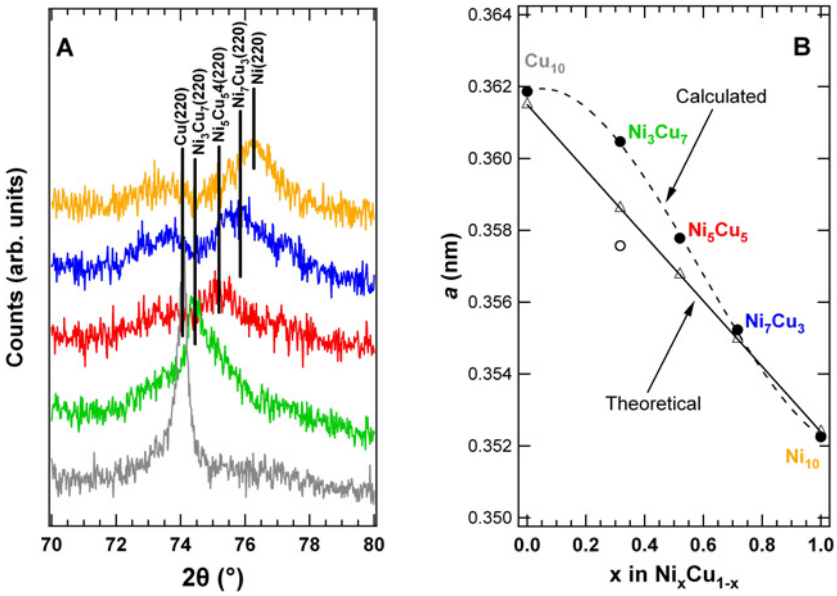

Figure 4.2: (A) Detail of the range 2θ = 70 – 80° of the XRD patterns of the reduced samples, showing the shift of the (220) reflection with the composition; (B) trend of the calculated cell parameter *a* with the composition of the metal phase, in comparison with the theoretical value.

For Cu and Ni, there is a good agreement between the two values. This is also observed in the case of the reduced Ni_7Cu_3-Al sample, where the metallic phase consists of an alloy with the desired composition. Otherwise, the cell parameter of Ni_3Cu_7 and Ni_5Cu_5 is significantly different with respect to the theoretical values. When the Ni:Cu ratio decreases (from 2.33 of Ni_7Cu_3-Al to 0.42 of Ni_3Cu_7-Al), the lattice parameter increases, and the catalyst with copper content of 7 wt.% shows the presence of two metal phases: a Cu rich alloy, which is the main component, and a Ni-rich alloy. For the Ni_5Cu_5-Al sample, only one cubic structure is detectable for the metal phase. It is not possible to identify a second metallic, which is probably beyond the detection limit of the XRD technique. The discrepancy between the observed and theoretical cell parameters suggests that also in this case two metal alloys are present. Notably, a similar trend was previously described in literature [9,14].

EXAFS and XANES spectra provide useful information regarding the properties of the investigated samples. The normalised X-ray absorption coefficient of a photoabsorber sample can be described as a linear combination of all possible different chemical species (standard). Indeed, it was possible to reconstruct the normalised spectra of the samples by means of a linear combination of the normalised XANES spectra of the standards, thus obtaining the weighted fraction of every component in both the calcined and reduced materials. It must be pointed out that the reduced samples were left exposed to air prior to the XAFS measurements for a few months. This leads to some difference between the information from the ex-situ XRD, obtained immediately after the reduction treatment, and those from XAFS. Notably, the reduced samples show catalytic activity only above 400 °C. This means that the exposure of the reduced catalyst to the reaction mixture containing oxygen at RT significantly modifies the oxidation state of the metal phase before the reaction (see below).

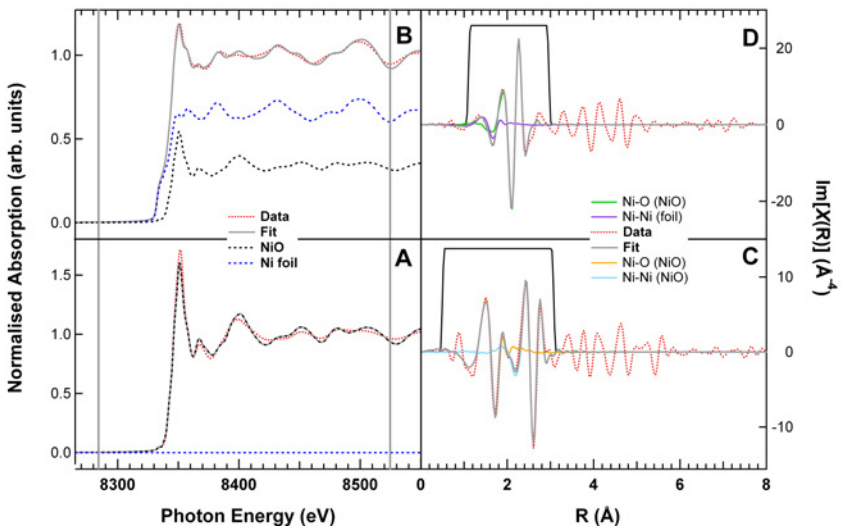

Figure 4.3: Ni K-edge for Ni_{10}-Al: experimental and fit of the XANES spectra for the calcined (A) and reduced (B) samples and experimental and fit of the imaginary part of the EXAFS signal for the calcined (C) and reduced (D) samples.

EXAFS and XANES have been performed on selected samples. Fig. 4.3 A shows XANES linear combination results of calcined Ni_{10}-Al, with metal foil and NiO as standard references, indicating that the sample is composed almost exclusively by NiO (supported on Al_2O_3). The reduced system after prolonged exposure to air (Fig. 4.3 B) appears to be composed mainly by Ni (65%) and NiO (35%). This result indicates an easy surface oxidation / passivation of the Ni nanoparticles. In agreement with XRD results, EXAFS analysis of the calcined sample reveals a very low C.N. for the first Ni-O shell, indicating a high dispersion of the oxide nanoparticles. After reduction, an

average particle size of about 1 nm was estimated for the metallic core, which is significantly lower with respect to the crystallite size obtained from XRD. This difference can be interpreted on the basis of the intrinsic characteristics / limitations of the two techniques: indeed, while the EXAFS signal is averaged over all particles, the XRD signal is more sensitive to the contribution of the bigger and more crystalline particles, with respect to the small and amorphous ones [15].

Fig. 4.4 A reports XANES linear combination results of calcined Cu_{10}-Al, showing that Cu is mainly present as CuO. EXAFS first shell analysis gives a coordination number which is typical of bulk CuO (Table 4.2). A comparison of the Fourier Transform of the outer shell with that of standard CuO, evidences only a weak decrease in module intensity. These results are consistent with the XRD outcomes and indicate the presence of bulk CuO particles, most likely with some shape anisotropy. After reduction, the Cu_{10}-Al system (Fig. 4.4 B) contains both metallic Cu (37%) and CuO (63%). The first coordination shell clearly shows the contribution of both the Cu-O shell of CuO, and of the first Cu-Cu shell of metallic Cu. The EXAFS fitting of this first coordination shell yields a very low coordination number (Table 4.2), suggesting the presence of highly dispersed small Cu-CuO core-shell nano-particles. The average metallic core dimension was estimated [15,16] to be approximately 0.6 nm. Consistently, XANES analysis indicates that the major part of Cu is oxidized.

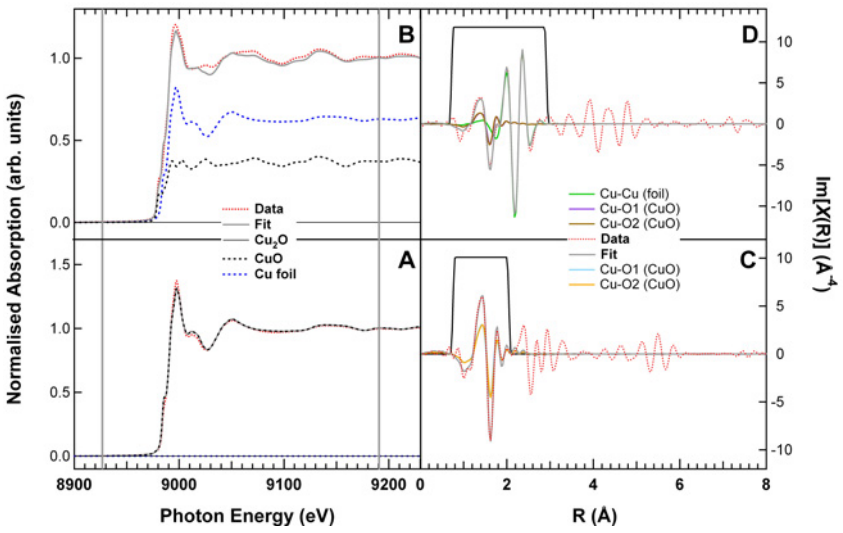

Figure 4.4: Cu K-edge for Cu_{10}-Al: experimental and fit of the XANES spectra for the calcined (A) and reduced (B) samples and experimental and fit of the imaginary part of the EXAFS signal for the calcined (C) and reduced (D) samples.

Table 4.2: structural parameters derived from the EXAFS analysis

SAMPLE	Calcined		Reduced [a]			
	M – O (nm)	C.N.	M – M (nm)	C.N.	M – O (nm)	C.N.
Ni_{10}-Al	0.208	0.5	0.248	7.1	0.203	1.8
Cu_{10}-Al	0.195	2.0	0.254	5.2	0.195	1.0
Ni_5Cu_5-Al [b]	0.195	1.7	0.252	3.0	0.296	2.2

[a] After treatment in flowing H_2 (5%) / Ar at 750 °C for 2 hours and exposure to air for a few months.
[b] Results for the analysis of the Cu edge (see text).

Fig. 4.5 reports the results of XANES linear combination fitting at the Ni and Cu edges of the calcined and reduced Ni_5Cu_5-Al sample. Notably, these XANES features could not be fitted by means of a linear combination of the XANES spectra of the standards only. The fact that the XANES features are not completely reconstructed in this way, suggests the presence of at least another phase. Consistently, XRD analysis points out the formation of a solid solution between NiO and CuO in the calcined system and of an alloy in the reduced one (although traces of a second alloy with different composition could be also present, see above). In the calcined sample (Fig. 4.5, A and C), the experimental data were fitted using a combination of the XANES spectra of NiO and CuO. The present data are not in contrast with the formation of a solid solution between the two oxides. However, the fitting limitations (see above) do not allow further indications. In the case of the reduced system (Fig. 4.5, B and D), the best linear fitting at both edges shows a mixed composition dominated by the oxidized metals (~ 70% in both cases). This fact suggests that the surface oxidation / passivation is not selective and presumably a mixed oxide is formed as a shell around a residual core of the NiCu alloy. Notably, only the Cu EXAFS signal of the bimetallic system can be analysed because of the adjacent position of Ni and Cu edges, which limits the extension of the Ni edge to only 600 eV. A low coordination number for Cu-Cu is obtained in the reduced sample, further suggesting the formation of a small metallic core, in agreement with the high concentration of oxide species revealed by XANES.

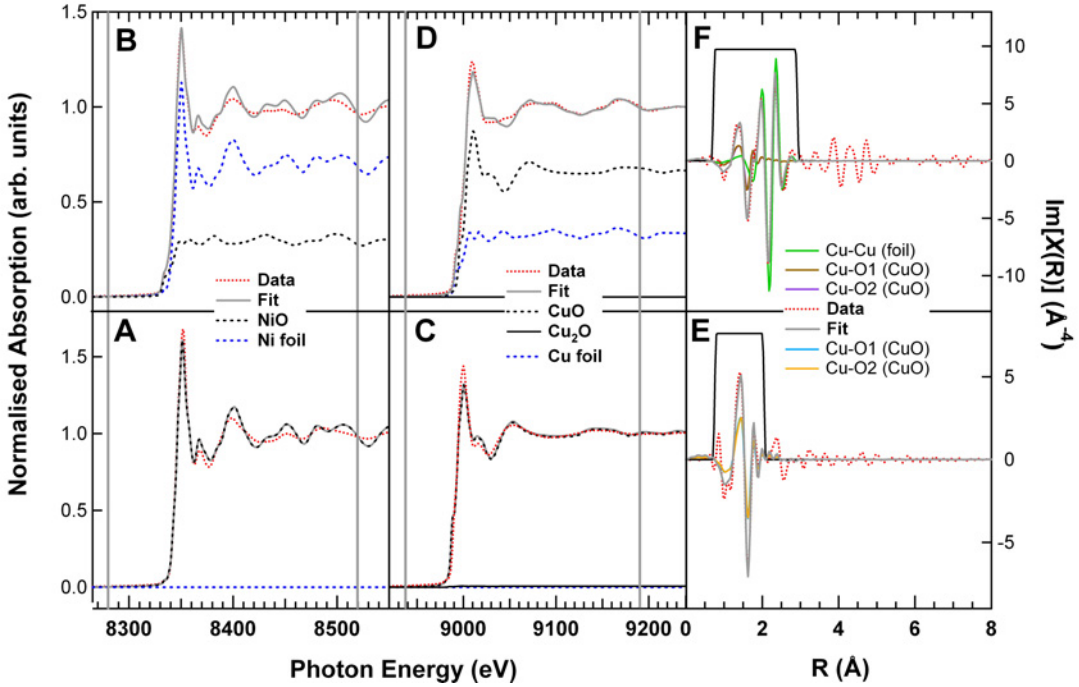

Figure 4.5: Ni/Cu K-edges for Ni_5Cu_5-Al: experimental and fit of the XANES spectra of the Ni XANES for the calcined (A) and reduced (B) samples, experimental and fit of the XANES spectra of the Cu XANES for the calcined (C) and reduced (D) samples and experimental and fit of the imaginary part of the Cu EXAFS signal for the calcined (E) and reduced (F) samples.

The TPR spectra of the investigated samples are shown in Fig. 4.6. Calcined Ni_{10}-Al displays a broad multipeak reduction profile in the temperature 400 - 800 °C range. Vice versa, unsupported bulk NiO shows a sharp reduction peak at about 380 °C (data not shown), as previously reported in literature [17,18]. This suggests the presence of a mixture of NiO_x species, originated by the different interaction of NiO particles with the Al_2O_3 support. Furthermore, the different reduction temperature could be partially ascribed to a different dimension of NiO particles. Generally, on Ni-based catalysts, the low temperature H_2 uptakes are attributed to the reduction of the NiO particles weakly interacting with the support, while the high temperature ones are assigned to the reduction of NiO species in intimate contact with the support and / or forming new species such as $NiAl_2O_4$ [19-21]. For this system, there is a strong dependence of the reduction behaviour on the thermal treatments. Indeed, the first TPR followed by mild oxidation (O_2 at 427 °C and 600 °C for 1h) leads to pronounced downward shifts of the reduction peaks, indicating significant changes in the Ni chemical environment. Notably, only the relative intensity of different components changes increasing the temperature from 427 to 600 °C. Finally, the re-oxidation at 900 °C for 5 h results in the formation of stable species (e.g. Ni-aluminate spinel species), formed by diffusion of NiO_x into the Al_2O_3. These species are difficult to reduce [22,23].

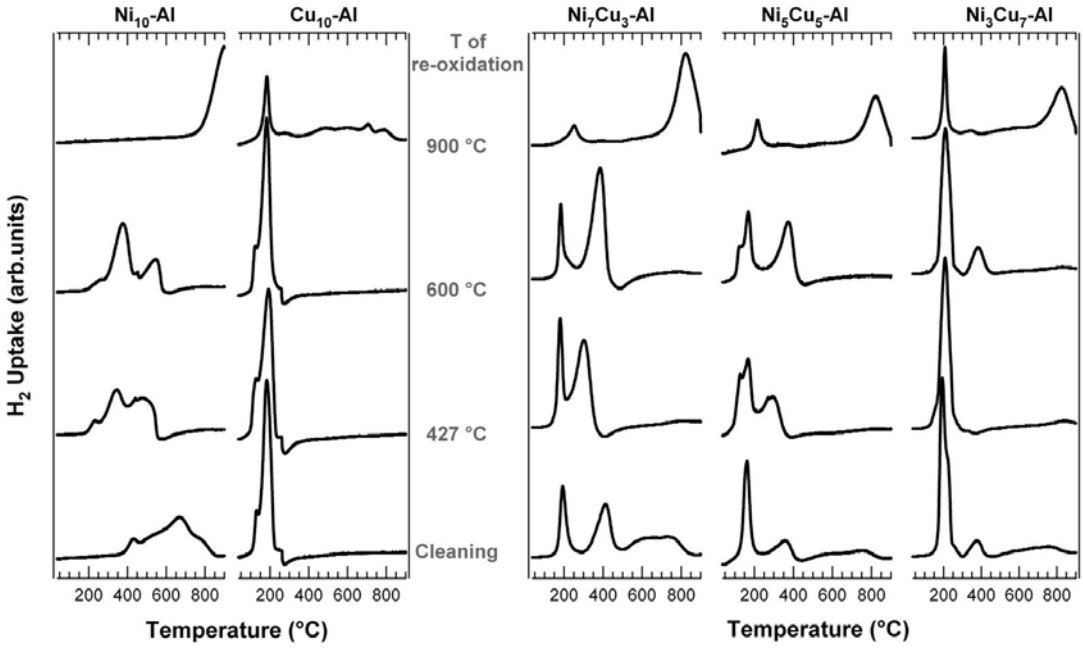

Figure 4.6: series of consecutive TPR of calcined Ni_{10}-Al, Cu_{10}-Al, Ni_7Cu_3-Al, Ni_5Cu_5-Al and Ni_3Cu_7-Al samples after standard cleaning procedure and re-oxidation at different temperatures.

Calcined Cu_{10}-Al shows two reduction peaks at 130 and 180 °C. These two components are shifted towards lower temperature with respect to pure bulk CuO, which exhibits two reduction peaks centred at 240 and 315 °C (data not reported). In the case of pure bulk Cu_2O, a single component is present at 350 °C (data not reported). The TPR profile of the calcined Cu_{10}-Al suggests the absence of Cu_2O, consistently with the XRD data. No appreciable effect of the thermal oxidative treatments on the reduction of the Cu was detected. Cu^0 species appear to interact with the support more weakly than Ni particles. New broad peaks are observed in the TPR spectra only after the re-oxidation at 900 °C, suggesting the formation of several species which can be reduced in the 400-900 °C temperature range. These new features can be attributed either to CuO_x crystallites with different dimensions, or to the CuO_x species which interact differently with the support: the stronger the interaction, the higher the reduction temperature.

The comparison of the TPR profile of Ni_xCu_y-Al samples with that of Ni_{10}Al clearly indicates that the addition of Cu strongly promotes Ni reduction. This effect is more evident when increasing the copper content. Notably, even a physical mixture of bulk NiO and CuO shows a significant promotion of the NiO reduction (data not reported). Consistently, the supported bimetallic systems present a sharp reduction peak below 200 °C (160 °C for Ni_5Cu_5-Al and 190 °C for Ni_3Cu_7-Al and Ni_7Cu_3-Al), which can be associated with the reduction of Cu in well dispersed mixed oxide species.

Furthermore, a broad peak at intermediate temperature (410 °C for Ni_7Cu_3-Al, 355 °C for Ni_5Cu_5-Al and 375 °C Ni_3Cu_7-Al) is observed. This latter process can be associated with the reduction of Ni-based species promoted by the presence of metallic Cu [13]. Thus, the very strong interaction found between the Ni and Al_2O_3 with respect to the interaction of Cu-Al_2O_3, does not seem to limit the strong catalytic effect of Cu on the Ni species. However, a minor reduction contribution, for all bimetallic systems, is observed at high temperature (above 450 °C), which could be either related to the presence of traces of Ni oxides species strongly interacting with the Al_2O_3 or to some kind of buoyancy effect.

A clear attribution of the reduction peaks is complicated by the presence of more than one $Ni_xCu_{1-x}O$ phase on the Cu-rich samples (see XRD). The subsequent oxidative treatment at 427 °C does not influence the peaks related to the reduction of Cu, while the features at 350-400 °C temperatures are shifted towards lower temperatures ($\Delta T \sim$ 115 °C for Ni_7Cu_3-Al and $\Delta T \sim$ 60 °C for Ni_5Cu_5-Al). Noteworthy, in the case of the Ni_3Cu_7-Al sample, no signals are detected between 300 and 400 °C. A similar behaviour is observed after oxidation at 600 °C. Finally, under strong oxidation conditions (at 900 °C) a reduction peak at 820 °C grows in the TPR spectra, which can be attributed to NiO and/or CuO and/or $Ni_xCu_{1-x}O$ species strongly interacting with the support, such as Ni aluminates.

4.3 Catalytic activity

4.3.1 Methane Partial Oxidation

The contribution of Al_2O_3 to MPO is marginal under our experimental conditions. Indeed, on bare Al_2O_3 (data not reported) the conversion of CH_4 and O_2 starts only above 650 °C, yielding maximum CH_4 and O_2 conversion of about 30 and 85%, respectively (at 900 °C).

Fig. 4.7 depicts the activity profile of calcined (A) and reduced (B) Ni_{10}-Al under MPO conditions.

In the case of Ni_{10}-Al, after activation in H_2 at 750 °C, O_2 is consumed between 200 and 300 °C while this does not occur for CH_4. No products are detected in this temperature range, indicating the oxidation of reduced Ni particles to NiO_x species as previously reported [24]. At about 340 °C, CH_4 and O_2 start to be simultaneously converted. Up to 620 °C, temperature at which O_2 conversion reaches 100% and CH_4 conversion is approximately 25%, CO_2 and H_2O are the only products observed. This is consistent with the occurrence of total combustion of CH_4. At the "critical temperature" of 710 °C, a transient process takes place: a steep increase in CH_4 conversion is detected. This is accompanied by the formation of additional CO_2 and H_2O, and, simultaneously, H_2 and CO production sharply increases. Above 710 °C, H_2

and CO yields rapidly increase until they reach their maximum theoretical value, while CO_2 and H_2O yields decrease to zero. The transient phenomenon described above is also detected in the case of calcined Ni_{10}-Al. However, consistently with the fact that Ni is already oxidised, the low temperature O_2 consumption is not observed and the reactivity is shifted to higher temperatures (~ 100 °C). The conversion of both CH_4 and O_2 starts only above 450 °C, increasing with temperature up to 775 °C when they become complete. No modification of the catalytic activity was observed during the second run-up experiment up to 900 °C on both systems.

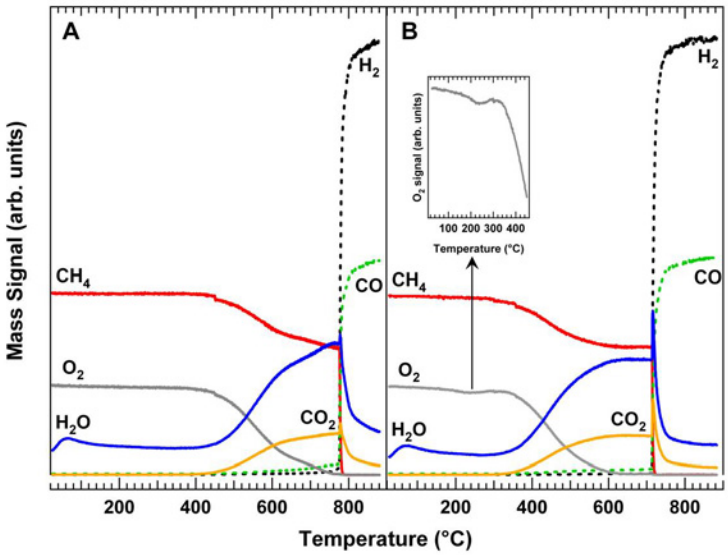

Figure 4.7: Methane Partial Oxidation over calcined (A) and reduced (B) Ni_{10}-Al. Conditions: CH_4 (2.0%) + O_2 (1.0%) in Ar, GHSV = 50000 mL g^{-1} h^{-1}.

Calcined and reduced Cu_{10}-Al show very poor MPO activity as depicted in Fig. 4.8. The CH_4 and O_2 conversion begins around 350 °C, being CO_2 and H_2O the only detected products up to 700 °C. Above this temperature, H_2 and CO formation is also observed. Full conversion of CH_4 is never achieved (~60% at 900 °C), while O_2 conversion reaches 100 % at 600 °C. During the second run-up experiment, H_2 and CO yields decrease significantly suggesting catalyst deactivation. The observed deactivation could be reasonably related to metal sintering, since Cu has a low coking tendency [13,25].

The catalytic performance of Ni_5Cu_5-Al catalyst (Fig. 4.9) is very promising. On the reduced sample, O_2 consumption is observed at considerably lower temperature (~ 45 °C) with respect to the Ni-only system. This consumption continues up to about 270 °C and can be related to the partial oxidation of NiCu alloy particles. The concomitant conversion of CH_4 and O_2 starts above 320 °C. Until 540 °C, only CO_2 and H_2O are detected. At this temperature, complete conversion is achieved for O_2 and, simultaneously, H_2 and CO production sharply increase. It is interesting to note that, in

the case of Ni_{10}-Al, the O_2 conversion reaches 100% below the "critical temperature", while this does not occur for the bimetallic system. At 540 °C, CH_4 conversion rapidly increases, reaching 75% and 100% only above 750 °C. Over non-reduced Ni_5Cu_5-Al, the sharp syngas production kick-off is shifted by 50 °C (~ 590 °C) towards higher temperature.

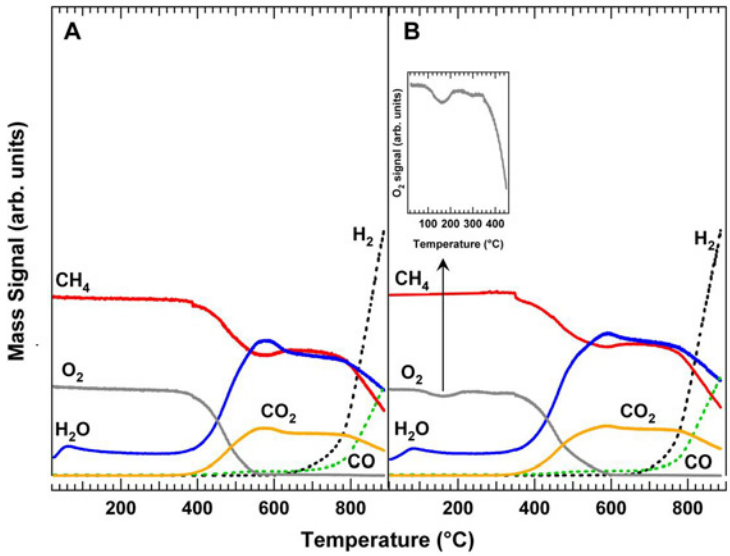

Figure 4.8: Methane Partial Oxidation over calcined (A) and reduced (B) Cu_{10}-Al. Conditions: CH_4 (2.0%) + O_2 (1.0%) in Ar, GHSV = 50000 mL g^{-1} h^{-1}.

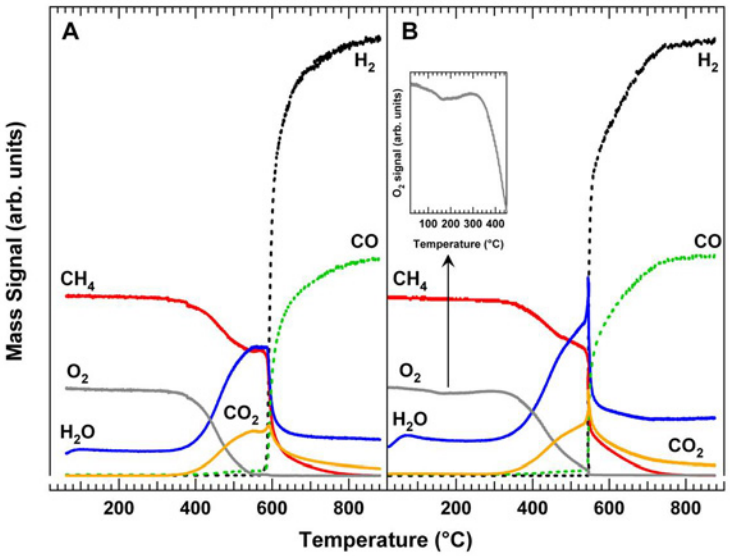

Figure 4.9: Methane Partial Oxidation over calcined (A) and reduced (B) Ni_5Cu_5-Al. Conditions: CH_4 (2.0%) + O_2 (1.0%) in Ar, GHSV = 50000 mL g^{-1} h^{-1}.

The catalytic behaviour of Ni_3Cu_7-Al and Ni_7Cu_3-Al samples is analogous of that of Ni_5Cu_5-Al (data not reported). No significant differences in terms of both product distribution and the position of the "critical temperature" were observed.

Appreciable modifications of the catalytic activity were not observed during the second run-up experiment up to 900 °C for all bimetallic systems, indicating good thermal stability.

Selected steady state experiments were conducted on Ni_{10}-Al and Ni_5Cu_5-Al under reaction conditions at 900 °C for 65 h to further investigate the stability of these materials (Fig. 4.10). The Cu_{10}-Al was not investigated due to its poor activity. No appreciable deactivation was observed for both systems, mainly because of the diluted reaction conditions, which reduce the extent of carbonaceous deposits. However, performing a subsequent temperature programmed oxidation (TPO) of the aged samples, CO_2 evolution was observed only for Ni_{10}-Al, indicating the presence of carbonaceous deposits on the catalyst surface. This is consistent with the well known ability of Ni to promote coke formation, even in the form of long filaments [26].

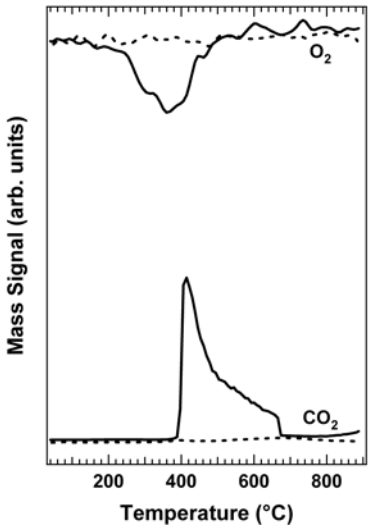

Figure 4.10: Temperature Programmed Oxidation (TPO) experiments on samples aged under MPO conditions (as reported for run-up experiments) at 900 °C for 65 h: (bold line) Ni_{10}-Al and (dotted line) Ni_5Cu_5-Al.

Partial oxidation of methane over Ni/Al_2O_3 was extensively studied in literature [24,27-37]. Using the pulse method, temperature programmed surface reaction (TPSR) and X-ray diffraction techniques on Ni(8%)/α-Al_2O_3, it was evinced by Jin *et al.* that the reaction follows a mechanism in which Ni^0 is firstly oxidized to NiO [24]. Subsequently, on NiO, the complete combustion of CH_4 takes place. At a certain critical temperature, besides the complete oxidation of methane, the reduction of NiO into Ni^0 by CH_4 occurs, leading to the formation of additional CO_2 and H_2O, as expressed by the following equation:

$$NiO + CH_4 \rightarrow CO_2 + H_2O + Ni^0 \qquad (4.1).$$

This nickel valence change represents the driving force which transforms the reaction from the complete oxidation to the partial oxidation of methane. Ni^0 species constitute the active sites for the MPO. The same reaction scheme was proposed by Yan *et al.* [37] on Ni(10 wt.%)/Al_2O_3.

Our experimental data for Ni_{10}-Al catalyst are in agreement with this scenario. XRD and XANES revealed that the calcined Ni_{10}-Al contains essentially NiO well dispersed on the surface. On the other hand, the reduced sample contains Ni^0 nanoparticles, which react with O_2 during MPO experiments up to 350 °C, producing a system similar to that observed by XANES (reduced sample exposed to air for a few months). The complete combustion of CH_4 takes place on NiO as previously reported [24,32], while the reforming of CH_4 is promoted by Ni reduced *in situ* at high temperature. In the case of the reduced Ni_{10}-Al, the catalyst is active at lower temperature because of the presence of residual reduced Ni, which could activate CH_4 for the combustion.

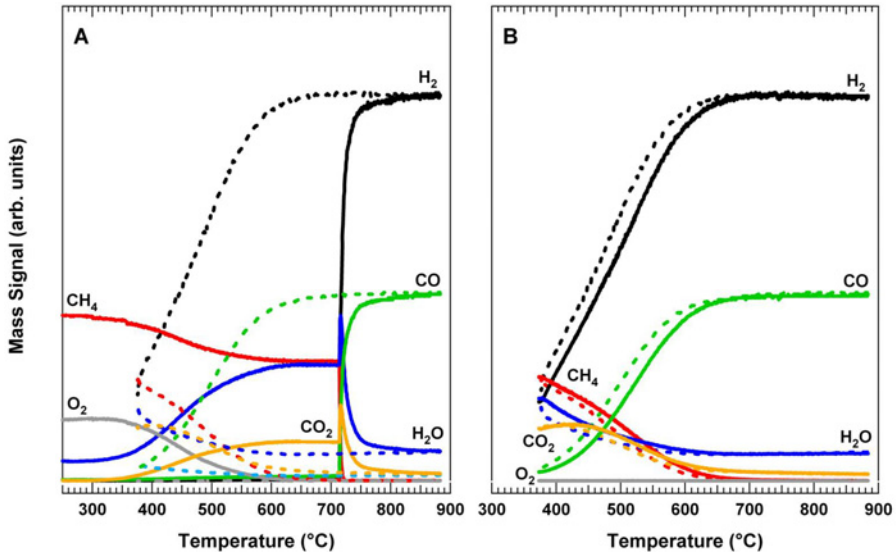

Figure 4.11: Methane Partial Oxidation over reduced Ni_{10}-Al: (A) (solid line) run-up experiment followed by (dotted line) cooling at 380 °C under reactant mixture; (B) (bold) subsequent run-up experiment. Conditions: CH_4 (2.0%) + O_2 (1.0%) in Ar, GHSV = 50000 mL g^{-1} h^{-1}.

In order to corroborate the reaction mechanism described above, we performed the following experiment on the reduced Ni_{10}-Al sample (Fig. 4.11 A and B). After the run-up experiment (solid line in Fig. 4.11 A analogous to Fig. 4.7 B), the catalyst was cooled down to 380 °C under the reactant mixture (dotted line in Fig. 4.11 A and B). Then, a second run-up experiment was carried out (solid line in Fig. 4.11 B). It is evident that the reaction mechanism is different. Indeed, during the second run-up, the 710 °C

"critical temperature", which characterizes the first run-up, is not observed. It is reasonable to attribute this result to the absence of NiO species on the catalyst surface. The trend of the H_2O and CO_2 signals could suggest a CRR mechanism (see § 1.3.2). In the 380-450 °C temperature range, water is consumed via the steam reforming reaction, while the CO_2 signal remains almost constant. Only above 450 °C, the CO_2 signal starts to decrease due to the dry reforming process which becomes operative.

Furthermore, if the reduced Ni_{10}-Al sample is exposed to the reactant mixture at 660 °C, 50 °C below the "critical temperature", the complete conversion of CH_4 and O_2 is instantaneously achieved as shown in Fig. 4.12. This fact can be again attributed to the presence of Ni^0 species on the catalyst surface.

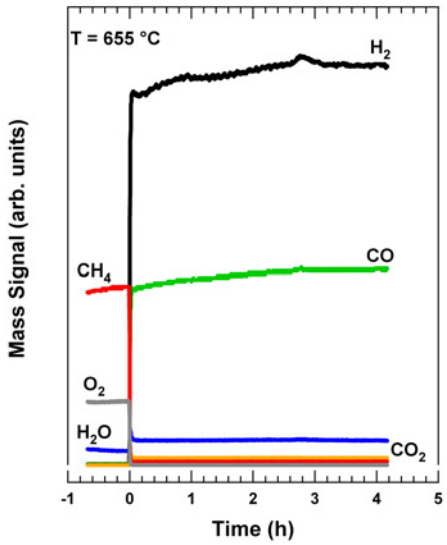

Figure 4.12: Methane Partial Oxidation over reduced Ni_{10}-Al. At t = 0 the sample is exposed to reactant mixture. Conditions: CH_4 (2.0%) + O_2 (1.0%) in Ar, GHSV = 50000 mL g^{-1} h^{-1}, T = 655 °C.

Several parameters have to be taken into account to fully interpret the origin of the catalytic performance observed over the bimetallic system. Generally, the different catalytic behaviour of NiCu-based systems has been discussed in terms of two mechanisms: an electronic effect and a geometric effect [38-42]. The former is related to the differences of electronic properties of Ni-Cu alloys in comparison with individual metals. Instead, the latter effect is related to the fact that reactions such as CH_4 activation are structure-sensitive and there is a dependence on the catalyst particle size. Particles with different shapes or size expose different surface planes to the reactant and each of them can show a peculiar catalytic activity due to different active sites involved. These aspects require further investigation.

The run-up experiments on NiCu-based catalyst suggest that the reaction pathway is similar to that observed for Ni_{10}-Al implying, also in this case, a change in the oxidation

state of the metals. Noteworthy, the maximum H_2/CO ratio of about 2 is achieved at ~750 °C, while, on Ni_{10}-Al, temperatures higher than 850 °C are required. The major advantage of Cu addition into the formulation of the catalyst is the strongly reduced deposition of coke. It was previously reported that coke deposition is strongly enhanced, if the size of Ni particles is greater than a critical value [43]. This fact indicates that coke deposition requires a sufficient number of adjacent sites for carbon growth. Moreover, Chin *et al.* [44] reported that the addition of Au to Ni-based catalyst for hydrocarbon steam reforming prevents the catalyst deactivation, presumably by sticking of Au at steps and edges of the Ni surfaces, i.e. the same nucleation sites for coke deposition. Similar could be the situation in our NiCu-based systems, suggesting that the effect of Cu could be geometric. The formation of a Ni-Cu alloy would be responsible of the blocking or decrease of the sites involved in the carbon growth, as previously discussed by Reshetenko *et al.* for high temperature methane decomposition [14]. Therefore, Cu in the Ni/Al_2O_3 system should act as a stabilizing agent due its structure-forming properties. However, the modification of the electronic properties of a Ni-Cu alloy in comparison with monometallic Ni, cannot be ruled out, in order to justify the position of the "critical temperature". In the bimetallic systems, this peculiar temperature is shifted towards lower temperatures ($\Delta T \sim 170$ °C). The different electronic environment of Ni in the alloy could influence the interaction between the adsorbed reaction intermediates and the metal phase. Furthermore, another factor which has to be taken into account, is the influence of the reaction medium, since the nature of gas reactants that stick on the alloy surface can significantly affect the surface composition due to segregation and restructuring effects. Indeed, if the reactants interact strongly enough with one of the selective alloy components, surface segregation may occur, together with alterations of the surface alloy stoichiometric composition [9,45].

It is worth to point out that copper addition leads often to more stable catalyst, as in the present work, but it does not always lead to more active catalysts as observed, for instance, in the case of CO hydrogenation [46]. For this reason, the global effect of catalyst promotion has to be evaluated by both catalyst activity and catalyst stability. Bimetallic systems, described above, show both higher catalytic activity and stability with respect to the monometallic samples.

Fig. 4.12 (upper panel) reports TPD spectra of CH_4 over calcined (A) and reduced (B) Ni_{10}-Al catalyst. The lower panel shows the TPO spectra recorded after the corresponding TPD experiment (A' and B', respectively). In the case of the calcined sample (Fig. 4.12 A), the CH_4 signal remains constant up to 600 °C. At this temperature methane starts to be converted instantaneously. This is accompanied by the formation of CO, CO_2, H_2O and H_2. Above 600 °C, carbon oxides and water are consumed while the H_2 signal continues to grow. At 730 °C, H_2 production rapidly decreases. In the same temperature range, the CH_4 signal increases up to 640 °C and then decreases.

Around 730 °C a minimum is achieved. Finally, increasing the temperature, the methane conversion quickly diminishes. This trend is due to the accumulation of surface C species over the catalyst with consequent blocking of the active sites for the methane activation and loss of catalytic activity.

The generation of CO, together with small amounts of CO_2 and H_2O, suggests the participation of an active oxygen species present on the metal surface (e.g. oxygen of NiO_x). Therefore, when the calcined sample is exposed to CH_4, the interaction with NiO_x follows a two step mechanism: first, CH_4 is oxidized to CO, CO_2 and H_2O, resulting in the reduction of NiO_x to Ni^0, and then CH_4 begins to dissociate over Ni^0 sites to generate H_2. This reaction scheme was suggested by Jin *et al.* [24] on Ni(8 wt.%)/α-Al_2O_3.

On the other hand, the reduced sample is more active (Fig. 4.12 B). Only H_2 is detected as product above 200 °C. The CH_4 decomposition starts around 220 °C and increases until 570 °C. Above this temperature, a progressive decline in CH_4 conversion is observed.

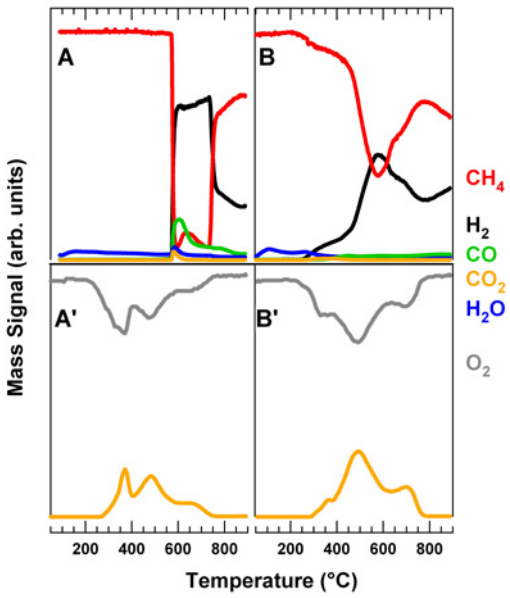

Figure 4.12: TPD-CH_4 over calcined (A) and reduced (B) Ni_{10}-Al followed by TPO experiment (A' and B' respectively). Conditions: CH_4 (2.0%) in Ar, GHSV = 50000 mL g^{-1} h^{-1}, 10 °C/min.

TPO spectra (Fig. 4.12 A' and B') show in both cases three major peaks, which are related to different carbonaceous species. It is difficult to establish the exact nature of these species, but it is reasonable to associate the peaks at higher temperatures with oxidation of graphitic carbon organised in bigger aggregated. The lower temperature TPO peaks could be due to the oxidation of small carbonaceous deposits, probably located in the proximity of accessible metal nanoparticle (able to activate O_2 molecules)

or due to the oxidation of C_xH_y species. Notably, Yan *et al.* [37] performed temperature programmed hydrogenation experiments in order to investigate the nature of carbon deposits on Ni(10 wt.%)/Al_2O_3 catalyst after CH_4/O_2 reaction at 700 °C for 2 h. The two peaks observed in the spectra (between 200-310 °C and 600-800 °C), were assigned by the authors to carbon species with partially dehydrogenated CH_x ($1 < x < 3$) species and to inactive carbidic clusters, respectively.

The mechanism for methane activation over Cu_{10}-Al system is quite different, as shown in Fig. 4.13. On the calcined sample, methane is converted to CO_2 and H_2O between 340 and 640 °C, most likely via the combustion mechanism. In fact, in this temperature range H_2 production is not observed. H_2 is detected only above 640 °C. On the reduced Cu_{10}-Al catalyst, methane starts to decompose in H_2 and C at higher temperatures (T > 430 °C).

On bimetallic systems, the reaction scheme is similar to that discussed for Ni_{10}-Al. Fig. 4.14 depicts the results for Ni_5Cu_5-Al.

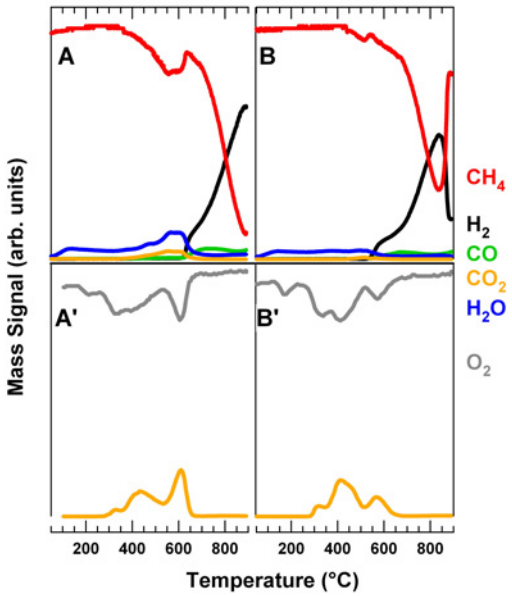

Figure 4.13: TPD-CH_4 over calcined (A) and reduced (B) Cu_{10}-Al followed by TPO experiment (A' and B' respectively). Conditions: CH_4 (2.0%) in Ar, GHSV = 50000 mL g^{-1} h^{-1}, 10 °C/min.

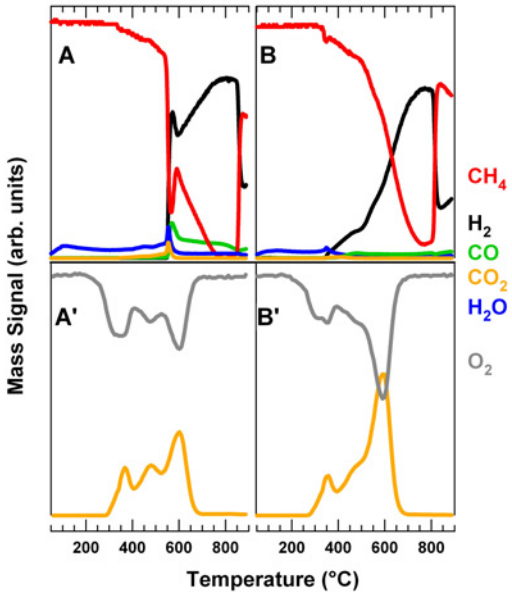

Figure 4.14: TPD-CH_4 over calcined (A) and reduced (B) Ni_5Cu_5-Al followed by TPO experiment (A' and B' respectively). Conditions: CH_4 (2.0%) in Ar, GHSV = 50000 mL g^{-1} h^{-1}, 10 °C/min.

4.3.2 Methanol Steam Reforming

Fig. 4.15 shows the results of the steam reforming of methanol over pre-reduced Ni_xCu_y/Al_2O_3.

On bare Al_2O_3, methanol conversion starts around 230 °C, producing essentially dimethylether (CH_3OCH_3) up to 400 °C. The formation of this product is related to the acidic characteristics of the support. Above 400 °C, H_2, CO and CO_2 are observed. CO_2 is also detected at 700 °C in minor concentrations.

Over the Ni_{10}-Al sample, methanol begins to be converted above 150 °C (Fig. 4.15, a). Below 250 °C, the main products are CO and H_2, which derive from methanol decomposition. The formation of CO_2 is observed for temperatures higher than 230 °C, indicating that the WGS reaction becomes operative only above this temperature. Significant amounts of CH_4 are also detected in the 230-510 °C temperature range, as a product of CO and CO_2 hydrogenation. This parallel reaction decreases the H_2 yield. The maximum for H_2 yield is reached above 510 °C, where the evolution of CH_4 is inhibited.

The behaviour of the Cu_{10}-Al catalyst (Fig. 4.15, b) is different. In this case, the WGS is already operative at low temperature (T < 230 °C), consistently with the well know ability of Cu to promote the WGS activity. The formation of small quantities of CO is observed only above 350 °C. It has to be noted that, increasing the temperature, the WGS equilibrium shifts towards the reactants. Therefore, the conversion of CO to

CO_2 due to the WGS reaction, slightly decreases above 450 °C. The catalytic performance observed in this work is in agreement with data reported by Lin *et al.* on Cu(15 wt.%)/Al_2O_3 [47].

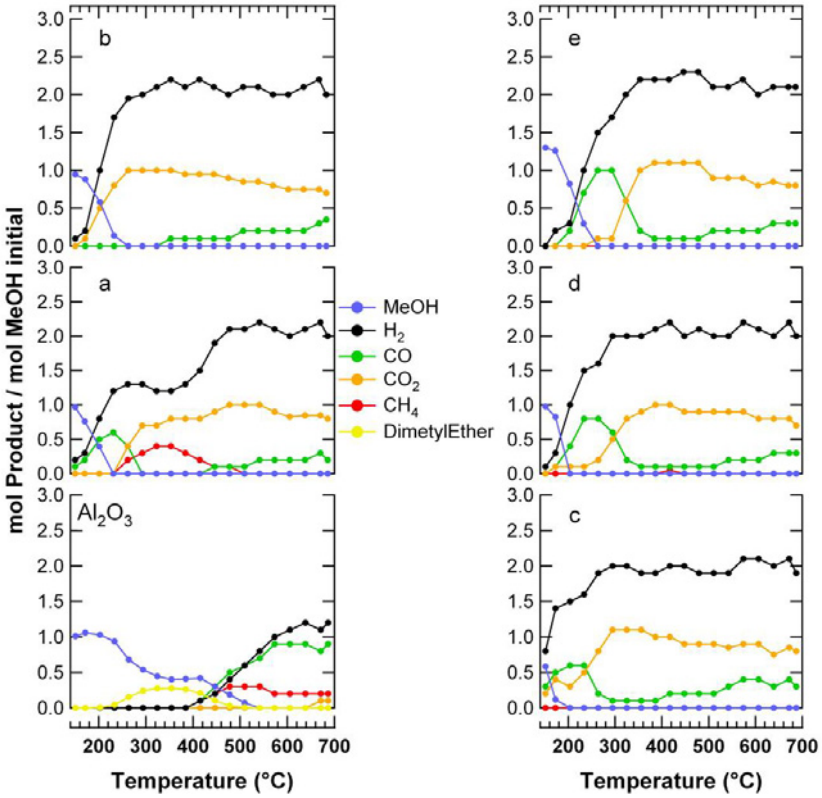

Figure 4.15: Methanol Steam Reforming over bare Al_2O_3 and pre-reduced at 750 °C for 2 h (a) Ni_{10}-Al, (b) Cu_{10}-Al, (c) Ni_3Cu_7-Al, (d) Ni_5Cu_5-Al, (e) Ni_7Cu_3-Al. Conditions: MeOH (1.0%) + H_2O (4.0%) in Ar, GHSV = 16000 mL g^{-1} h^{-1}.

Copper-containing catalysts are well known to show particularly high activity and selectivity for the MeOH-SR. They are active at lower temperatures and, for this reason, they are preferred with respect to other catalysts, like the Ni-based, which possesses high activity in carbon oxides hydrogenation with, consequently, the promotion of undesirable by-products formation (e.g. CH_4). This makes the use of such metals an unattractive option for processes where hydrogen is desired. Experimental studies on MeOH-SR performed over Ni/Al_2O_3 systems were not found, confirming the considerations stated above.

The catalytic performances of the bimetallic systems are interesting (Fig. 4.15, c, d and e). The conversion of methanol starts above 150 °C on Ni_7Cu_3-Al and Ni_5Cu_5-Al, while it begins already at this temperature over Ni_3Cu_7-Al. The complete conversion is reached around 260 °C for Ni_7Cu_3-Al and around 205 °C for Ni_3Cu_7-Al and Ni_5Cu_5-Al.

The composition of the bimetallic systems does not seem to influence the product distribution above 300 °C. On the other hand, at temperatures below 300 °C, some differences are evident. Indeed, when the Ni:Cu ratio increases, the CO yield increases while the CO_2 yield follows an opposite trend. By comparing these activity profiles with those of the monometallic systems, it is clear that the relative amounts of carbon oxides are related with the copper relative concentration in the catalysts, which influences the WGS equilibrium. Notably, CH_4 production was not observed during the run-up experiment on the samples, suggesting that it is possible to decrease significantly the CO/CO_2 hydrogenation activity of nickel catalysts by copper alloying. It is well established, and reported in several reviews, that Cu does not easily dissociate CO [48-50]. It is reasonable to infer that this low reactivity towards CO dissociation yields the inhibition of CO activation on the nickel–copper alloy due to dilution of the active nickel phase by the inactive copper atoms. The influence of copper on carbon deposits cannot be also excluded as observed in methane partial oxidation.

No significant deactivation of the catalyst activity for all samples was observed in the two consecutive run-up experiments.

4.3.3 Ethanol Steam Reforming

Fig. 4.16 presents typical activity profiles for Ni/Cu-based catalysts under ethanol steam reforming reaction. With respect to methanol, ethanol requires higher reforming temperatures due to the presence of the C-C bond.

On bare Al_2O_3, ethanol conversion starts above 250 °C, producing essentially ethylene through the dehydration reaction. Only above 600 °C, some reforming products are detected, obtained mainly from the cracking of the carbonaceous compounds.

On the Ni_{10}-Al catalyst (Fig. 4.15, a) ethanol begins to be converted at 200 °C. Below this temperature, acetaldehyde and H_2 are the main products. Increasing the temperature, the acetaldehyde yield decreases while CO and CH_4 start to be produced. The CO yield reaches a maximum around 250 °C, after which it drops to zero at 350 °C. Above this temperature, the WGS reaction becomes operative as confirmed by the presence of CO_2 among the products. The formation of CH_4 is strongly favored between 250 and 450 °C, while the evolution of ethylene is appreciably inhibited. For higher temperatures, the product distribution is dictated by the equilibrium of the water gas shift and the methanation reactions. The reforming reactions are predominant only above 500 °C, where only H_2, CO and CO_2 are detected as products. No modification of the catalytic activity was observed after 3 run-up experiments.

It is interesting to note that the dehydration of ethanol to ethylene is well known to be strongly active on Al_2O_3, due to the acidic characteristics of this support. In the case of the Ni_{10}-Al sample, the inhibition in the ethylene production can be related to the

partial coverage of the alumina surface by the metal, with consequent reduction of the acidic sites. Furthermore, the activity of nickel in the reforming of ethylene cannot be excluded from these considerations.

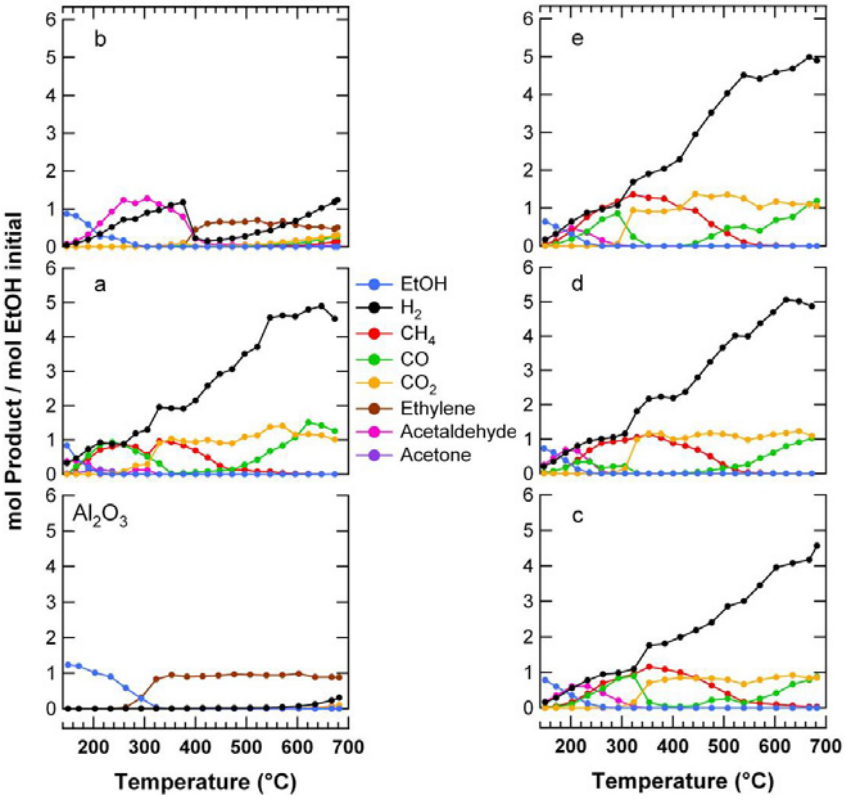

Figure 4.16: Ethanol Steam Reforming over bare Al_2O_3 and reduced (a) Ni_{10}-Al, (b) Cu_{10}-Al, (c) Ni_3Cu_7-Al, (d) Ni_5Cu_5-Al, (e) Ni_7Cu_3-Al. Conditions: EtOH (1.0%) + H_2O (5.0%) in Ar, GHSV = 16000 mL g^{-1} h^{-1}.

EtOH-SR was studied over Ni/Al_2O_3 system by several research groups [51-59]. Comas *et al.* [60] studied the reaction in the 300-500 °C temperature range, and they did not find any evidence for the water gas shift reaction over Ni. This differs from our experimental results. Akande *et al.* [61] investigated the effects of catalyst synthesis method, Ni loading, and temperature on the catalytic activity of Ni/Al_2O_3 catalysts for ethanol reforming. Three types of preparation methods, namely, coprecipitation, precipitation and impregnation, were evaluated. Optimal Ni loading of 15 % was found for maximum ethanol conversion using Ni/Al_2O_3 catalysts prepared by coprecipitation and precipitation methods. For comparison, the Ni loading did not show noticeable effects on the activity when impregnation method was used. Regarding hydrogen production, the catalyst prepared by coprecipitation with 15 % Ni loading showed the best performance. In addition, Ni/Al_2O_3 prepared by coprecipitation showed the highest selectivity to hydrogen. These results emphasize the importance of the synthesis

method, which affects the nature of the active species generated on the catalyst surface. These different species show different redox properties, thus different reactivity under the same reaction conditions.

The catalytic performance of the Cu_{10}-Al catalyst is strongly different (Fig. 4.15, b). Ethanol conversion becomes significant above 200 °C. Up to 375 °C, the main products are acetaldehyde and hydrogen. Above this temperature, ethylene is observed, while acetaldehyde is not detected. The H_2 yield, which reaches a minimum around 450 °C, grows again by increasing the temperature. Traces of CO, CO_2 and CH_4 are also observed at high temperatures (T > 600 °C). Significant changes are observed in the two subsequent run-up experiments. The catalyst is characterized by a progressive worsening of its catalytic performance. The complete conversion is reached only at high temperatures (T > 600 °C), producing essentially ethylene and H_2. Furthermore, the formation of acetaldehyde is strongly inhibited, suggesting that the observed deactivation is mainly due to metal sintering as confirmed by XRD data.

Cu-based catalysts have also received particular attention. Cavallaro *et al.* [62] investigated steam reforming of ethanol over $CuO/ZnO/Al_2O_3$ and found that the catalyst exhibited good activity with CO, CO_2 and H_2 as the main products above 350 °C. Amphlett *et al.* [63-66] suggested that CuO/ZnO, CuO/SiO_2, CuO/Cr_2O_3 or $CuO/NiO/SiO_2$ might prove promising for reforming of ethanol–water mixtures at 350-450 °C. To our knowledge, no works on the catalytic performance of Cu/Al_2O_3 are present in literature.

Taking into account our results, it is clear that neither copper nor nickel alone supported on alumina appear as appropriate catalysts for ethanol steam-reforming under low temperature (T < 500 °C) conditions for hydrogen production. Over the copper sample, dehydrogenation of ethanol into acetaldehyde occurs but the reforming reaction does not proceed further to yield H_2 and CO_x. On the other hand, on the nickel sample, the decomposition reaction of ethanol to CH_4 and CO_x is favored. Only at high temperature (T > 550 °C) methane production is inhibited by steam-reforming processes.

The activity of the bimetallic catalysts, during the first run-up experiment, is not very different (Fig. 4.15, c, d and e) from the monometallic Ni system. Indeed, the product distribution is similar and the Ni:Cu ratio does not seem to affect it. Small differences in the relative amounts of acetaldehyde and CO, are observed only at low temperature (T < 300 °C). As described in § 4.3.2, the introduction of copper in the catalyst formulation has a positive effect in methanol steam reforming, since it inhibits the formation of methane. In the case of ethanol, the situation seems to be different. However, it has to be taken into account that methane can be generated not only through carbon oxides hydrogenation, as in the methanol reforming, but also acetaldehyde decomposition (see Fig. 1.1 in Chapter 1). Thus, it is clear that competitive reaction pathways are involved and the global result will depend on the

kinetic of these steps related to the different activity of the metals. Despite their similar activity, these samples present different stability during the two subsequent run-up experiments. The Ni_3Cu_7-Al catalyst shows the lowest stability, probably due to modification of the active phase (e.g. alloy). On the contrary, no appreciable deactivation of the catalytic performance was observed in the case of Ni_5Cu_5-Al and Ni_7Cu_3-Al.

It is often reported that Cu addition enhances the performance of Ni in EtOH-SR [67-70]. Ni has limited WGS activity [55,60] but shows high hydrogenation activity and hence it may help in combining adsorbed H atoms on the catalyst surface to form molecular hydrogen [71]. On the contrary, Cu has limited steam reforming activity, but is a good dehydrogenation catalyst [72]; and shows high WGS activity. Therefore, in the bimetallic systems, Cu represents the active agent for steam reforming while Ni favors the C–C bond cleavage.

Marino *et al.* [67,68] tested at 300 °C a series of Ni-Cu-K/Al_2O_3 catalysts, where potassium was added in the catalyst formulation to neutralize the acidic sites of the support. In this work, the authors discuss the effect of the Ni:Cu ratio and of the calcination temperature on the different phases present in the final catalysts. The activity, selectivity and stability of these materials is related to the different species formed during the thermal/chemical treatments (e.g. reduction) before the catalytic test. The selectivity for CH_4 was found to decrease as the calcination temperature increases. This fact was attributed to Ni–support interaction, which becomes stronger as the calcination temperature increases (from 450 °C to 800 °C), in paralle with a decrease of the nickel reducibility. Considering that metallic nickel is able to catalyze ethanol dehydrogenation to acetaldehyde, the decrease in reducibility of this metal as temperature increases explains the observed slight reduction in the catalytic activity. The reduced Ni(6 wt.%)Cu(6 wt%)-K/Al_2O_3 sample showed the best performance among the studied samples.

In the present work, all samples were calcined at intermediate temperature (600 °C) leading to the formation of species which are easily reduced at 750 °C in H_2, as confirmed by TPR data (see § 4.2).

At this point, it is also interesting to note that a way to combine the different catalytic activity of Ni and Cu, is the use of a two-layer fixed bed reactor. This approach seems to be very promising [73]. At low temperature (300-400 °C), ethanol is first converted by dehydrogenation over Cu into acetaldehyde. The resulting mixture, which primarily consists of acetaldehyde, H_2 and excess of water, can then feed at temperatures around 450 °C over a second bed containing Ni catalyst, where it will undergo steam reforming.

The stability of the catalytic activity under isothermal conditions was tested for all samples at 700 °C after 3 run-up experiments. XRD data suggest that a change in the oxidation state of the active phase does not occur. However, a partial sintering of the

metal particles is observed. Average crystallite diameters of 11 nm and 50 nm were calculated for Ni_{10}-Al and Cu_{10}-Al, respectively. In the case of Ni_5Cu_5-Al, a segregation of NiO, with crystallites of 7 nm, from the alloy takes place. Thus, the remaining metal phase, with crystallites of 25 nm, becomes rich in Cu. Consistently, preliminary EXAFS measurements on the aged samples indicates a slightly increase in the C.N. of the first M-M shell with respect to the reduced / activated samples. This is indicative of a appreciable sintering of the active phase. Qualitative comparison between reference samples and the investigated materials, indicates that all the aged systems remains mainly in a reduced form. Partial oxidation /passivation is observed, as in the reduced samples (Table 4.2) , but with a minor extent. As discussed above these reoxidation is more likely associated with the prolonged samples exposition to air before EXAFS measurements. Notably, the bigger aged metal particles are less prompt to be oxidised with respect to the smaller metal particles of the freshly reduced samples.

References

[1] A.M.C. Wittborn, M. Costas, M.R.A. Blomberg, P.E.M. Siegbahn, Journal of Chemical Physics 107 (1997) 4318.

[2] M.R.A. Blomberg, P.E.M. Siegbahn, U. Nagashima, J. Wennerberg, Journal of the American Chemical Society 113 (1991) 424.

[3] P.E.M. Siegbahn, M.R.A. Blomberg, M. Svensson, Journal of the American Chemical Society 115 (1993) 1952.

[4] D.A. Hickman, L.D. Schmidt, Science 259 (1993) 343.

[5] F. Besenbacher, I. Chorkendorff, B.S. Clausen, B. Hammer, A.M. Molenbroek, J.K. Norskov, I. Stensgaard, Science 279 (1998) 1913.

[6] D.L. Trimm, Catalysis Today 37 (1997) 233.

[7] J.R. Rostrup-Nielsen, Ib. Alstrup, Catalysis Today 53 (1999) 311.

[8] L.B. Avdeeva, O.V. Goncharova, D.I. Kochubey, V.I. Zaikovskii, L.M. Plyasova, B.N. Novgorodov, Sh.K. Shaikhutdinov, Applied Catalysis A-General 141 (1996) 117.

[9] C.A. Bernardo, I. Alstrup, J.R. Rostrup-Nielsen, Journal of Catalysis 96 (1985) 517.

[10] Y. Li, J. Chen, Y. Qin, L. Chang, Energy and Fuels 14 (2000) 1188.

[11] K.S.W. Sing, D.H. Everett, R.A.W. Haul, L. Moscou, R.A. Pierotti, J. Rouquérol, T. Siemieniewska, Pure and Applied Chemistry 57 (1985) 603.

[12] R.S. Zhou, R.L. Snyder, Acta Crystallographica Section B-Structural Science 47 (1991) 617.

[13] J.H. Lee, E.G. Lee, O.S. Joo, K.D. Jung, Applied Catalysis A-General 269 (2004) 1.

[14] T.V. Reshetenko, L.B. Avdeeva, Z.R. Ismagilov, A.L. Chuvilin, V.A. Ushakov, Applied Catalysis A-General 247 (2003) 51.

[15] S. Calvin, C.J. Riedel, E.E. Carpenter, S.A. Morrison, R.M. Stround, V.G. Harris, Physica Scripta T115 (2005) 744.

[16] S. Calvin, S.X. Luo, C. Caragianis-Broadbridge, J.K. McGuinness, E. Anderson, A. Lehman, K.H. Wee, S.A. Morrison, L.K. Kurihara, Applied Physics Letters 87 (2005) 1.

[17] D.A. Monti, A. Baiker, Journal of Catalysis 83 (1983) 323.

[18] S.D. Robertson, Journal of Catalysis 37 (1975) 424.

[19] H.S. Roh, K.W. Jun, S.C. Baek, S.E. Park, Bulletin of Korean Chemical Society 23 (2002) 1166.

[20] H.S. Roh, K.W. Jun, W.S. Dong, J.S. Chang, S.E. Park, Y.I. Joe, Journal of Molecular Catalysis A-Chem. 181 (2002) 137.

[21] J. Ye, Z. Li, H. Duan, Y. Liu, Journal of Rare Earth 24 (2006) 302.

[22] A.J. Akande, R.O. Idem, A.K. Dalai, Applied Catalysis A-General 287 (2005) 159.

[23] O.S. Joo, K.D. Jung, Bulletin of Korean Chemical Society 23 (2002) 1149.

[24] R.C. Jin, Y.X. Chen, W.Z. Li, W. Cui, Y.Y. Ji, C.Y. Yu, Y. Jiang, Applied Catalysis A-General 201 (2000) 71.

[25] M.D. Gross, J.M. Vohs, R.J. Gorte, Journal of Material Chemistry 17 (2007) 3071.

[26] H.S. Bengaard, J.K. Norskov, J. Sehested, B.S. Clausen, L.P. Nielsen, A.M. Molenbroek, J.R. Rostrup-Nielsen, Journal of Catalysis 209 (2002) 365.

[27] D. Dissanayake, M.P. Rosynek, K.C.C. Kharas, J.H. Lunsford, Journal of Catalysis 132 (1991) 117.

[28] P. Kim, Y. Kim, H. Kim, I.K. Song, J. Yi, Applied Catalysis A-General 272 (2004) 157.

[29] S. Xu, R. Zhao, X.L. Wang, Fuel Process Technology 86 (2004) 123.

[30] D. Ma, D.J. Mei, X. Li, M.C. Gong, Y.Q. Chen, Journal of Rare Earth 24 (2006) 451.

[31] Z.W. Liu, K.W. Jun, H.S. Roh, S.C. Baek, S.E. Park, Journal of Molecular Catalysis A-Chem. 189 (2002) 283.

[32] Y. Lu, J. Xue, C. Yu, Y. Liu, S. Shen, Applied Catalysis A-General 174 (1998) 121.

[33] H.S. Roh, K.W. Jun, W.S. Dong, S.E. Park, Y.I. Joe, Chemistry Letters (2001) 666.

[34] Q. Miao, G. Xiong, L. Xu, S. Sheng, X. Guo, Chin. Journal of Catalysis 18 (1997) 17.

[35] H.T. Wang, Z.H. Li, S.X. Tian, Reaction Kinetics and Catalysis Letters 83 (2004) 245.

[36] V.A. Tsipouriari, X.E. Verykios, Studies in Surface Science and Catalysis 119 (1998) 795.

[37] Q. Yan, H. Toghiani, M.G. White, Journal of Physical Chemistry C 111 (2007) 18646.

[38] K.C. Khulbe, R.S. Mann, Catalysis Reviews 24 (1982) 311.

[39] J.H. Sinfelt, J.L. Carter, D.J.C. Yates, Journal of Catalysis 24 (1972) 283.

[40] V. Ponec, Applied Catalysis A-General 222 (2001) 31.

[41] A. Roberti, V. Ponec, W.M.H. Sachtler, Journal of Catalysis 28 (1973) 381.

[42] N.D. Lang, H. Ehreneich, Physical Reviews 168 (1968) 605.

[43] J.H. Kim, D.J. Suh, T.J. Park, K.L. Kim, Applied Catalysis A-General 197 (2000) 191.

[44] Y.H. Chin, D.L. King, H.S. Roh, Y. Wang, S.M. Heald, Journal of Catalysis 244 (2006) 153.

[45] J. H. Sinfelt, Bimetallic Catalysts. Discoveries, Concepts and Applications. Wiley, New York, 1983.

[46] M. Agnelli, C. Mirodatos, Journal of Catalysis 192 (2000) 204.

[47] Y. Liu, T. Hayakawa, T. Tsunoda, K. Suzuki, S. Hamakawa, K. Murata, R. Shiozaki, T. Ishii, M. Kumagai, Topics in Catalysis 22 (2003) 205.

[48] V. Ponec. New Trends in CO activation. Guczi, L. Ed., Vol. 64, p.117, 1991. New York, Elsevier. Studies in Surface Science and Catalysis.

[49] J. Schwank. New trends in CO activation. Guczi, L. Ed., Vol. 64, p.225, 1991. New York, Elsevier. Studies in Surface Science and Catalysis.

[50] V. Ponec and G. C. Bond. Catalysis by Metals and Alloys., Vol. 95, 1995. Amsterdam, Elsevier Science BV. Studies in Surface Science and Catalysis.

[51] A.N. Fatsikostas, X.E. Verykios, Journal of Catalysis 225 (2004) 439.

[52] S. Freni, S. Cavallaro, N. Mondello, L. Spadaro, F. Frusteri, Journal of Power Sources 108 (2002) 53.

[53] A. Carrero, J.A. Calles, A.J. Vizcaino, Applied Catalysis A-General 327 (2007) 82.

[54] H.V. Fajardo, L.F.D. Probst, Applied Catalysis A-General 306 (2006) 134.

[55] F. Aupretre, C. Descorme, D. Duprez, Catalysis Communication 3 (2002) 263.

[56] J.W.C. Liberatori, R.U. Ribeiro, D. Zanchet, F.B. Noronha, J.M.C. Bueno, Applied Catalysis A-General 327 (2007) 197.

[57] A.L. Alberton, M.M.V.M. Souza, M. Schmal, Catalysis Today 123 (2007) 257.

[58] M.S. Batista, R.K.S. Santos, E.M. Assaf, J.M. Assaf, E.A. Ticianelli, Journal of Power Sources 124 (2003) 99.

[59] J. Llorca, P.R. de la Piscina, J.A. Dalmon, J. Sales, N. Homs, Applied Catalysis B-Environmental 43 (2003) 355.

[60] J. Comas, F. Marino, M. Laborde, N. Amadeo, Chemical Engineering Journal 98 (2004) 61.

[61] A. Akande , R.O. Idem, A.K. Dalai, Applied Catalysis A-General 287 (2005) 159.

[62] S. Cavallaro, S. Freni, International Journal of Hydrogen Energy 21 (1996) 465.

[63] J.C. Amphlett, R.F. Mann, B.A. Peppley, C.P. Thurgood, Catalyst Deactivation 2001, Proceedings 139 (2001) 205.

[64] L.M. Kearns, J.C. Amphlett, R.F. Mann, B.A. Peppley, Abstracts of Papers of the American Chemical Society 215 (1998) U488.

[65] B.A. Peppley, J.C. Amphlett, L.M. Kearns, R.F. Mann, Applied Catalysis A-General 179 (1999) 21.

[66] B.A. Peppley, J.C. Amphlett, L.M. Kearns, R.F. Mann, Applied Catalysis A-General 179 (1999) 31.

[67] F. Marino, M. Boveri, G. Baronetti, M. Laborde, International Journal of Hydrogen Energy 29 (2004) 67.

[68] F. Marino, G. Baronetti, M. Jobbagy, M. Laborde, Applied Catalysis A-General 238 (2003) 41.

[69] F. Marino, M. Boveri, G. Baronetti, M. Laborde, International Journal of Hydrogen Energy 26 (2001) 665.

[70] F. Marino, E.G. Cerrella, S. Duhalde, M. Jobbagy, Laborde.M.A., International Journal of Hydrogen Energy 23 (1998) 1095.

[71] J. Kugai, S. Velu, C. Song, Catalysis Letters 101 (2005) 255.

[72] Y.J. Tu, Y.W. Chen, Industrial & Engineering Chemistry Research 37 (1998) 2618.

[73] P.D. Vaidya, Chemical Engineering Journal 117 (2006) 39.

Chapter 5

Embedding strategy extension: non-precious metals

5.1 Introduction

As extensively expressed in § 1.2, the development of catalyst synthesis methods which produce and stabilize metal particles of controlled nano-size and narrow size distribution is an important task in heterogeneous catalysis, since it offers promising opportunities. In conventional catalysts, the active phase is usually supported on an oxide of high surface area to prevent the excessive mobility of the metal particles. In spite of the dispersion of these metal particles, catalysts often undergo deactivation due to the process of sintering, which occurs due to particle growth and agglomeration. This behavior, accompanied by a corresponding loss of the catalytic activity, is a serious problem in many applications. The design of a novel sinter-stable catalyst needs to meet the following requirements: a) its components have to be thermally very stable to maintain the integrity of the system; b) it should retain the catalytic activity after high-temperature treatment.

The encapsulation of pre-formed metal nanoparticles in a porous oxide, described in § 3.1, was demonstrated to be a successful approach to limit the metal agglomeration in the case of Rh-based systems even under severe working conditions (e.g. high temperatures). In this chapter, the extension of the embedding strategy to non-precious metals, like Ni and Cu, is discussed.

At the present time, the impregnation technique is probably the most commonly used procedure for Ni/Cu-based catalyst preparation. This method typically yields a wide metal particle size distribution, and average particle sizes which are difficult to control. It is also important to note that, although in some cases a homogeneous metal distribution is obtained, the subsequent chemical/thermal treatments (e.g. reduction), which are required for the activation of the catalysts, give usually opposite results.

On the other hand, the embedding approach could lead to a better and stricter control of the catalyst dimensions at the nanometer scale. In this way, the ability to manipulate the particle size and the particle size distribution in a reproducible manner could be achieved. Consequently, this would allow to maintain the useful relation between the reactivity and the particle size during catalyst aging.

The first step of the embedding strategy involves the preparation of a stable suspension of protected metal nanoparticles, followed by the deposition and growth of the porous oxide layers around each metal nanoparticle. These two steps will be described in § 5.2 and § 5.3, respectively.

5.2 Ni and Cu nanoparticles synthesis

The effective control of the particle size is one of the most difficult challenges for researchers involved in the synthesis of nanoparticle dispersions. In addition, since individual nanoparticles have a tendency to form agglomerates during the preparation

process, control of the particle-particle interaction is critical for obtaining a stable dispersion.

The growth of nanoparticles can be achieved through a wide variety of different routes. However, among these methods, mainly wet chemical processes are used to produce nanoparticles due to their straightforward nature and their potential to produce large quantities of the final product. They are the most convenient ways to control the size and shape of the particles.

Whatever the specific chemical method used, a stabilizing agent is always necessary to prevent the aggregation of the formed nanoparticles into larger assemblies. The nanoparticles stabilization and thus the means to preserve their finely dispersed state is a crucial aspect to consider during their synthesis [1]. In the absence of the stabilizer, the particle dispersion is inherently unstable with respect to agglomeration. Stabilization can be accomplished in two ways: electrostatic (charge, or inorganic) stabilization and steric (organic) stabilization [2]. Several types of stabilizing and protective agents for metal particles have been thoroughly investigated.

Ionic compounds such as halides, carboxylates, or polyoxoanions, dissolved in (generally aqueous) solution can generate the electrostatic stabilization. The adsorption of these compounds and their related counterions on the metallic surface will generate an electrical double-layer around the particles. This results in a coulombic repulsion between the particles. If the electric potential associated with the double layer is high enough, then the electrostatic repulsion will prevent particle aggregation. Colloidal suspensions stabilized by electrostatic repulsion are very sensitive to any phenomenon able to disrupt the double layer like ionic strength or thermal motion.

A second means by which metal colloids can be prevented from aggregating is to use macromolecules such as polymers. The adsorption of these molecules at the surfaces of the particles will provide a protective layer. By contrast with the electrostatic stabilization, which is mainly used in aqueous media, the steric stabilization can be used in organic or in aqueous phase. Nevertheless, the length and/or the nature of the macromolecules adsorbed influence the thickness of the protective layer and can thus modify the stability of the colloidal metal particles.

Finally, the electrostatic and steric stabilization can be combined to maintain metallic nanoparticles stable in solution. This kind of stabilization is generally provided by means of surfactants (the surfactant was used in the Rh nanoparticle synthesis). The way through which these amphipathic molecules work, was discussed in § 3.1.

The chemical reduction of transition metal salts in the presence of stabilizing agents to generate zerovalent metal particles in aqueous or organic media is one of the most common and powerful synthetic methods in this field [3-5]. The wide application of this method stems from its simplicity and reproducibility. The salt reduction method allows to prepare colloidal nanoparticles with a narrow size distribution. A wide range of reducing agents have been used to obtain nanoparticles: gases such as hydrogen or

carbon monoxide, hydrides or salts such as sodium borohydride or sodium citrate, or even oxidable solvents such as alcohols which can act both as solvent and reducing agent [6].

The reduction of metal salts is the result of redox reactions in which electrons from a reducing agent are transferred to the metal according to the following schematic chemical equation:

$$mMe^{n+} + n\,\mathrm{Re}\,d \rightarrow mMe^{0} + nO_x \qquad (6.1).$$

Chemical reduction is a multifactor process, which offers a variety of parameters that can influence the physical and chemical properties of the resulting particles. It depends on the choice of a redox pair and on the concentration of its components as well as on the temperature, pH of the medium, and diffusion and sorption characteristics. Particle size distribution is strongly governed by the interplay between two processes which occur during preparation: nucleation and particle growth. In principle, the particle size can be pre-determined by influencing the relative rates of these two processes. This can be achieved by varying the reaction conditions (e.g. temperature, type and concentration of the metal precursor, as well as the nature of the stabilizing or reducing agent).

In the present work, Ni and Cu nanoparticles were prepared by the reduction of $Ni(NO_3)_3$ and $Cu(NO_3)_3$ salts with $NaBH_4$ at RT and in the presence of:

1. N-hexadecyl-N-(2-hydroxyethyl)-N,N-dimethyl ammonium bromide

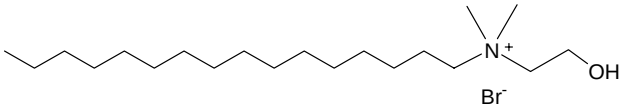

(HEAC16Br)

2. N,N-dimethylethanolamine

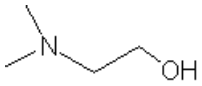

(DMEA)

3. Hexadecylamine

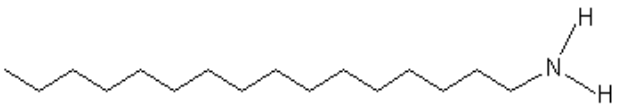

(HDA)

4. Polyvinilpirrolidone (40000)

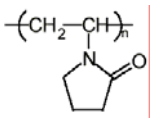

(PVP)

In order to avoid the reoxidation of Ni and Cu nanoparticles, the syntheses were performed in organic media. Ethanol was commonly used as solvent, with exception of HDA, due to its low solubility in the alcohol, and tetrahydrofuran (THF) was used instead. Notably, ethanol is not a suitable reducing agent at room temperature for both metals.

In a typical procedure, $NaBH_4$ was dissolved in the solution of the stabilizing agent. The resulting solution was quickly added under vigorous stirring to the solution of $Ni(NO_3)_2$ or $Cu(NO_3)_2$, used as metal precursors. The starting color of the metal solution changes rapidly to dark, indicating that colloidal nanoparticles are generated. The suspension was then stirred for 2 h in order to completely decompose the excess of $NaBH_4$. Without the protective agent, a stable suspension was not observed. Indeed, metal particles show a great tendency to agglomerate in relatively short times.

No stable suspension was prepared with HEAC16Br for both metals, even changing the surfactant/metal ratio. On the contrary, high PVP/metal (> 20) and $NaBH_4$/metal (> 5) ratios are required for nickel. In the case of copper, the situation is significantly more complex due to the stable intermediate oxidation state of Cu. Under the adopted experimental conditions it is possible to obtain stable suspensions with different nature and/or morphology of the nanoparticles. In parallel, different colors of the solution/suspension of the nanoparticles, ranging from orange to green, are obtained depending on the ratio PVP to metal.

It is generally accepted that long chain alkylamine, like HDA, can have a strong ability to coordinate metal surfaces. Monodisperse Ni nanoparticles around 3.7 nm were prepared by Hou *et al.* thorough the reduction of $Ni(acac)_2$ (acac ~ acetylacetone) with sodium tetrahydridoborate in a monosurfactant system, in which HDA serves as stabilizer and solvent, without any further size selective process [7,8].

Herein, we report the preliminary results obtained for Ni nanoparticles synthesized using HDA in THF. We examined the effect of HDA/Ni and $NaBH_4$/Ni molar ratio on the Ni particle size. The Table 5.1 lists the samples which are characterized by means of TEM.

Table 5.1: Ni nanoparticles prepared using different HDA/Ni and $NaBH_4$/Ni molar ratios

		$NaBH_4$/Ni		
		2.5	5	7.5
HDA/Ni	0	-	Ni0	-
	5	-	Ni5	-
	15	Ni15-2.5	Ni15	Ni15-7.5
	20	-	Ni20	-
	30	-	Ni30	-

The preliminary TEM characterization, indicates that at $NaBH_4$/Ni = 5. When the HDA/Ni increases from 5 to 15, the mean diameter of the Ni nanoparticles decreases from 4 to 2.5 nm. Higher ratios do not affect the particle size.

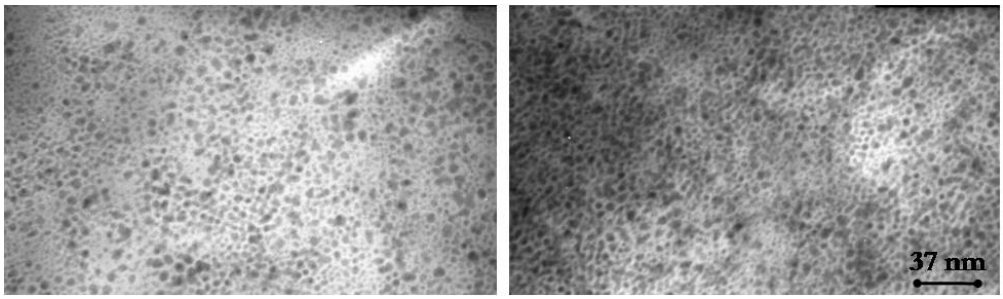

Figure 5.1: TEM images of Ni nanoparticle protected by HDA (HDA/Ni = 15 and $NaBH_4$/Ni = 5), 1 cm = 37 nm.

At constant HDA/Ni = 15, the mean diameter of the Ni nanoparticles decreases as the $NaBH_4$/Ni decreases. This phenomenon could be explained from the influence of reduction rate on the nucleation and particle growth. Since a minimum number of atoms are required to form a stable nucleus, a collision between several atoms must occur for nucleation. However, the probability is much lower than the probability for the collision between one atom and a nucleus already formed. The number of nuclei formed at the very beginning of the reduction determines the number and size of the final particles. At high $NaBH_4$/Ni ratio, the reduction rate is fast and many nuclei are formed in the early period of the reduction, but, evidently they are not very stable and tend to agglomerate in larger particles. On the other hand, at low $NaBH_4$/Ni ratios, although the reduction rate is slow and only few nuclei are produced, they are more stable towards the aggregation.

5.3 Nanoparticles embedding

In the case of $Rh@Al_2O_3$ systems, pre-formed and protected metal nanoparticles were embedded into the alumina through a simple precipitation technique (§ 3.1). The same approach cannot be employed for Ni and Cu and here we analyze the reasons why this procedure is not successful.

The problems are related to the low stability of the metal suspension in the presence of aqueous solutions of Al salts. Indeed, the addition of aluminium nitrate leads to a significant decrease of the pH of the resulting solution. At low pH values, both Ni and Cu nanoparticles are easily oxidized and dissolved. In the case of Rh, the metal nanoparticles are stable in acidic media. Consistently, the starting suspension of protected Rh nanoparticles has an acidic character (pH ~ 3).

To overcome these problems, the $Al(NO_3)_3$ was dissolved in an ethanol solution of TetraMetylAmmoniumHydroxide (TMAH). The obtained solution was added to the metal suspension. The controlled precipitation of Al hydroxide was realized by CO_2 bubbling to reduce the pH. Unfortunately, the small amount of water produced during this process was enough to mostly re-oxidize the metal nanoparticles. In addition to this, in the case of Ni, the calcination in air at 600 °C of the final material, which is necessary to transform the Al hydroxide into alumina, leads to a blue-coloured sample. This is a clear indication for the formation of nickel aluminate species, as also confirmed by XRD (Fig. 5.2).

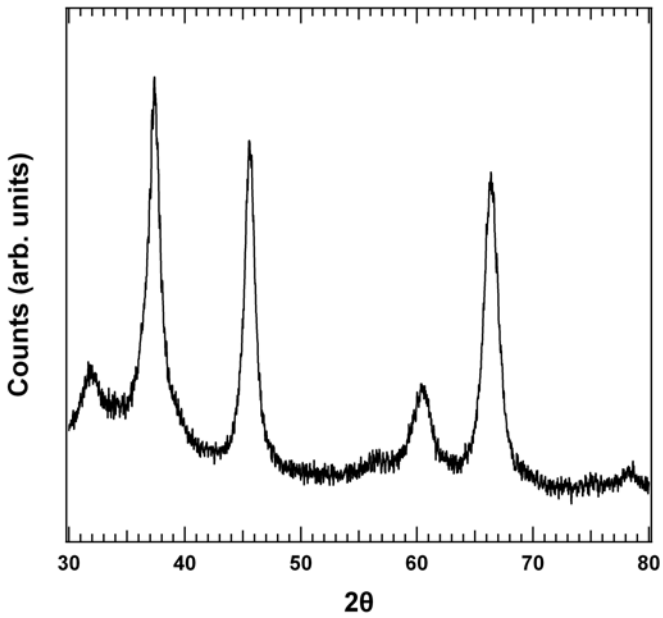

Figure 5.2: XRD powder diffraction profiles of Ni(10 wt.%)@Al_2O_3 obtained using DMEA as protective agent and $NaBH_4$ as reducing agent for Ni nanoparticles.

Notably, the calcination at the same temperature does not have a similar effect in the corresponding impregnated system (Ni_{10}-Al, § 4.2), indicating the different nature of the involved species. This preliminary work could be continued by attempted calcinations under reducing/inert conditions or by changing the Al precursor, investigating for instance the use of Al alcohoxides.

The deposition of the pre-formed particles on the support can avoid the problems mentioned above. However, a significant lower activity was observed, for instance in methane partial oxidation, with respect to the impregnated samples, as depicted in Fig. 5.3.

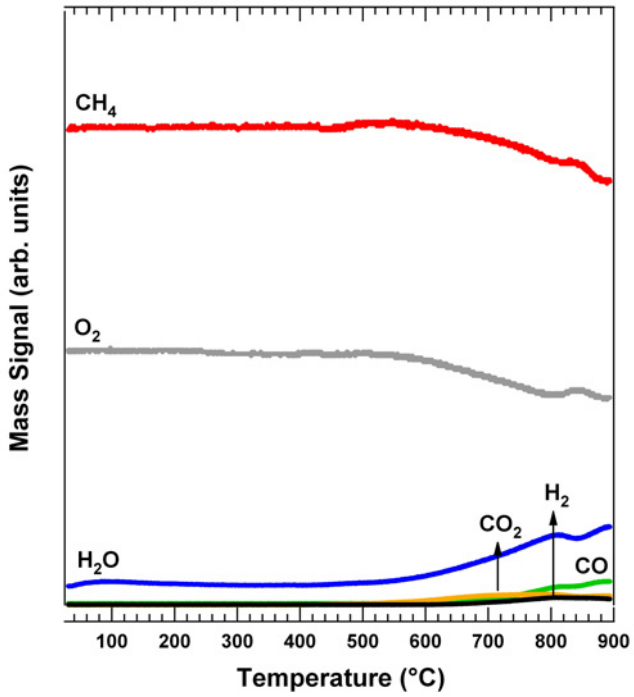

Figure 5.3: Methane Partial Oxidation over reduced nanoNi(10%)/Al_2O_3-IMP. Conditions: CH_4 (2.0%) + O_2 (1.0%) in Ar, GHSV = 100000 mL g^{-1} h^{-1}.

This negative behavior could be associated with the presence of residues of the stabilizer, used as protective agent for metal particles, or of decomposition products of the reducing agent (e.g. Na). These poisoning compounds are indeed difficult to be removed from the catalyst. In the case of Ni nanoparticles protected by DMEA, TPO experiments point out that a simple calcination step at 500 °C for 5 h in air is not sufficient to fully eliminate all the surfactant (Figure 5.4). Higher calcination temperatures are required (e.g. 650 °C), which are however incompatible with the nature of the system. In fact, formation of inactive Ni aluminate species (e.g. $NiAl_2O_4$) are detected.

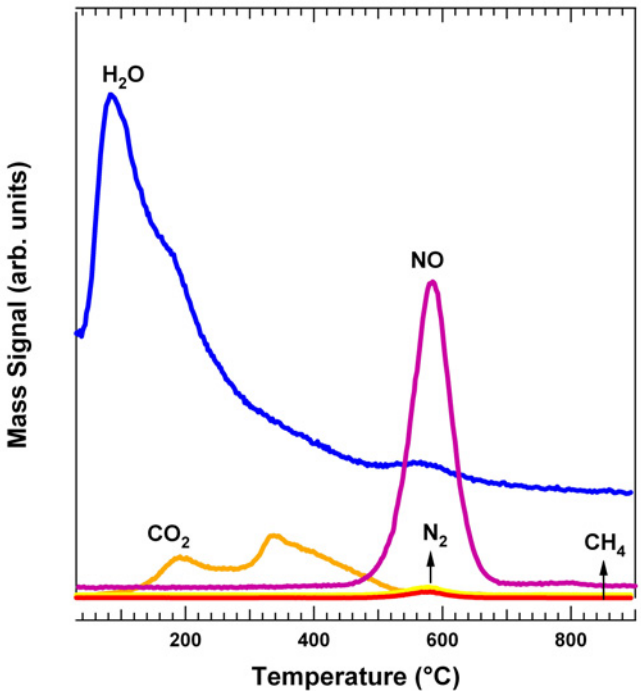

Figure 5.4: TPO experiment performed on Ni nanoparticles protected by DMEA and deposited on commercial Al_2O_3 (Sasol HP 14-150 calc. 900 °C for 24 h with a specific surface area of 97 $m^2 g^{-1}$).

The nature of the reducing agent also plays a key role in the loss of the catalytic activity. It is commonly accepted that Na has a detrimental effect on the surface area stability of many oxides, and on alumina in particular. In order to clarify its influence on the activity of our catalysts, the alumina employed in the preparation of the samples discussed in chapter 4 was impregnated with $NaBH_4$. The resulting material was calcined at 600 °C for 6 h. This sample showed a significant lower surface area (42 m^2/g) with respect to bare Al_2O_3 (97 m^2/g). Furthermore, even after a dozen washing cycles with water before calcination, the sample shows no appreciable enhancement of the surface area (45 m^2/g). This behavior can be ascribed to the presence of Na, which strongly interacts with the catalyst leading to the support sintering [9]. The washing cycles with water are therefore inadequate to yield a complete elimination of Na.

Notably, with respect to the embedded rhodium catalysts, the amount of $NaBH_4$ used in the reduction process is higher. However, in the case of the embedded system, Na can be partially buried into the support during the aluminium hydroxide precipitation. This makes the elimination of Na even more difficult. Finally, it must be noticed that in the case of Rh, the lower amount of $NaBH_4$ required for the reduction of the Rh (1 wt% and $NaBH_4/Rh$ = 2.5) with respect to the Ni (10 wt.% and $NaBH_4/Ni$= 5) case, prevents similar serious deactivation phenomena.

References

[1] D. H. Everett, Basic Principles of Colloid Science. Royal Society of Chemistry, London, 1988.

[2] A. Roucoux, J. Schulz, H. Patin, Chemical Reviews 102 (2002) 3757.

[3] N. Toshima, T. Yonezawa, New Journal of Chemistry 22 (1998) 1179.

[4] J.D. Aiken, R.G. Finke, Journal of Molecular Catalysis A: Chemical 145 (1999) 1.

[5] J.S. Bradley, Clusters and Colloids. VCH, Weinheim, 1994, pp. 469-473.

[6] B.L. Cushing, V.L. Kolesnichenko, C.J. O'Connor, Chemical Reviews 104 (2004) 3893.

[7] Y. Hou, H. Kondoh, T. Ohta, S. Gao, Applied Surface Science 241 (2005) 218.

[8] Y. Hou, S. Gao, Journal of Materials Chemistry 13 (2003) 1510.

[9] R. Snel, Applied Catalysis 11 (1984) 271.

Chapter 6

CO_2 hydrogenation under ultra high vacuum and high pressure conditions

---

6.1 Heterogeneous catalysis and ultra high vacuum environment

A central goal in heterogeneous catalysis research is to obtain a detailed understanding of the relation between the atomic-scale structure of a catalyst and its catalytic activity and selectivity. In this respect, ultra high vacuum techniques represent useful means and are widely used. However, it is important to underline that the very low pressures required for UHV surface science studies are many orders of magnitude below the pressures used in practical catalytic processes ($p \geq 1$ atm). Furthermore, many chemical reactions occurring at the surface of solid materials proceed only under high pressures of the gaseous reactants but not at low pressures ($p < 10^{-6}$ mbar) despite favorable thermodynamics [1]. The different reactivity under UHV conditions is known as the pressure gap in heterogeneous catalysis [1-3].

An origin of this gap is the presence of a barrier to dissociative chemisorption of at least one of the reactants upon collision with the surface. Since it is the translational or internal energy of the incident molecule that is important in surmounting this barrier and not the surface temperature, the rate of the reaction is limited by the flux of incident molecules with energies above the energy of the barrier. High pressures increase the absolute number of high energy molecules, thereby increasing the reaction rate sufficiently for the products to be detected. As a result, the chemical behavior of catalytic systems can often change substantially under different pressure regimes. Furthermore, at sufficiently low pressures, the surface will adopt its clean, unperturbed structure, with gas molecules occasionally adsorbing, diffusing around and desorbing again. On the other hand, at sufficiently high pressure the gas phase will play an important role in the thermodynamics of the surface. In particular, by increasing the pressure over many orders of magnitude we raise the free energy, e.g. the chemical potential, of each gas phase molecule. This implies that the structure that would minimize the total energy of the surface plus the gas phase at low pressures may be quite different from the one that actually minimizes the free energy of the surface-plus-gas system at high pressures [4]. Competitive adsorption between reactants and possible various impurities (whose concentration can be significant at high partial pressure) can further complicate real catalyst behavior.

Hydrogenation reactions exemplify the above discussed problem of pressure gap. Generally, hydrogen adsorbs dissociatively on most transition metal surfaces. The reaction often requires to overcome a dissociation barrier which is some ten times higher than the average energy of gas phase H_2 at room temperature (0.06 eV). The energy which is gained upon atomic adsorption, has to balance the energy required for the dissociation of the molecule (Eq. 6.1) according to the following equation:

$$E_{ads} = E_{M-H} - \frac{1}{2} E_{diss}^{H_2} \qquad (6.1).$$

The use of an atomic hydrogen source under UHV conditions, as in this work, allows to overcome both the thermodynamic and kinetic limitations which ordinarily restrict hydrogenation to high pressures. In the case of activated dissociative adsorption, the hydrogen atomic beam allows to gain the H_2 molecule dissociation energy by eliminating this latter step and, consequently, more energy is available for surface reactions. In this way, it is possible to simulate higher pressures, thus reproducing in the analytical environment reaction conditions which are closer to "real" catalysis. With respect to molecules, impinging hydrogen atoms allow reaching a higher surface saturation coverage and hydrogen adsorption on metals where hydrogen molecules do not dissociate. Furthermore, hydrogen atoms can overcome the diffusion barrier to the bulk and populate subsurface adsorption sites. Notably, the use of an atomic hydrogen beam can significantly influence the chemistry of surface hydrogenation reactions, because a consistently higher energy is available and, different pathways can be sampled, as observed in CO_2 hydrogenation experiments (see § 6.2).

Another problem encountered in UHV studies, which has to be taken into account, refers to the use of a clean and well-defined single crystal plane to model a site or set of sites expected to exist on practical high-surface-area catalysts (structure or material gap). The physics behind this gap is usually associated with unique electronic properties of nm-sized metal particles, with the contribution of special sites, such as edges, to the reaction rate, and/or with metal-support interaction. The structure gap may, however, also be due to purely kinetic effects, such as the interplay of the reaction kinetics occurring on different facets of metal particles.

Up to now, significant efforts have been dedicated to bridging these gaps (e.g. the development of high pressure reactors and cells integrable into standard UHV equipment; the design of planar nanoparticle model catalysts, consisting of well-defined metal particles supported on thin oxide films or on oxide single crystals).

6.2 CO_2 hydrogenation on Ni(110)

6.2.1 Ni in the methanol synthesis

It was observed that Ni doping of a Cu(100) surface does non alter MeOH production from a CO_2/H_2 mixture, while admission of CO leads to a significant increase in the rate of methanol formation with a turnover frequency/Ni site which is 60 times higher than the turnover frequency/Cu site [5-7]. For a mixture of CO_2 and H_2 or CO and H_2, it was found that the rates of methanol formation are essentially identical. The enhancement was observed by having all the reactants present at the same time, and in particular it has to be correlated with the simultaneous presence of CO and Ni. The results mentioned above, which are summarized in Figure 6.1., can be explained in the following way.

In the Ni/Cu alloy the addition of CO to the stream promotes Ni segregation to the surface [8,9]. The driving force behind the surface segregation of Ni is the energy gain obtained by chemisorption of CO. This is due to the stronger bonding of CO to Ni, as compared to Cu. The amount of Ni which one will extract depends both on the CO partial pressure and temperature. Thus, the role of CO is most probably the enrichment of Ni at the surface.

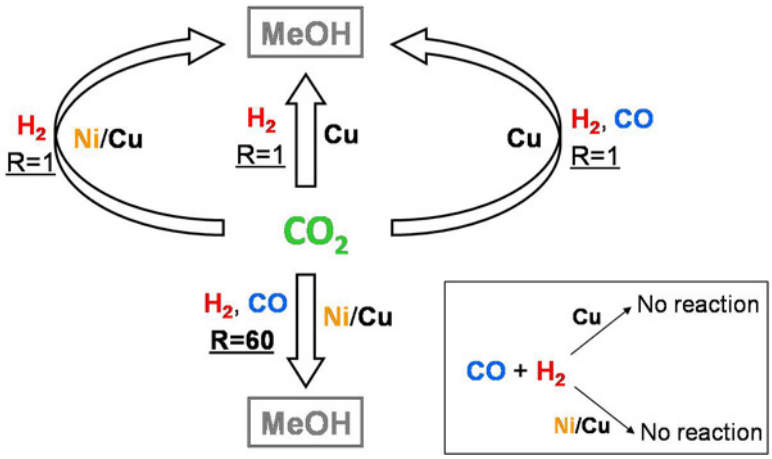

Figure 6.1: effect of Ni doping of Cu(100) surface on methanol synthesis. Reaction conditions: p(CO) ~ 100-300 mbar, p(CO_2) ~ 30-300 mbar, p(H_2) ~ 1400 mbar, T ~ 270 °C [5].

If we consider the possible reaction mechanisms (hydrogenation of CO_2 or CO), there are essentially two possibilities which can account for the observed behavior as depicted in Fig. 6.2. Either CO (and Ni) promotes the hydrogenation of CO_2 or, alternatively, CO_2 (and Ni) promotes the hydrogenation of CO. A direct hydrogenation of CO from a CO/H_2 mixture over Ni/Cu(100) was not observed. Although the possible role of CO_2 in promoting a direct CO hydrogenation cannot be completely excluded, this is taken as indication that most likely CO promotes the hydrogenation of CO_2. It is clear that the presence of Ni has also some role in the reaction pathway.

Notably, it was observed that formate is formed under UHV conditions in the case of coadsorption of H_2 and CO_2 on Ni(110) [10], whereas high pressures are needed in case of Cu(100) [9,11]. This means that a higher rate of formate formation could be anticipated for the Ni/Cu(100) system. Another possibility is that Ni affects the rate-limiting step, which has been suggested to be the hydrogenation of dioxomethylene (H_2CO_2) into methoxy (CH_3O) and adsorbed oxygen (Fig. 6.2) [12,13].

On the basis of the above considerations, the need for a deeper insight into the MeOH production reaction mechanism is clear. In order to understand the role of Ni and to identify the reaction intermediates and channels, we studied the CO_2 hydrogenation process on Ni single crystal (Ni(110)), as mentioned in Chapter 1 (§ 1.5).

The interaction of methanol and formic acid with the clean metal surface was also considered. Indeed, it is known that the intermediates involved in the methanol and formic acid interaction with the Ni surface (e.g. CH_3O and HCOO respectively) are also involved in the methanol synthesis reaction. Their identification by an analysis of the contribution to the XPS C1*s* and O1*s* components, as well as their thermal stability, will help in the interpretation of the hydrogenation reaction data. The experimental results are discussed in the next section.

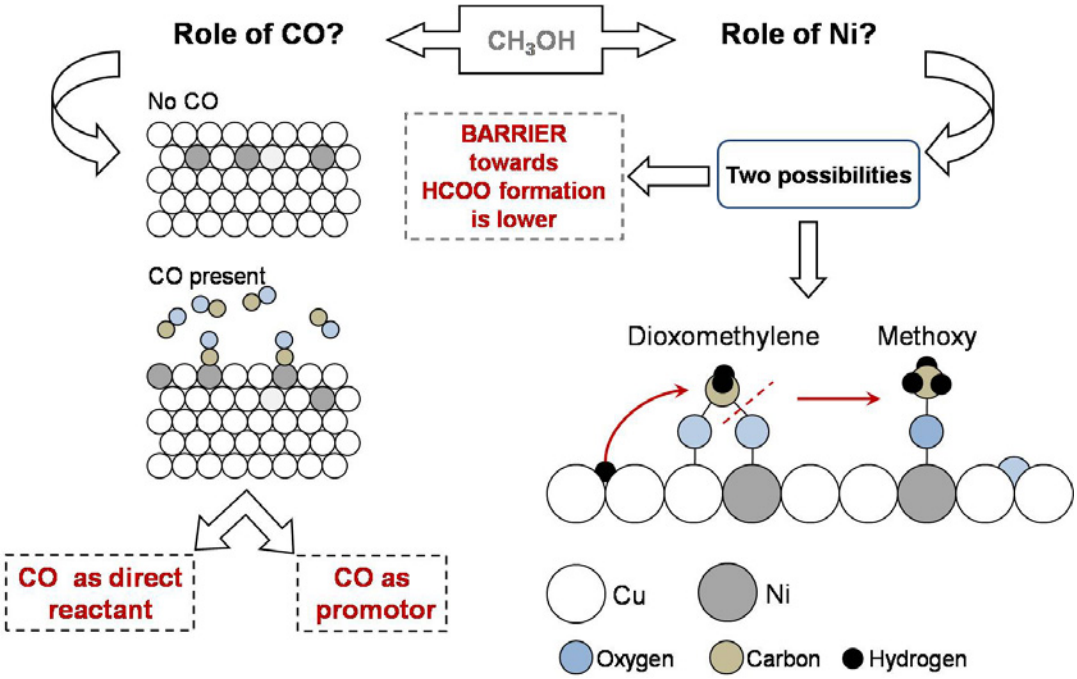

Figure 6.2: reaction mechanism proposed on Ni/Cu alloy [5].

6.2.2 Experimental results

- **TPD**

Fig. 6.3 shows TPD spectra collected after exposure at -180 °C of clean Ni(110) to 4 L CO_2 (lower panel), 4 L CO_2 + 10 L H_2 (middle panel) and 4 L CO_2 + 10 L H_{at} (upper panel).

Upon CO_2 adsorption, two distinct peaks are observed at -173 °C and -53 °C, respectively. The feature at low temperature is due to desorption of physisorbed CO_2 while the peak at higher temperature is related to the chemically bound CO_2 species. Desorption of the low temperature state starts immediately with heating, thus indicating that its coverage is limited by the adsorption temperature. On the contrary,

chemisorbed CO_2 is stable on the surface up to about -53 °C. At this temperature it partially dissociates into CO and oxygen, both remaining chemisorbed on the surface. The formed CO leaves the surface at temperatures between 100 °C and 167 °C. Instead, the atomic oxygen does not desorb as corroborated by LEED patterns which suggest formation of the (3×1)-O ordered structure already at 92 °C. CO and O recombination does not take place on this surface.

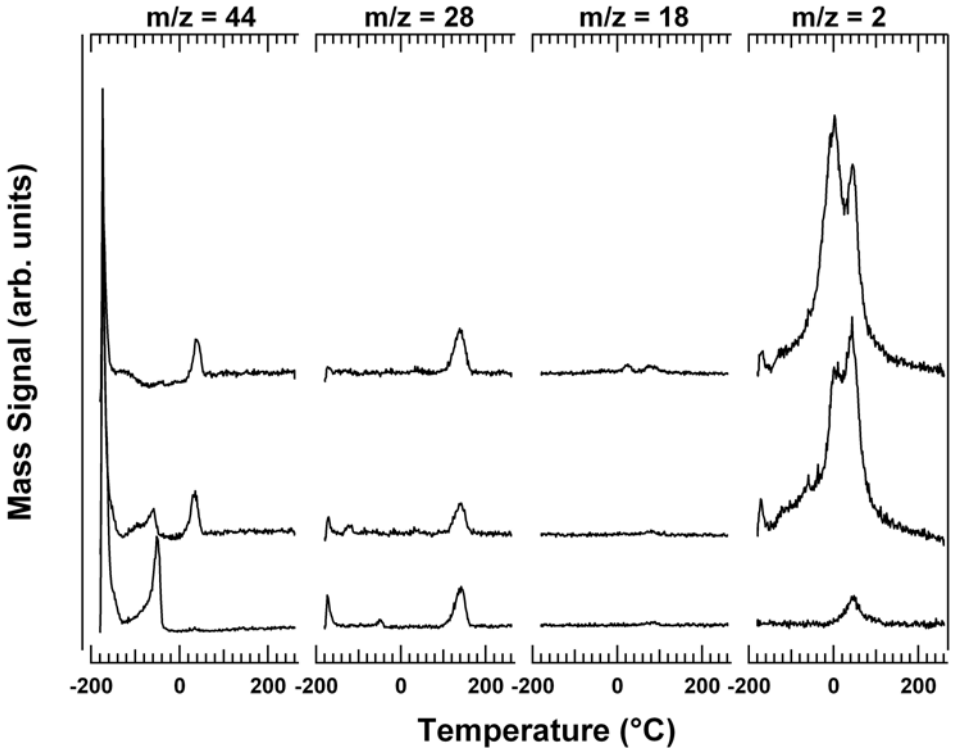

Figure 6.3: TPD data obtained upon exposure at -180 °C of clean Ni(110) in UHV to 4 L CO_2 (lower panel), 4 L CO_2 + 10 L H_2 (middle panel) and 4 L CO_2 + 10 L H_{at} (upper panel). Heating rate 1.5 °C/s.

For the CO_2+H_2 case, a new mass 44 desorption peak appears at 32 °C, which grows at the expense of the "-53 °C state" suggesting the formation of a reaction intermediate. This latter feature is also shifted to lower temperature (- 58 °C) due to possible "destabilization effects". When using atomic hydrogen, the 32 °C peak remains almost unaltered with respect to the molecular case, while the lower temperature peak disappears. A small broad feature grows at about -123 °C. When using H_2, desorbing CO is 25% less than in the CO_2 alone case. When using H_{at}, CO coverage is 10% higher than in the CO_2 alone experiment and therefore 50% higher than in the molecular hydrogen experiment. In the H_{at} case, water is also detected as a desorption product (two distinct mass 18 desorption peaks are present at 22 and 77 °C respectively) due to hydrogenation of the oxygen atoms originated from the CO_2

decomposition, as well as due to small contamination. Hydrogen desorption spectra are similar for the H_2 and H_{at} cases.

For comparison, adsorption of methanol and formic acid (1 L at -180 °C) were also performed (data not shown). Noteworthy, above -123 °C, in the case of methanol, only CO and H_2 are detected as products, while with formic acid CO_2 is also observed. This fact suggests the formation of formate intermediate in both hydrogenation experiments.

Interesting information can be obtained by combining these results with XPS and HREELS data, as discussed below.

- **XPS**

Fig. 6.4 reports carbon 1*s* core level spectra upon exposure at -180 °C of clean Ni(110) in UHV to 4 L CO_2 (left panel), 4 L CO_2 + 10 L H_2 (middle panel) and 4 L CO_2 + 10 L H_{at} (right panel).

At -180 °C, carbon dioxide spectra (left panel in Fig. 7.4) are characterized by two peaks at 286.2 and 290.6 eV associated to the chemisorbed and the multilayer states, respectively. The latter feature disappears already at -123 °C, in agreement with CO_2 desorption spectra (see Fig. 7.3), while the other peak vanishes between -123 °C and -33 °C, where carbon dioxide desorption and decomposition into CO occur. At -33 °C a peak at 285.1 eV, attributed to CO, is present and persists beyond 12 °C in agreement with CO desorption spectra.

Upon co-adsorption with molecular hydrogen, at -180 °C almost no difference can be observed in the spectra (middle panel in Fig. 6.4) with respect to the CO_2 alone experiment, apart from a decrease in the intensity of the multilayer related peak due to possible induced desorption. At -123 °C the physisorbed state is not present any more, in agreement with TPD experiment, and only the chemically bound CO_2 peak is present, unaltered. After heating to - 33 °C, an additional component grows at the expense of the chemisorbed CO_2 at 288.0 eV. This new contribution can be assigned to formate (HCOO), based on the results of previous XPS and STM studies [14,15]. The additional XPS component proves that the CO_2 feature observed in the TPD spectra at 32 °C is due to a hydrogenation process. The intensities of the XPS features indicate that 40% of the CO_2 is hydrogenated. Above 12 °C only the CO peak at 285.1 eV remains and vanishes at 227 °C in agreement with TPD experiment. Notably, from the intensities trend plots as a function of the annealing temperature, it can be seen that the carbon monoxide peak grows firstly between -123 °C and -33 °C due to CO_2 decomposition and secondly at 92 °C due to decomposition of the 286.9 or the 288.0 eV intermediates and in parallel with mass 44 desorption, thus indicating a dual decomposition mechanism (dehydrogenation and C-O bond cleavage).

In the case of atomic hydrogen, the spectrum at -180 °C is already different from the other cases, since two peaks grow at 285.5 and 288 eV in addition to the two CO_2 related features. Notably, the feature at 285.5 eV is not observed in the molecular

hydrogen experiment even after heating to higher temperatures. At -123 °C there is no more multilayer CO_2 (290.6 eV), while the 285.5 and 288.0 eV peaks have grown in intensity. At -33 °C, only two peaks are present at 285.1 (CO) and 288.0 eV (HCOO). After annealing at 92 °C there is only the CO feature, in agreement with TPD data, which disappears below 227 °C.

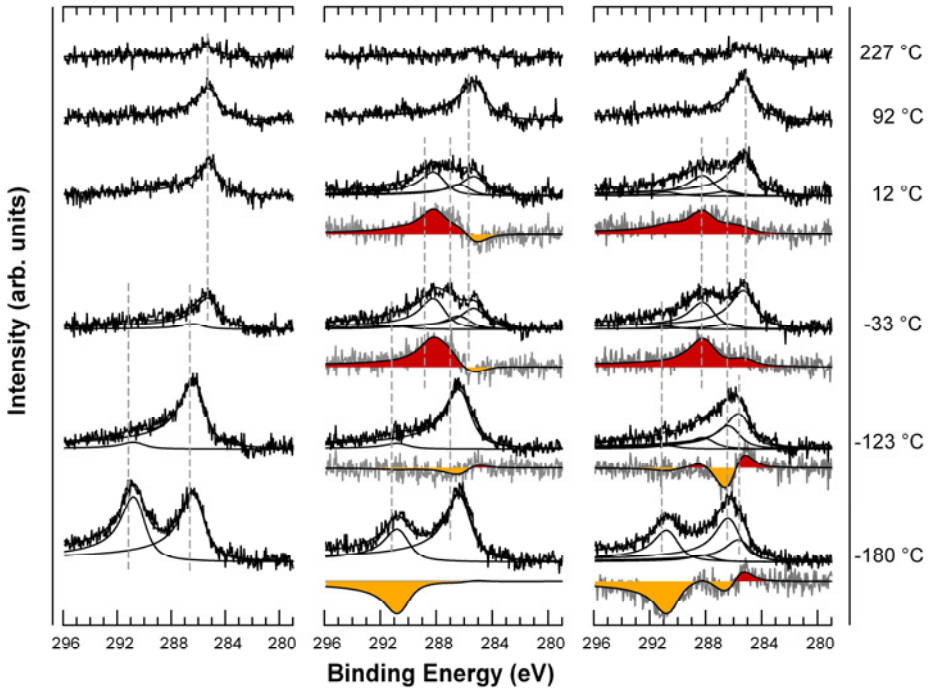

Figure 6.4: XPS spectra of the C1s core level region collected upon stepwise annealing of clean Ni(110) exposed to 4 L CO_2 (left panel), 4 L CO_2 + 10 L H_2 (middle panel) and 4 L CO_2 + 10 L H_{at} (right panel). The grey curves are difference spectra obtained by subtracting the spectra of the pure CO_2 experiment to the corresponding spectra of the CO_2+H_2/H_{at} experiments, where additional (red) and missing (yellow) contributions are highlighted.

Fig. 6.5 shows the evolution of the surface species and concentrations as a function of the annealing temperature. From the intensities trend plots, it can be observed that CO forms above -123 °C both from CO_2 decomposition as well as from the 285.5 eV intermediate. With respect to the carbon dioxide alone experiment, the CO coverage at -33 °C is almost the same, but the initial chemisorbed CO_2 coverage is half, thus indicating that part of it originates from the decomposition of the 285.5 eV intermediate. The decrease in intensity of the 288.0 eV peak between 12 and 92 °C does not reflect in a significant increase in the CO related peak intensity, thus indicating that species completely desorbs as CO_2 in the mass spectra. On the other hand, in the molecular hydrogen case CO peak grows firstly between -123 and -33 °C due to CO_2 decomposition and secondly at 92 °C due to decomposition of the 288.0 eV

intermediate and in parallel with mass 44 desorption, thus indicating a dual decomposition mechanism (dehydrogenation and dehydration).

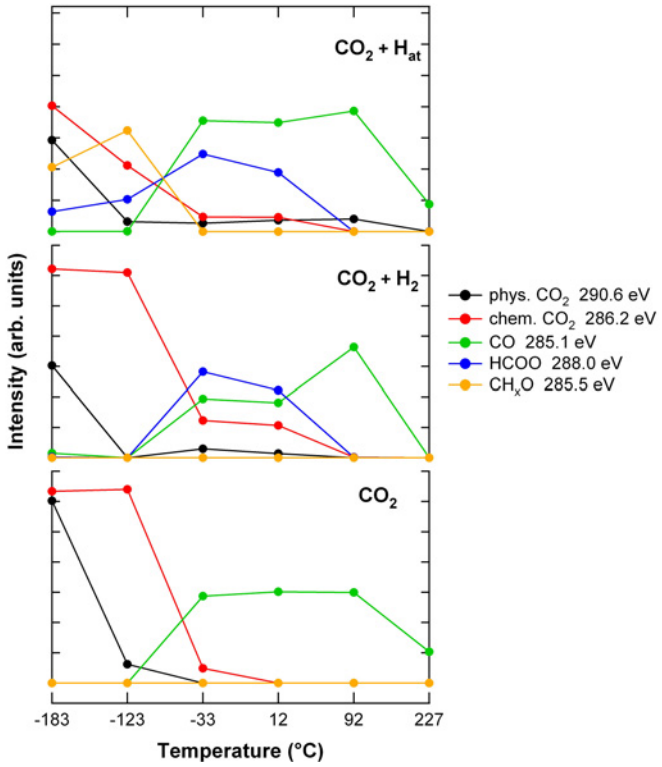

Figure 6.5: C1*s* intensities trend plots as a function of the annealing temperature for CO_2 (lower panel), CO_2 + H_2 (middle panel) and CO_2 + H_{at} (upper panel) experiments.

C1*s* spectra of Ni(110) exposed to 1 L MeOH at -180 °C, was also recorded. At this temperature (data not shown), the MeOH contribution at 286.4 eV (in perfect agreement with 286.4 eV on Ni(100) [16]) and the methoxy contribution at 286.0 eV are observed. In the literature C1*s* from methoxy is reported at 285.75 eV on Ni(100) [16]. Upon heating, the latter vanishes at -73 °C due to dehydrogenation process (no MeOH mass was detected in TPD).

On the basis of the above considerations, it is evident that an univocal assignment of 285.5 eV feature is not possible. However, its thermal stability on the surface, which is similar to that of methoxy reported in literature, suggests the formation of some CH_xO species.

Fig. 6.6 reports oxygen 1*s* core level spectra upon exposure at -180 °C of clean Ni(110) in UHV to 4 L CO_2 (left panel), 4 L CO_2 + 10 L H_2 (middle panel) and 4 L CO_2 + 10 L H_{at} (right panel).

In analogy to the C1*s* region, the O1*s* spectra of the pure CO_2 layer at -180 °C consist of two well separated peaks with binding energies of 534.0 eV and 530.6 eV,

which can be attributed, on the basis of previous data [17], to physisorbed and chemisorbed CO_2 species, respectively. The feature at high binding energy disappears after annealing to -123 °C according to TPD data. Moreover, a new component appears at 531.0 eV corresponding to CO. In addition to the CO related signal, at 92 °C a new peak grows at a binding energy of 529.3 eV, which is associated to atomic oxygen produced by chemisorbed CO_2 dissociation. After annealing to 227 °C the spectra show only the contribution of O species.

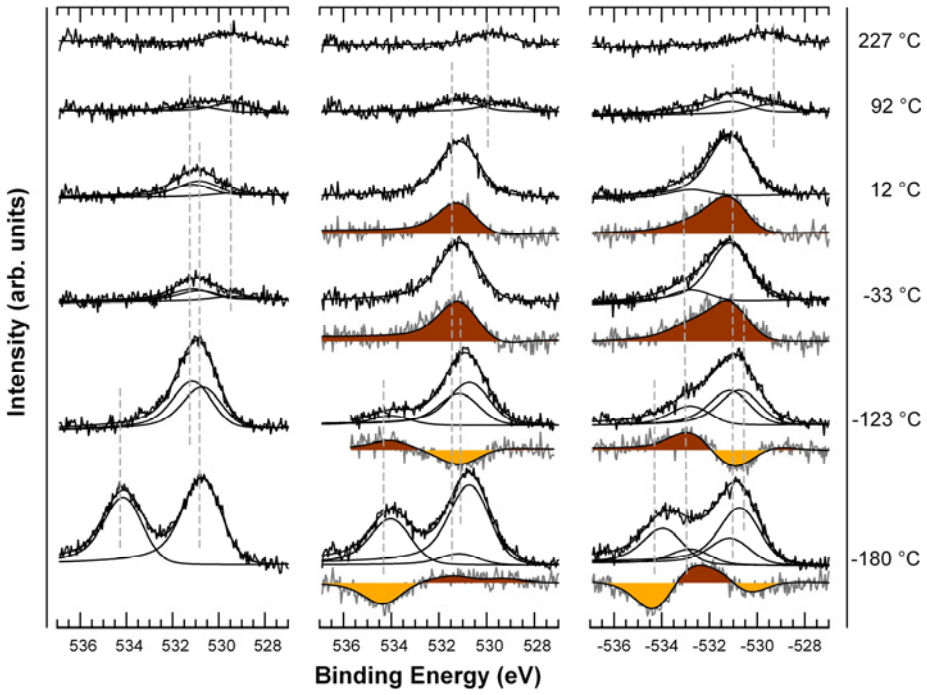

Figure 6.6: XPS spectra of the O1s core level region collected upon stepwise annealing of clean Ni(110) exposed to 4 L CO_2 (left panel), 4 L CO_2 + 10 L H_2 (middle panel) and 4 L CO_2 + 10 L H_{at} (right panel). The grey curves are difference spectra obtained by subtracting the spectra of the pure CO_2 experiment to the corresponding spectra of the CO_2+H_2/H_{at} experiments, where additional (red) and missing (yellow) contributions are highlighted.

Upon co-adsorption with molecular hydrogen, the complete set of spectra can be fitted by means of the same components of the carbon dioxide case, i.e. peaks at 529.3, 530.6, 531.0 and 534.0 eV. The main difference is that the 531.0 eV peak is present already at -180 °C and grows and remains constant up to 12 °C, where the mass 44 peak is observed in the TPD spectra. This is due to the fact that O-H (hydroxyl groups) and HCOO O1*s* contributions are all centered at almost the same binding energy than CO.

In the case of atomic hydrogen, the main difference with respect to the two other experiments is that at -180 °C a third peak is already present at 532.0 eV and

looses intensity between -123 °C and 12 °C, in parallel with the 285.5 eV feature in the C1*s* spectra. Noteworthy, upon MeOH adsorption at -180 °C we find an O1*s* contribution which is attributed to methoxy at 532.5 eV, while a value of 531.7 eV is reported in the literature [15]. Also in this case, the peak at 530.6 eV (e.g. CO, OH, HCOO) is stable up to more than 12 °C, in agreement with mass 44 desorption temperature in the TPD experiment. CO finally desorbs and atomic oxygen is left on the surface at 227 °C.

- **HREELS**

Fig. 6.7 shows HREELS spectra of Ni(110) exposed to 0.22 L of CO_2 at -186 °C and subsequently heated to different temperatures.

At low temperature (T < -173 °C) there are six prominent losses at 48 meV, 81 meV, 90 meV, 140 meV, 168 meV and 290 meV. Furthermore, two shoulders of the 140 meV peak around 128 meV and 150 meV are present. For increasing temperature, the high frequency peak at 290 meV decreases in intensity and completely disappears above -163 °C, while the other losses still persist. According to TPD and XPS data as well as to previous results [18,19] it is reasonable to associate this component to physically bound CO_2. It is interesting to observe the behavior of the intensity of the 80 meV and 90 meV peaks as a function of the temperature. Markedly, the annealing to -173 °C and -163 °C leads to a reduction of the 80 meV signal, while the 90 meV loss seems not to be affected, remaining as intense as the 141 meV loss. At -118 °C and -96 °C both losses show almost the same intensity. At these temperatures the peak assigned to physisorbed CO_2 is not present anymore. Above -118 °C the intensity of the loss at 140 decreases and goes to zero at -85 °C. Spectra in the -118 - 47 °C range show also additional peaks at 63, 150, 235 and 251 meV. After annealing to 47 °C all peaks attributed to the chemisorbed CO_2 disappear while the new vibrational frequencies are still present. On the basis of the TPD and XPS results it is well known that CO_2 dissociation into CO and oxygen occurs. CO remains adsorbed on the surface until 47 °C. The losses at 235 meV and 251 meV are in agreement with the observed CO behavior in previous studies [20,21]. Notably, the relative intensity of these signals changes with temperature. Above -96 °C the 251 meV peak decreases while the 235 meV peak increase. The two losses are due to two different coordination sites, namely bridge and terminal sites as known from literature [20,21]. The population of the two different adsorption sites for CO is a function of the total surface coverage which changes in this case with surface temperature due to different competing mechanisms, i.e. CO_2 decomposition, CO_2 desorption and CO desorption. At 227 °C a single dominant peak is observed at 63 meV; it is attributed to atomic oxygen produced by the CO_2 dissociation process.

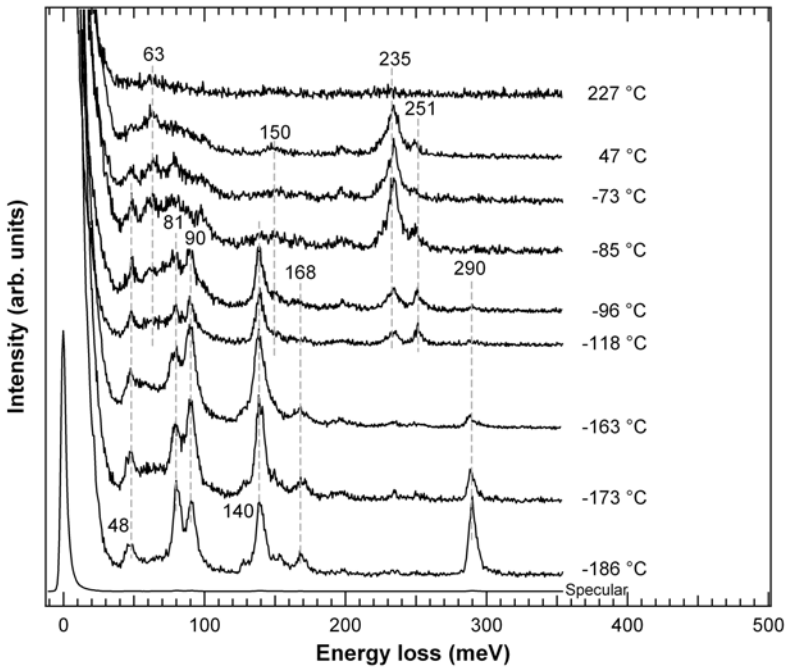

Figure 6.7: HREELS spectra on Ni(110) initially exposed to 0.22 L of CO_2 at -186 °C and subsequently heated to different temperatures.

The complete attribution of chemisorbed CO_2 related signal (Table 6.1) was possible only by combining the experimental results with DFT calculations, which were performed in collaboration with CNR-INFM DEMOCRITOS National Simulation Center of Trieste [22].

Table 6.1: vibrational frequencies assignment for chemisorbed CO_2 on Ni(110)

	VIBRATIONAL MODE (meV)			
	Asymm. stretch	**Symm. stretch**	**Bending**	**External stretch**
Ads. Site				
SB	-	141	81	46
HU	168		90	

Two non-equivalent adsorption sites (SB = short bridge site and HU = hollow up site) were identified. These configurations are simultaneously populated at temperatures lower than -73 °C. As depicted in Fig. 6.8, in the SB configuration, the molecular plane is perpendicular to the surface, while in the HU configuration, the molecular plane is

inclined with respect to the surface. In is important to note that in both sites, the molecule has mainly pure carbon coordination with the metal and is negatively charged and bent. The populated hollow up (HU) and short bridge (SB) adsorption configurations are almost energetically equivalent (ΔE = 0.07 eV) and are experimentally resolved by HREELS due to the differing vibration modes, whereas the related C1*s* and O1*s* chemical shifts are below the experimental conventional XPS resolution. The bending of the molecule is due to the charge transfer from the metal to the surface.

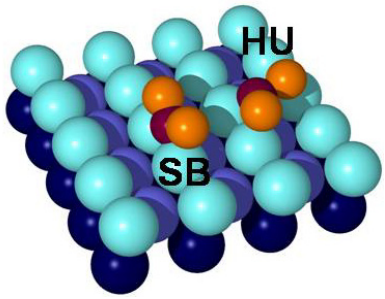

Figure 6.8: chemisorption configurations for CO_2, identified combining HREELS data with DFT calculations.

HREELS spectra of the CO_2 + H_2 and CO_2 + H_{at} layer are reported in Fig. 6.9 (left and right panel, respectively).

In the case of molecular hydrogen, at low temperature (T < -123 °C), the spectra present all the losses related to chemisorbed CO_2 and observed in the pure layer [22]. The asymmetric stretch feature of physisorbed CO_2 (290 meV) is reduced in intensity, in agreement with the XPS data which indicate a destabilization of this species in the presence of hydrogen. The intensity decrease of the loss at 141 meV due to chemisorbed CO_2 is attributed to a modification of the dynamic dipole moment upon co-adsorption of CO_2 and H. The peak at 131 meV is the fingerprint of the 0.50 monolayer of hydrogen atoms in bridge sites [23]. Its intensity is weak due to the low scattering dipole. The spectra give no evidence of losses in the C-H stretching region (330-380 meV), whose presence would indicate CO_2 hydrogenation. The additional weak contribution at 198 meV is due to contaminant water [24], detected also in the desorption spectra, and the one at 235 meV is due to adsorbed CO at the short bridge site [22]. In the -123 - 27 °C temperature range, four major peaks are present at 50, 98, 167, 365 meV. These four losses are characteristic of formate adsorbed on Ni(110) in a "reversed Y" configuration [25,26]. These features correspond to the following vibrational modes: Ni-O stretch, O-C-O wang, O-C-O symmetric stretch and C-H stretch, respectively. There is no evidence of losses which could be attributed to formic acid. At T > 25 °C, the spectra are dominated by the carbon monoxide peak at 235 meV.

Significant differences are observed after exposure of the CO_2 covered surface to the atomic hydrogen beam at -186 °C. At this temperature, besides the losses of the molecular experiment, a feature around 360 meV in the C-H stretch region is present, thus indicating the formation of an hydrogenated intermediate. It is important to stress the fact that no signal is observed in the molecular hydrogen experiment, where higher temperatures are necessary for the reaction. Moreover, in the low frequency region a loss around 55 meV is observed which disappears above -118 °C. On the basis of literature data [27,28] methoxy losses should be visible at 50 (Ni-OCH_3 symm. stretch), 128 (C-O), 143 (CH_3 rock), 179 (CH_3 deformation), 346 (C-H symm. stretch) and 361 meV (C-H asymm. stretch). Although some of these signals are observed in the spectra, however it cannot be ruled out the involvement of other species like H_2CO or HCO, which show some characteristic features at frequency near to those of methoxy. Increasing the temperature, the spectra becomes more similar to that recorded with molecular hydrogen.

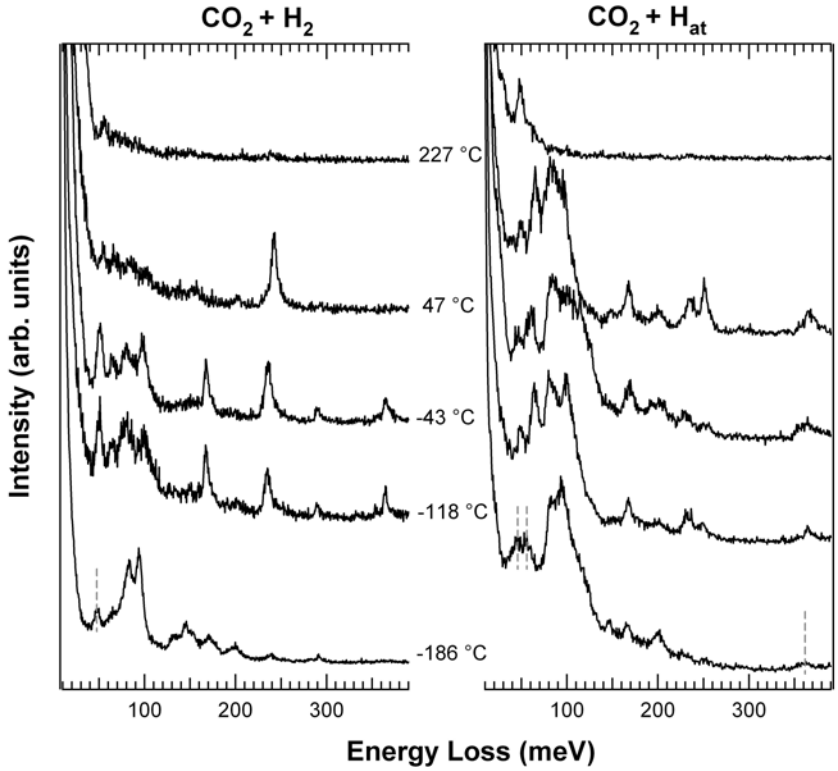

Figure 6.9: HREELS spectra on Ni(110) initially exposed to 0.22 L CO_2 + 10 L H_2 (left panel) and 0.22 L CO_2 + 10 L H_{at} (right panel) at -186 °C and subsequently heated to different temperatures.

6.2.3 Reaction modeling

The mechanism of CO_2 hydrogenation to methanol involves several successive hydrogenation steps, as shown in Fig. 6.10. Different intermediate species can be formed, which need to be identified. This is not straightforward.

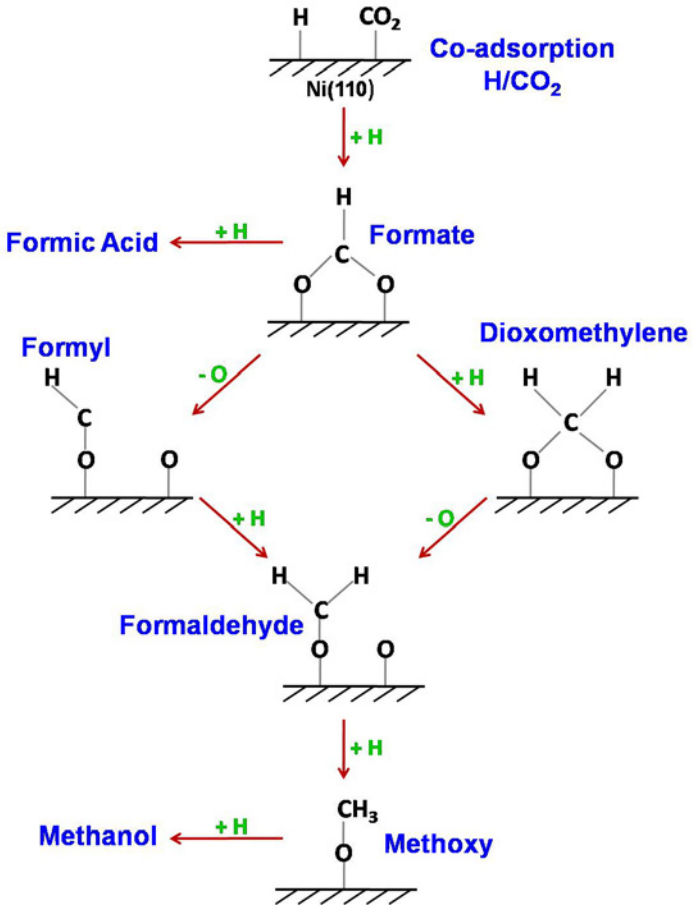

Figure 6.10: proposed reaction pathways for the hydrogenation of CO_2 to methanol.

It is reasonable to think that the first step of the reaction is the interaction of an adsorbed hydrogen atom with the activated carbon atom of the chemisorbed CO_2, leading to the formation of adsorbed formate. After that, the reaction proceeds with the interaction of the adsorbed formate with co-adsorbed hydrogen atom, yielding dioxomethylene. The subsequent interaction of the oxygen atom of the adsorbed dioxomethylene with an adsorbed atomic hydrogen can lead to the formation of adsorbed formaldehyde. Alternatively, formate can decompose into formyl species which can undergo hydrogenation to formaldehyde. This latter intermediate can, then, react with atomic hydrogen to produce adsorbed methoxy. The resulting methoxy can undergo further hydrogenation into methanol. Each hydrogenation step is characterized

by an energy barrier, the crossing of which is a function of parameters like the surface temperature or the energy content of the reactants.

Notably, evidences for the formation of formate species at -73 °C were previously reported in literature by Wambach *et al.*, upon adsorption of CO_2 on the hydrogen pre-covered surface [10]. The authors discuss the reaction pathways in terms of a Langmuir-Hinshelwood mechanism. This idea is supported by the observation that large H_2 pre-coverages suppress CO_2 adsorption, while small coverages of hydrogen induce formate formation. The temperature dependence of the production of the formate species points towards an activated process.

By changing the order of the reactants, as in the present work, the same intermediate was observed suggesting the idea that the reaction follows the same mechanism.

In order to clarify the atomic-scale details of the reaction (e.g. adsorption geometries of the intermediates mentioned above, adsorption energies, reaction energy barriers, etc.), we are now corroborating experimental data with theoretical calculations. It is noteworthy that, up to now, this detailed picture for the hydrogenation process of activated CO_2 was not fully explained.

Results indicate that when adsorbed H approaches CO_2, which at low temperature is negatively charged and is chemically bonded mainly via the carbon atom, the molecule flips, binds to the surface with the two oxygen atoms and H binds to the carbon atom, as displayed in Fig. 6.11. This leads to the formation of the formate intermediate, which is known to exist in such a configuration.

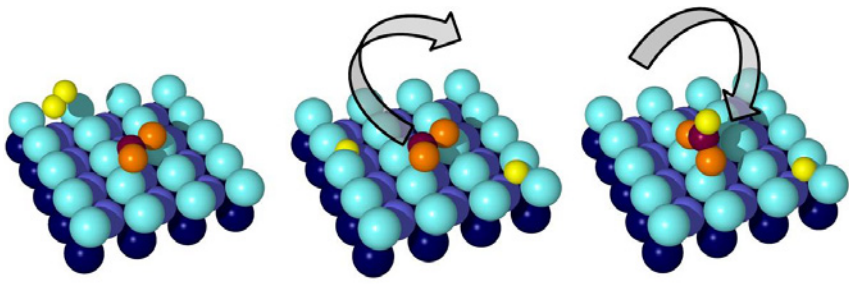

Figure 6.11: hydrogen assisted flip of activated carbon dioxide

The calculated barrier for the first hydrogenation of chemisorbed CO_2 is 0.43 eV, which is in agreement with our experimental finding. In fact, with molecular hydrogen the reaction takes place only above -123 °C. This energy barrier is smaller than that for CO_2 desorption and that for dissociation into CO+O. The subsequent hydrogen addition may occur at the carbon atom due to its residual valence. The energy barrier of this step is however higher than that of the first one and it cannot be overcome in simple UHV co-adsorption experiments. The situation seems to change with the use of

an atomic hydrogen beam. From the reaction point of view, the energy content of an H atom is higher than of a molecule, since the dissociation energy of H_2 has not to be subtracted from the reaction balance. This yields the possibility of benchmarking new reaction pathways which were not explored before.

6.3 CO_2 hydrogenation on Ni/Cu-based systems

6.3.1 Introduction

CO_2 hydrogenation has not been investigated as much as CO hydrogenation [29]. The most important reactions of CO_2 with hydrogen are:

- the Sabatier reaction
  $CO_2 + 4H_2 \leftrightarrow CH_4 + 2H_2O$ (6.2)
- the Bosch reaction
  $CO_2 + 2H_2 \leftrightarrow C + 2H_2O$ (6.3)
- the reverse water gas shift reaction
  $CO_2 + H_2 \leftrightarrow CO + H_2O$ (6.4)
- the synthesis of methanol
  $CO_2 + 3H_2 \leftrightarrow CH_3OH + 2H_2O$ (6.5).

The direction of CO_2 and H_2 mixture transformation depends on several factors like the catalyst composition (e.g. nature of the metal and support) as well as the operative conditions (H_2/CO_2 ratio, pressure, temperature, etc.).

Nickel is still the deeply studied as methanation catalyst for its high activity, excellent selectivity to methane, and relatively low price [30,31][Hu et al.; J.Mol.Struc.(Theochem.) 155(1999)491]. On the contrary, copper possesses poor activity towards methane formation, and a higher selectivity towards methanol production [29].

When the hydrogenation of CO_2 is compared with that of CO on nickel-based catalysts, two interesting features are noted: a) the rate of hydrogenation of CO_2 to methane appreciably exceeds the rate of methanation of CO; b) whereas higher hydrocarbons are formed together with methane in the hydrogenation of CO, methane is formed with an almost 100 % selectivity in the hydrogenation of CO_2 [32-41].

Two general reaction mechanisms have been proposed for CO_2 methanation. The first one involves the transformation of the CO_2 to CO and atomic oxygen (the latter of which is hydrogenated to H_2O) followed by further dissociation of CO to a carbon intermediate which is hydrogenated to methane [42]. The second mechanism involves

pathways not requiring the initial transformation of CO_2 to CO, but hydrogenation of CO_2 to methane occurs directly through the formation of CH_nO intermediates [43].

Concerning the reaction (6.5), it should be borne in mind that methanol is currently obtained from $CO/CO_2/H_2$ gas mixture using $Cu/ZnO/Al_2O_3$ catalyst at 250-300 °C and 10 MPa [44]. For a long time, it was believed that methanol was synthesized via intermediate hydrogenation of CO [45]. However, the use of the labeled $^{14}CO_2$ and ^{14}CO molecules [46,47] showed that the species which is hydrogenated is not CO but CO_2. Nevertheless, , unfortunately, the ternary catalyst ($Cu/ZnO/Al_2O_3$) does not display satisfying activity for hydrogenation of pure CO_2 [48]. For this reason, many efforts have been undertaken to design new catalysts for CO_2 hydrogenation to methanol. For instance, methanol was observed by Zhang *et al.* over Cu(12 wt.%)-V/Al_2O_3 at 240 °C with an H_2/CO_2 molar ratio equal to 3 [49]. The reaction was performed under a total pressure of 3.0 MPa.

6.3.2 Experimental results

- **Unsupported Ni/Cu**

Fig. 6.12 shows TPD-CO_2 experiments performed over pure NiO (Fig. 6.12 A), CuO (Fig. 6.12 B) and NiCu (Fig. 6.12 C) powders after reduction in H_2 at 600 °C for 1 h. It is evident that the dissociation of the molecule does not take place on any sample. Only above 700 °C, the CO signal slightly increases, mainly due to the thermal cracking of the molecule.

The CO_2 hydrogenation reaction was performed at 1 atm over pure NiO, CuO and NiCu powders after activation in H_2 at 600 °C for 1 h. The results are reported in Fig. 6.13 (A, B and C, respectively). On NiO, CO_2 and H_2 conversion starts above 170 °C. It is interesting to note that up to 350 °C, CO and water are the main detected products, while the formation of significant amounts of CH_4 is observed only above this temperature. It was reported by Fujita *et al.* [50] that on nickel catalyst, prepared by decomposition of nickel carbonate and reduction at 600 °C, the hydrogenation of adsorbed oxygen to water proceeds much more rapidly, compared with that of carbon species to methane. The authors performed the catalytic tests at a total pressure of 101 kPa. In spite of the different working conditions, a similar consideration can be inferred in the present work. Increasing the temperature, the H_2O signal increases faster than the one related to CO. A maximum is reached at about 410 °C for both water and carbon monoxide. At higher temperatures, the CO signal decreases, while the water production rate remains almost constant up to 550 °C. At 510 °C, a minimum is observed in CO production and H_2 consumption. On the contrary, at this temperature, a strong methane formation peak is found. It is evident that the decrease in CO signal is due to the methanation reaction, which consumes CO itself. For temperatures higher

than 510 °C, the CH_4 signal diminishes, while water and CO formation rates increase again. In the same temperature range, the H_2 conversion rapidly declines, while the consumption of CO_2 continues to grow, although more slowly. Methane disappears above 750 °C. Notably, the CH_4 selectivity can be varied by changing the H_2:CO_2 ratio. In particular, methane formation is inhibited when the H_2:CO_2 ratio decreases (data not reported).

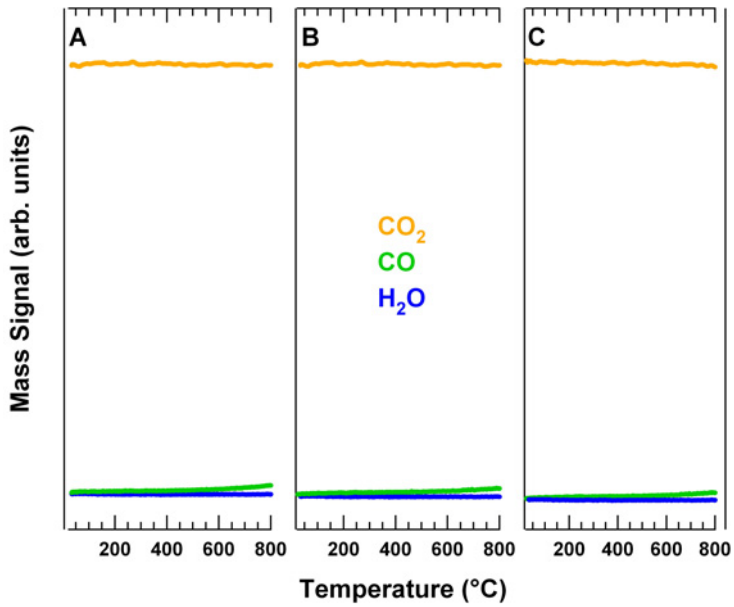

Figure 6.12: TPD-CO_2 over pure NiO (A), CuO (B) and NiCu (C) powder after reduction in H_2 at 600 °C for 1 h. Conditions: CO_2(10%) in Ar, GHSV = 6000 mL g^{-1} h^{-1}, 20 °C/min.

On pure CuO, the consumption of CO_2 and H_2 begins above 400 °C. Notably, no CH_4 was observed, in agreement with the poor methanation activity of copper. CO and water are monitored as the only products. The reaction product evolution is similar in the case of the NiCu sample. However, the reactivity of this latter system is shifted by 50 °C towards lower temperatures with respect to CuO.

From these findings, we suggest that on Ni, CO_2 activation is assisted by hydrogen, in analogy to UHV experiments. Indeed, no CO is observed if hydrogen is not introduced into the stream. The molecule could be activated with the addition of the first hydrogen to the carbon atom. The subsequent step (the cleavage of the first C-O bond) requires more energy and could be the rate limiting step. Below 430 °C, after the cleavage of the first C-O bond via an unstable intermediate, dehydrogenation to CO could occur, while in the 430-630 °C range the second C-O bond could also be dissociated, in analogy to UHV experiments where carbon monoxide is known to dissociate even on single crystal Ni surfaces.

In conclusion, Ni is highly efficient in CO_2 activation, by means of the formation of a hydrogenated intermediate which subsequently decomposes to CO. At high temperatures, the last C-O bond dissociates and the high selectivity of Ni with respect to the methanation reaction is confirmed. This suggests that in a Ni/Cu catalyst for methanol synthesis the role of the Ni sites could be mostly devoted to the activation of the molecule.

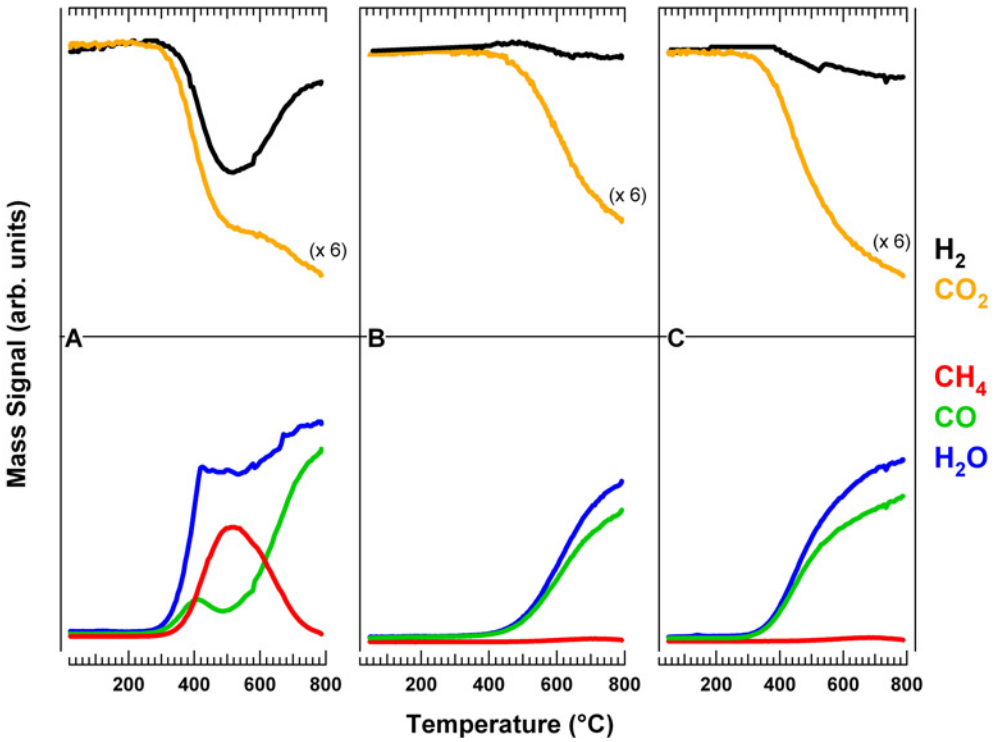

Figure 6.13: CO_2 hydrogenation over pure NiO (A), CuO (B) and NiCu (C) powder after reduction in H_2 at 600 °C for 1 h. Conditions: CO_2(10%) + H_2(60%) in Ar, GHSV = 6000 mL g^{-1} h^{-1}, 20 °C/min.

- **Ni/Cu supported on Al_2O_3**

Fig. 6.14 shows TPD-CO_2 spectra recorded over reduced Ni_{10}-Al (Fig. 6.14 A), Cu_{10}-Al (Fig. 6.14 B) and Ni_5Cu_5-Al (Fig. 6.14 C) catalysts. Below 600 °C, all catalysts do not have ability to activate the CO_2 molecule, as well as the unsupported ones.

The catalytic performance of Ni_{10}-Al, Cu_{10}-Al and Ni_5Cu_5-Al in CO_2 hydrogenation is very similar to that of unsupported samples, as depicted in Fig. 6.15 (A, B, C, respectively). The main difference is an appreciable shift towards lower temperature for the evolutions of all the products which can be associated with a higher metal dispersion for the supported catalysts. The data confirm the higher activity of Ni in the

methanation reaction (Fig. 6.15 A) with respect to copper (Fig. 6.15 B). In the case of the bimetallic system, a small CH_4 peak is found in the TPD spectra around 650 °C. Notably, it is reported in literature that the rate of methane production from CO at atmospheric pressure is greatly decreased by copper addition [51]. The invariance of kinetic parameters upon copper addition strongly suggests that this decrease is not due to electronic effects, but rather that it reflects a decrease of the number of sites. Indeed, active sites may be considered as ensembles composed by several adjacent active metal atoms. The formation of an alloy between copper and nickel, leads to a dilution of the active sites and consequently, the reaction rate can decrease [52]. Similar conclusions can be drawn also for CO_2 methanation in the present work.

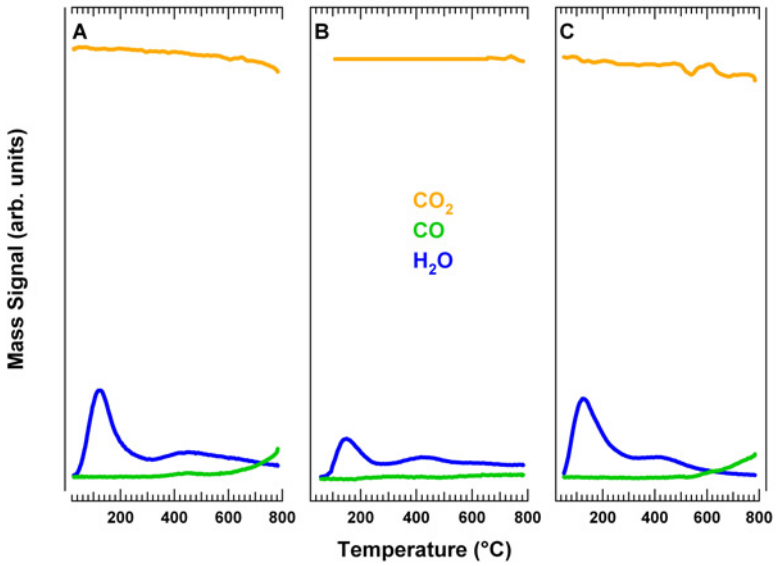

Figure 6.14: TPD-CO_2 over reduced Ni_{10}-Al (A), Cu_{10}-Al (B) and Ni_5Cu_5-Al (C) catalysts. Conditions: CO_2(10%) in Ar, GHSV = 6000 mL g^{-1} h^{-1}, 20 °C/min.

It is worthy of note that, with respect to unsupported metal samples, the support (Al_2O_3) is not inert. On bare Al_2O_3, CO_2 and H_2 start to be converted mainly to CO and H_2O above 400 °C, as depicted in Fig. 6.16 B. Notably, the alumina used as support is a high surface area γ-Al_2O_3, with a reasonable amount of hydroxyls groups which may contribute to CO_2 activation.

On the basis of these experimental results, it is possible to conclude that also on supported catalysts the activation of CO_2 is assisted by hydrogen. It is interesting to underline the fact that a similar behavior was observed on supported precious metal catalysts [53]. In this case, it was found that CO_2 dissociation is promoted by the presence of H and CH_x fragments on a catalyst surface.

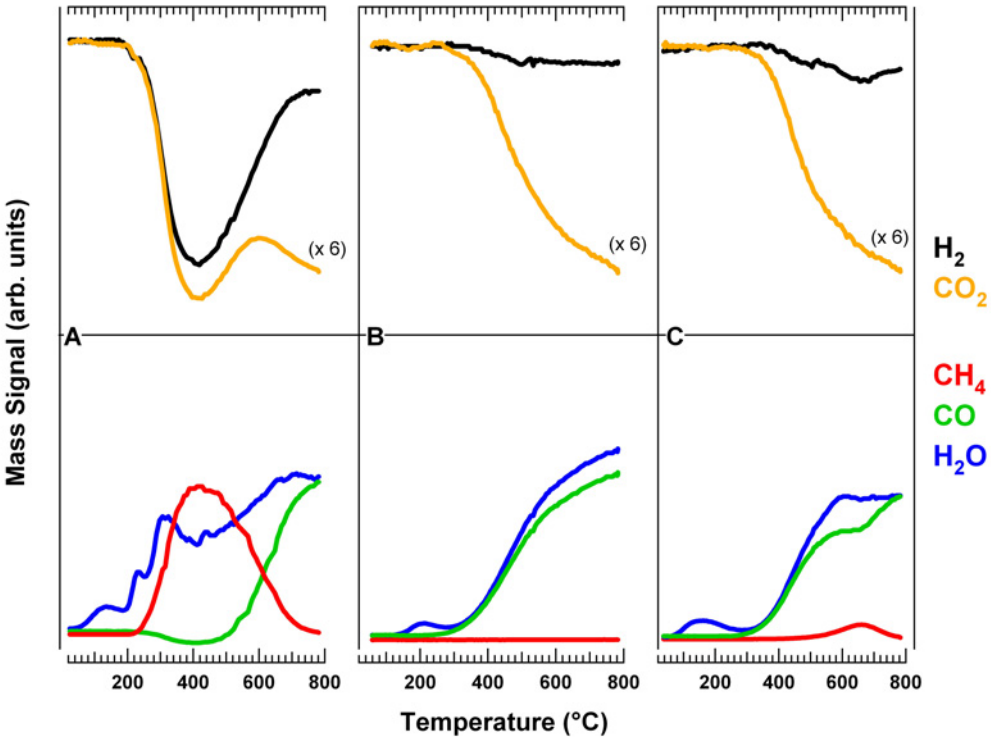

Figure 6.15: CO_2 hydrogenation over reduced Ni_{10}-Al (A), Cu_{10}-Al (B) and Ni_5Cu_5-Al (C) catalysts. Conditions: CO_2(10%) + H_2(60%) in Ar, GHSV = 6000 mL g^{-1} h^{-1}, 20 °C/min.

In order to compare the UHV results with those obtained at high pressure, it should be underlined that the type of interaction occurring between reactants and/or products and the catalyst, and hence catalyst activity, depends on the surface structure of the particles that constitute the active phase. On the other hand, such surface structure may be deeply affected by the interaction with the reactants and the products. In this way, the surface can suffer structural modification. The temperature, the gaseous atmosphere, and the interaction with the support, in other words, the chemical environment, may cause a significant modification in the structure of the active species. Furthermore, these modifications change with the pressure of the reactants (UHV vs. high pressure conditions). According to the effect of the particle structure upon the activity and selectivity of the reactions, some process are more or less structure sensitive. It was proposed that over carbon supported platinum catalysts CO_2 hydrogenation is affected by the changes in the size of the catalyst particles [54].

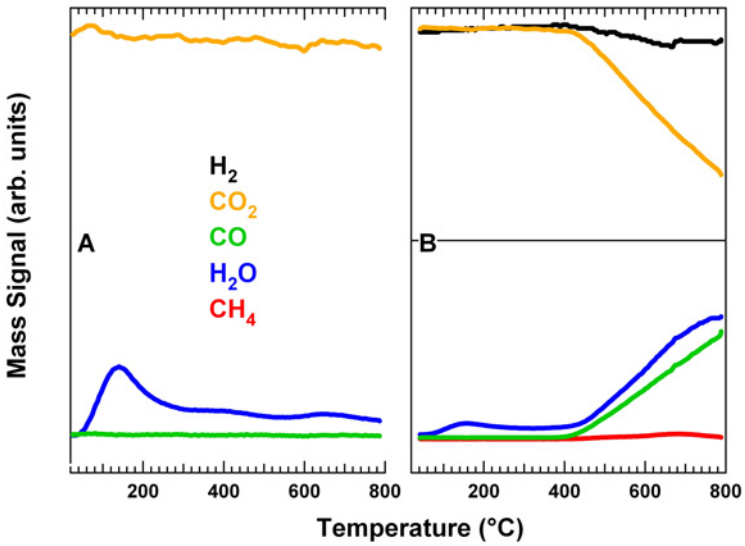

Figure 6.16: (A) TPD-CO_2 experiment and (B) CO_2 hydrogenation over bare Al_2O_3. Conditions: CO_2(10%) in Ar, GHSV = 6000 mL g^{-1} h^{-1}, 20 °C/min and CO_2(10%) + H_2(60%) in Ar, GHSV = 6000 mL g^{-1} h^{-1}, 20 °C/min.

References

[1] S.T. Ceyer, Accounts of Chemical Research 34 (2001) 737.

[2] S.T. Ceyer, Langmuir 6 (1990) 82.

[3] S.T. Ceyer, Science 249 (1990) 133.

[4] B.L.M. Hendriksen, S.C. Bobaru, Frenken, J.W.M., Topics in Catalysis 36 (2005) 43.

[5] J. Nerlov, Ib. Chorkendoff, Catalysis Letters 54 (1998) 171.

[6] J. Nerlov, S. Sckerl, J. Wambach, I. Chorkendoff, Applied Catalysis A-General 191 (2000) 97.

[7] J. Nerlov, I. Chorkendoff, Journal of Catalysis 181 (1999) 271.

[8] A. Christensen, A.V. Ruban, P. Stoltze, K.W. Jacobsen, H.L. Skriver, J.K. Norskov, F. Besenbacher, Physical Review B 56 (1997) 5822.

[9] S. Quannasser, L.T. Wille, H. Dreysse, Physical Review B 55 (1997) 14245.

[10] J. Wambach, G. Illing, H.J. Freund, Chemical Physics Letters 184 (1991) 239.

[11] P.A. Taylor, P.B. Rasmussen, C.V. Ovesen, P. Stoltze, I. Chorkendoff, Surface Science 261 (1992) 191.

[12] P.B. Rasmussen, M. Kazuta, I. Chorkendoff, Surface Science 318 (1994) 1994.

[13] P.B. Rasmussen, P.M. Holmblad, T. Askgaard, C.V. Ovesen, P. Stoltze, J.K. Norskov, I. Chorkendoff, Catalysis Letters 26 (1991) 373.

[14] A.R. Alemozafar, R.J. Madix, Journal of Physcal Chemistry B 108 (2004) 14374.

[15] A. Emundts, G. Pirug, J. Werner, H.P. Bonzel, Surface Science 410 (1998) L727-L735.

[16] R. Neubauer, C.M. Whelan, R. Denecke, H.P. Steinruck, Surface Science 507-510 (2002) 832.

[17] G. Illing, D. Heskett, E W. Plummer, H.-J. Freund, J. Somers, Th. Lindner, A.M. Bradshaw, U. Buskotte, M. Neumann, U. Starke, K. Heinz, P.L. de Andres, D.K. Saldin, J. B. Pendry, Surface Science 206 (1988) 1.

[18] H. Lindner, D. Rupprecht, L. Hammer, K. Muller, Journal of Electron Spectroscopy and Related Phenomena 44 (1987) 141.

[19] B. Bartos, H.J. Freund, H. Kuhlenbeck, M. Neumann, H. Lindner, K. Mueller, Surface Science 179 (1987) 59.

[20] J. Bauhofer, M. Hock, J. Kippers, Surface Science 191 (1987) 395.

[21] B.J. Bandy, M.A. Chesters, P. Hollins, J. Pritchard, N. Sheppard, Journal of Molecular Structure 80 (1982) 203.

[22] X. Ding, L. De Rogatis, E. Vesselli, A. Baraldi, G. Comelli, R. Rosei, L. Savio, L. Vattuone, M. Rocca, P. Fornasiero, F. Ancilotto, A. Baldereschi, M. Peressi, Physical Review B 76 (2007) Art.No.195425.

[23] N.D.S. Canning, M.A. Chesters, Surface Science 175 (1986) L811-L816.

[24] M. Hock, U. Seip, I. Bassignana, K. Wagenmann, J. Kuppers, Surface Science 177 (1986) L978.

[25] T.S. Jones, M.R. Ashton, N.V. Richardson, Journal of Chemical Physics 90 (1989) 7564.

[26] S. Haq, J.G. Love, H.E. Sanders, D.A. King, Surface Science 325 (1995) 230.

[27] S.R. Bare, J.A. Stroscio, W. Ho, Surface Science 155 (1985) L281-L291.

[28] S.R. Bare, J.A. Stroscio, W. Ho, Surface Science 150 (1985) 399.

[29] O.V. Krylov, A.Kh. Mamedov, Russian Chemical Reviews 64 (1995) 877.

[30] F.W. Chang, M.S. Kuo, M.T. Tsay, M.C. Hsieh, Applied Catalysis A-General 247 (2003) 309.

[31] C. Hu, P. Hu, M. Li, A. Tian, Journal of Molecular Structure 491 (1999) 155.

[32] K.J. Williams, A.B. Boffa, J. Lahtinen, M. Salmeron, A.T. Bell, G.A. Somorjai, Catalysis Letters 5 (1990) 385.

[33] A. Boffa, C. Lin, A.T. Bell, G.A. Somorjai, Journal of Catalysis 149 (1994) 149.

[34] A. Guerrero-Ruiz, I. Rodriguez-Ramos, Reaction Kinetics and Catalysis Letters 29 (1985) 93.

[35] J. Lahtinen, T. Anraku, G.A. Somorjai, Catalysis Letters 25 (1994) 241.

[36] M.C. Roman-Martinez, D. Cazorla-Amoros, A. Linares-Solano, C. Salinas-Martinez de Lecea, Applied Catalysis A-General 116 (1994) 187.

[37] J.A. Dalmon, Journal of Chemical Society, Faraday Transaction I 75 (1979) 1011.

[38] D.J. Dwyer, G.A. Somorjai, Journal of Catalysis 52 (1978) 291.

[39] M. Araki, V. Ponec, Journal of Catalysis 44 (1976) 439.

[40] N.M. Gupta, V.S. Kamble, V.B. Kartha, R.M. Iyer, K. Ravindranathan Thampi, M. Gratzel, Journal of Catalysis 146 (1994) 173.

[41] F. Solymosi, Journal of Chemical Society, Faraday Transaction I 77 (1981) 1003.

[42] D.E. Peebles, D.W. Goodman, J.M. White, Journal of Physical Chemistry 87 (1983) 4378.

[43] G.D. Lee, M.J. Moon, J.H. Park, S.S. Park, S.S. Hong, Korean Journal of Chemical Engineering 22 (2005) 541.

[44] G.C. Chinchen, P.J. Denny, J.R. Jennings, M.S. Spencer, K.C. Waugh, Applied Catalysis 36 (1998) 1.

[45] K. Klier, Advances in Catalysis 31 (1982) 243.

[46] M. Bowker, H. Houghton, K.C. Waugh, Journal of Chemical Society, Faraday Transaction I 77 (1981) 3023.

[47] G.C. Chinchen, P.J. Denny, D.G. Parker, M.S. Spencer, D.A. Whan, Applied Catalysis 30 (1987) 333.

[48] T. Inui, T. Takeguchi, Catalysis Today 10 (1991) 95.

[49] Y. Zhang, J. Fei, Y. Yu, X. Zheng, Journal Natural Gas Chemistry 16 (2007) 12.

[50] S. Fujita, H. Terunuma, H. Kobayashi, N. Takezawa, Reaction Kinetics and Catalysis Letters 33 (1987) 179.

[51] G.A. Martin, Catalysis Reviews-Science and Engineering 30 (1988) 519.

[52] E.B. Pereira, G.A. Martin, Applied Catalysis A-General 103 (1993) 291.

[53] F. Solymosi, Gy. Kutsan, A. Erdohelyi, Catalysis Letters 11 (1991) 149.

[54] M.C. Roman-Martinez, D. Cazorla-Amoros, C. Salines-Martinez de Lecea, A. Linares-Solano, Langmuir 12 (1996) 379.

Chapter 7

Conclusions and perspectives

In a sustainable energy development, hydrogen will become very important as it is considered one of the key energy carriers in terms of energy content, as fuel for transportation and intermediate in the conversion of renewable energy sources. In this respect, catalytic technologies will play a significant role. The aim of this work was the design of novel catalysts for hydrogen production from both methane and methanol-ethanol/water solution. Special interest was also focused on the CO_2 hydrogenation reaction, as a potential chemical route to its valorization and to mitigate the greenhouse effect.

Active catalysts, resistant to the sinterization under severe reaction conditions, were developed through a simple and low cost synthetic route combining the high reactivity of nanosized noble metal particles with the excellent high temperature stability of Al_2O_3-based nanocomposites. The catalyst design was based on the encapsulation of pre-formed Rh nanoparticles into porous oxides, which limits the mobility of the metal particles at high temperature. As a major effect, the encapsulation of the Rh nanoparticles inhibits their sinterization and prevents their total occlusion, favoring the accessibility of the catalytic sites to the reactant. As suggested by catalytic activity tests and TEM characterization, the samples maintained their nanostructured design. The deposition and the growth of the protective oxide layers around the Rh nanoparticles were realized in a single or two step processes. In the first case, the strategy lead to a material with some particles surrounded by porous oxide, while some of them were situated at the surface of the support and therefore only partially embedded/protected. On the other hand, modifying the Al precipitation step, a better incorporation and preservation of particle sizes, due to the milder conditions of pH and ionic strength during the synthetic procedure, were achieved.

The catalysts were tested for the Catalytic Partial Oxidation of Methane (MPO). The embedded Rh(1 wt.%)@Al_2O_3-1-shell and Rh(1 wt.%)@Al_2O_3-2-shell presented higher thermal stability with respect to a reference catalyst obtained by conventional incipient wetness impregnation, under MPO conditions at 750 °C. This higher stability was correlated to the protection offered by the surrounding layer of porous oxide which prevented extensive sintering of the active metal phase. Additional partial deactivation of the catalysts was observed due to some coke deposition. This deactivation was essentially reversible in the case of the embedded systems. On the contrary, the deactivation observed on the impregnated Rh(1 wt%)/Al_2O_3 catalyst was mainly irreversible. In fact, in this case, the major factor inducing the deactivation was the sinterization of the metal phase and/or the incorporation of Rh into the Al_2O_3 lattice during high temperature treatments.

Despite their similar reactivity during the run-up experiments, the embedded Rh catalysts presented significant differences in their stability at 750 °C under MPO conditions. Indeed, on the Rh(1%)@Al_2O_3-2-shell sample, the CH_4 conversion remained complete more then twice longer with respect to Rh(1%)@Al_2O_3-1-shell catalyst. This behavior could be ascribed to a lower rate of coke deposition on 2-shell system with respect to 1-shell.

All these results confirm the fact that the careful control of the particle size and interaction with stabilized supports can significantly prevent catalyst deactivation through sintering making these catalysts a viable choice when catalyst lifetime is taken into account. The high cost of Rh can be partially compensated by its high activity, and the consequent low loading requirements, and high stability. Its use could become a reality in small reformers.

In order to obtain a better understanding of the interaction between Rh nanoparticles and the alumina support in the embedded catalysts (e.g. the effect of thickness of the protective layer on metal-support interaction and the nature of the Rh species), an XPS study on three model embedded Rh systems was performed. Among them, the behavior of the model Rh(33 wt.%)@Al_2O_3 sample is very interesting. Indeed, in this case a new component in the XPS spectra was found, after reduction in H_2 at 750 °C for 2 h. Further investigations are still in progress. However, on the basis of the XPS spectra together with the TPR and XRD measurements, we suggest that the origin of this particular feature is associated to the encapsulation process of the metal nanoparticles rather than to the particle size effect.

The extension of the embedding approach to Ni/Cu-based systems was also handled. Although stable suspension of Ni and Cu nanoparticles were successfully prepared, the incorporation of the pre-formed metal particles could not be realized through the precipitation method, as in the Rh case. This is mainly due to the reoxidation tendency of these non precious metals and the poisoning of the final materials with residual compounds, such as $NaBH_4$, used during the synthesis. It is clear

that a different approach has to be developed. Stable oxides nanoparticles could be used instead of metal nanoparticles in order to adopt a similar preparation procedure. In fact, in a subsequent step the embedded nanoparticles of the oxides could be reduced to form the active phase.

In addition, Ni(x%)Cu(y%)/Al_2O_3 catalysts with different Ni and Cu contents were synthesized using the conventional impregnation method. All the samples were tested towards the partial oxidation of methane and the steam reforming of methanol and ethanol.

The impregnation of alumina with Ni or/and Cu nitrates, followed by calcinations, yielded the formation of metal oxides. XRD and XAFS data indicated a high metal oxide dispersion in the case of Ni and Ni/Cu systems, while relatively low dispersion was observed for the bare Cu(10%)/Al_2O_3 system.

The interaction with the support and the concomitant presence of the two metals strongly promotes the reducibility of the material. Easy passivation/reoxidation of the reduced supported metals was observed.

The catalytic MPO activity data of Ni(10 wt.%)/Al_2O_3 and Ni(5 wt.%)Cu(5 wt.%)/Al_2O_3 were consistent with a reaction scheme which involves the oxidation of metallic species at low temperature (< 300 °C) followed by a second step in which the metal oxide particles are reduced at a "critical temperature". Total combustion of CH_4 occurs on the oxidized particles, while partial oxidation, with H_2 and CO production, in a ratio 2 to 1, is operative on reduced particles. Furthermore, a significant lowering of the light-off temperature (temperature corresponding to 50% conversion) was observed for the bimetallic system. This improvement is associated with the formation of an alloy between Ni and Cu. The formation of the alloy strongly reduces also the coke deposition under MPO conditions, increasing the life-time of the catalyst. Notably the Ni:Cu ratio did not affect the catalytic performance during the run-up experiments, although the composition of the alloys produced during the H_2 treatment at 750 °C for 2 h before the catalytic test, is different. However, influences on the rate of coke deposition cannot be excluded. These aspects are under investigation.

Neither copper nor nickel alone supported on alumina appeared as suitable catalysts for ethanol steam-reforming at low temperatures (T < 500 °C). Over the Cu(10 wt.%)/Al_2O_3 sample, dehydrogenation of ethanol into acetaldehyde occurs but the reforming reaction does not proceed further to yield H_2 and CO_x. On the other hand, on the Ni(10 wt.%)/Al_2O_3 catalysts, the decomposition reaction of ethanol to CH_4 and CO_x is favored. Only at high temperature (T > 550 °C) methane production is inhibited by steam-reforming processes. The activity of the bimetallic systems, during the first run-up experiment, is not very different from the monometallic Ni system. The Ni:Cu ratio did not seem to affect the product distribution. Despite their similar activity, these samples present different stability during the two subsequent run-up experiments. The Ni_3Cu_7-Al catalyst shows the lowest stability.

The catalytic performance of bimetallic systems was more promising in the methanol steam reforming. Indeed, the introduction of copper in the catalyst formulation showed a positive effect, since it inhibits the formation of methane, an undesirable by-product. No significant deactivation for all samples was observed.

On Ni/Cu based samples, CO_2 hydrogenation was also investigated. All catalysts did not show the ability to activate the CO_2 molecule, as well as the corresponding unsupported systems. No CO was observed if hydrogen was not introduced into the stream. These findings suggest that the CO_2 molecule could be activated with the addition of the first hydrogen to the carbon atom. The subsequent step (the cleavage of the first C-O bond) requires more energy and could be the rate limiting step. These results are in good agreement with the data obtained on Ni single crystal (Ni(110)), under UHV conditions. In this case, stable hydrogenation intermediates/products were observed during the reaction by means of X-Ray Photoelectron Spectroscopy (XPS), Temperature Programmed Desorption (TPD) experiments and High Resolution Electron Energy Loss Spectroscopy (HREELS) in the temperature range of -180/230 °C. The evolution of the surface species and concentrations as a function of the annealing temperature were examined. This work was supported by parallel DFT calculations, in order to model both experimentally and theoretically the CO_2 hydrogenation reaction. The final aim is to build a complete picture of the mechanisms for the activation of the molecule, to identify the rate limiting steps and the hydrogenation barriers, and to evaluate adsorption sites, binding energies and reaction or diffusion barriers for the involved species.

At low *T* on Ni(110), CO_2 is negatively charged and chemically bonded mainly via the carbon atom. Exposure of the CO_2 covered Ni(110) surface at -180 °C to molecular hydrogen, followed by annealing in the -123/-23 °C range, yielded evidence for the formation of formate which is stable up to RT and subsequently decompose to carbon dioxide and hydrogen. No water is detected in the TPD spectra, thus indicating no decomposition of C-O bonds. The mechanism which activates the adsorbed molecule for subsequent hydrogenation and decomposition reactions is the formation of the first C-H bond. The carbon bonded, bent CO_2 molecule turns upside down and the formate binds to the metal via two Ni-O bonds. After the activation of the molecule, addition of another hydrogen atom and the subsequent cleavage of the first C-O bond have to follow. This is the rate limiting step which can be overcome under high pressure conditions. In our UHV simulation of the reaction, we have employed an atomic hydrogen beam, thus supplying from the outside the energy for the cleavage of the H_2 molecule bond. In this way, a simulation of high pressure regimes is obtained under UHV conditions, where otherwise a gap of ten orders of magnitude in the hydrogen pressure amounts to as much as 0.6 eV of lower free energy per molecule at RT. Exposure to the atomic hydrogen beam of the CO_2 covered metal surface at -180 °C yields already the formation, in addition to formic acid, of C-H bonds and water, which

is detected in the TPD spectra, thus indicating the cleavage of the carbon oxygen bond. However, the new surface species cannot be clearly identified (e.g. CH_3O, H_2CO or HCO). In this respect, theoretical calculations, which are still in progress, will be very useful.

Summarizing, better knowledge on the reactivity of Rh, Ni and Cu based catalysts under various reaction conditions has been obtained. The data has been used and will be used to develop an improved class of catalysts: the protected embedded metal nanoparticles.